DESIGN AND CHARACTERIZATION OF OPTICAL PHASED ARRAY WITH HALF-WAVELENGTH SPACING

by

Ziyun Kong

A Dissertation

Submitted to the Faculty of Purdue University

In Partial Fulfillment of the Requirements for the degree of

Doctor of Philosophy

School of Electrical and Computer Engineering

West Lafayette, Indiana

December 2021

THE PURDUE UNIVERSITY GRADUATE SCHOOL
STATEMENT OF COMMITTEE APPROVAL

Dr. Minghao Qi, Chair

School of Electrical and Computer Engineering

Dr. Andrew M. Weiner

School of Electrical and Computer Engineering

Dr. Peter A. Bermel

School of Electrical and Computer Engineering

Dr. Weng Cho Chew

School of Electrical and Computer Engineering

Approved by:

Dr. Dimitrios Peroulis

To my grandparents.

ACKNOWLEDGMENTS

I have received a lot of support and assistance during my Ph.D. journey. I would like to express my deep appreciation to my advisor, Prof. Minghao Qi for giving me the exceptional opportunity, genuine advice and extensive resources. The completion of my dissertation would not have been possible without his encouragement, patience and guidance throughout the years. I would also like to express my deep gratitude to my master's degree advisor and my committee member, Prof. Andrew M. Weiner. His broad knowledge, keen perspective, and endless passion for science have deeply infected me. My sincere gratitude extends to all my committee members, Prof. Peter A. Bermel and Prof. Weng Cho Chew, for their kind encouragement and constructive feedback on my thesis work.

I would like to thank the lab manager of Purdue ultrafast optics lab, Dr. Daniel E. Leairds for his superb and versatile engineering skills, and his support, help and guidance for my experiments.

I have enjoyed working with all my current and former colleagues in the group. Special thanks to Dr. Min Teng, Dr. Yun Jo Lee, Dr. Abudulla Al Noman, Mr. Gregory Chang, Mr. Yingheng Tang and Mr. Ruihan Chen, for all the insightful discussion, valuable advice, and assistance. I also want to thank former and present group members of the Ultrafast Optics and Optical Fiber Communications Lab: Dr. Xiaoxiao Xue, Dr. Chengying Bao, Dr. Yang Liu, Dr. Andrew J. Metcalf, Dr. Pei-Hsun Wang, Dr. Amir Rashidinejad, Dr. Jose Jaramillo, Dr. Ogaga D. Odele, Dr. Poolad Imany, Dr. Oscar E. Sandoval, Mr. Beichen Wang, Dr. Cong Wang, Dr. Mohammed Saleh Al alshaykh, Dr. Keith McKinzie, Dr. Hsuan-Hao Lu, Dr. Navin Lingaraju, Ms. Alex Moore, Mr. Nathan OMalley, and Ms. Suparna Seshadri.

Last but not least, I wholeheartedly thank my parents, Mr. Liang Kong and Mrs. Xiaoqiu Song, who have always loved and supported me unconditionally. I also want to express my great appreciation to my wife, Ms. Yizhen Zhang, who has accompanied and encouraged me throughout my graduate life. Thanks also to my friends who have always cheered me on and celebrated every accomplishment with me.

PREFACE

The content of this thesis includes the extension of the author's previously published works, which are listed below:

- **Kong, Z., Lee, Y. J., Al Noman, A., Tang, Y., Chang, G., & Qi, M.** (2020, May). *Design of 2D Optical Phased Array Emitters with Half-wavelength Spacing and Less Than-20 dB Crosstalk.* In CLEO: Applications and Technology (pp. AF3M-6). Optical Society of America.

- **Kong, Z., Lee, Y. J., Al Noman, A., Tang, Y., Chang, G., Chen, R., & Qi, M.** (2020, July).*Aliasing-free Beam Steering from an Optical Array Emitter with Half-wavelength Pitch.* In Integrated Photonics Research, Silicon and Nanophotonics (pp. ITh2H-6). Optical Society of America.

TABLE OF CONTENTS

LIST OF TABLES

LIST OF FIGURES

ABBREVIATIONS

OPA	Optical phased array
LiDAR	Light detection and ranging
ADAS	Advanced driver assistant system
FoV	Field of view
FWHM	Full width half maximum
E-skid	**E**xtreme **ski**n-**d**epth
MMI	multi-mode interference / Multi-mode interferometer
SOI	Silicon on insulator
SiN / SiN_x	Silicon nitride
FDTD	Finite Difference Time Domain
IL	Insertion loss
LN	$LiNbO_3$, Lithium niobate
SEM	scanning electron microscope
CW	Continuous wave
EDFA	Erbium-doped fiber amplifier
PIC	Photonic integrated circuits
PDL	Path-dependent loss
OMINs	Optical multistage interconnection networks
SNR	Signal-to-noise ratio

ABSTRACT

Integrated optical phased arrays (OPAs) have gained popularity for achieving beam steering with no moving parts and potential high speed and small beam divergence angle. These characteristics are crucial for applications like free-space communication and light detection and ranging (LiDAR), a key component in autonomous driving. Two main aspects that affect the performance of an integrated OPA are discussed: high power handling and large beam steering range.

High emission power from the OPA is desirable for long range detection applications. Silicon is broadly used in integrated OPA designs as it allows for structures with a more compact footprint. However, its power-handling capability is limited by the two-photon absorption of the material, resulting in higher loss and potential damage at high input power levels. In this work, high power delivery into free space is realized by using a silicon nitride (SiN) and silicon hybrid platform. SiN components are used to direct and split high input power into smaller portions and coupled into silicon components for a more compact emitter array.

In order to achieve a full 180°beam steering range with aliasing-free operation, the pitch of a periodic emitter array is required to be half of the operating wavelength or less. At such a small pitch, evanescent coupling between adjacent emitters causes strong crosstalk. We demonstrate the optical phased array based on uniform half-wavelength spaced grating emitter array. Two-dimensional beam confinement and a record-high aliasing-free beam steering field-of-view of 135° from grating emitter are measured from a 32 channel SiN/Si hybrid OPA. Evanescent coupling between waveguides are suppressed by metamaterial-based **e**xtreme **ski**n-**d**epth (e-skid) waveguides. The e-skid waveguides utilize an alternating air-silicon multi-fin side cladding. The high index contrast of those sub-wavelength ridges provides strong anisotropy, which leads to faster decay of the evanescent wave for transverse electric (TE) input modes, thus limiting evanescent coupling between closely spaced waveguides.

Furthermore, we extend the concept of the half-wavelength-pitched emitter array to the design of a two-dimensional end-fire OPA. This OPA can potentially achieve 180° × 180°

full-range beam steering with no grating lobes by having a half-wavelength emitter pitch in both dimensions. The design of a broadband 8×8 silicon photonics switch based on the half-wavelength-pitched emitter array with low path-dependent loss (PDL) is also discussed.

1. INTRODUCTION

Light detection and ranging (LiDAR) is a crucial component for advanced driver assistant systems (ADAS) and autonomous vehicles for its capability to provide ranging and motion detection with high speed and precision. Furthermore optical phased array (OPA) offers a solution to the rising need for a compact, reliable LiDAR system. OPA enables chip-scale beam steering with no moving parts, making it much more reliable than current mechanical solutions. Thanks to the recent advance in silicon photonics, mass production of large-scale integrated OPA has been made possible for several foundries. The rapidly maturing OPA technology has led to numerous demonstrations with increasing performance since the last decade[1]. Current focus for OPA development includes minimizing pitch array for large field-of-view beam forming[2], large aperture size of the emitter for smaller beam diffraction angle [3], long detection range[4], compact packaging[5] and full integration[6] of OPA system, etc. One crucial aspect of the OPAs for automotive applications is the ability to steer the output beam into a wide field of view (FOV) without extra grating lobes. While the grating lobes cause ambiguity and power loss in field applications, a solution of an aliasing-free OPA is in great demand.

Optical phased arrays, adapted from radio frequency (RF) phased array, is an array of emitters fed by a coherent source. The emitters have a phase control mechanism to adjust the emitted wavefront, thus resulting in a desired far field pattern. To illustrate the emission from an emitter array, we assume an array of identical emitters placed with equal spacing in between them, each with emission[7]:

$$E_{\mathrm{i}}(r) = A_{\mathrm{i}}\mathrm{e}^{\mathrm{j}\phi_{\mathrm{i}}}\mathrm{e}^{\mathbf{jkr}} \tag{1.1}$$

where A_{i} and ϕ_{i} are the amplitude and phase of the i_{th} emitter. $k = 2\pi/\lambda$ is the wave vector and r is the spatial vector of the emitter. Here we suppressed the time-dependency $\mathrm{e}^{\mathrm{j}\omega t}$ for simplicity. As a result, the total emission being observed at a given angular direction θ can be expressed as the sum of all emitters:

$$E(\theta) = \sum_{\mathrm{i}=1}^{N} E_{\mathrm{i}} = \sum_{\mathrm{i}=1}^{N} A_{\mathrm{i}} \mathrm{e}^{\mathrm{j}(\mathbf{k}\mathbf{r}_{\mathrm{i}}+\phi_{\mathrm{i}})} \tag{1.2}$$

If we assume a uniform emitter array with uniform emission strength across emitters, spacing d and a linear phase difference $\Delta\phi$ in between emitters, the above equation can be simplified to

$$E(\theta) = A(\theta) \sum_{\mathrm{i}=1}^{N} \mathrm{e}^{\mathrm{j}n(kd\cos(\theta)+\Delta\phi)} \tag{1.3}$$

where $A(\theta)$ is the emission profile of the emitter element, which is known as the element factor. And the array factor

$$\sum_{\mathrm{i}=1}^{N} \mathrm{e}^{\mathrm{j}n(kd\cos(\theta)+\Delta\phi)} \tag{1.4}$$

resembles a finite geometric series, so

$$|E(\theta)| = |A(\theta)| \left| \frac{\sin(\frac{N}{2}(kd\cos(\theta) + \Delta\phi))}{\sin(\frac{1}{2}(kd\cos(\theta) + \Delta\phi)} \right| \tag{1.5}$$

expresses the radiation pattern of a uniform antenna array. As illustrated in Fig. 1.1 [8], beam forming and steering could be achieved by altering the linear phase difference $\Delta\phi$ between emitters, resulting in the beam steering along azimuthal direction.

More specifically, when a linear phase difference of $\Delta\phi$ is applied to the phased array, the emitted beam is tilted by θ, where:

$$\sin\theta = \frac{\lambda\Delta\phi}{2\pi d} \tag{1.6}$$

Here d is the spacing between adjacent emitters and λ is the operating wavelength, $\Delta\phi \in [-\pi, \pi]$. All emitted beams, including higher order lobes as shown in Fig 1.1(b) and (c)

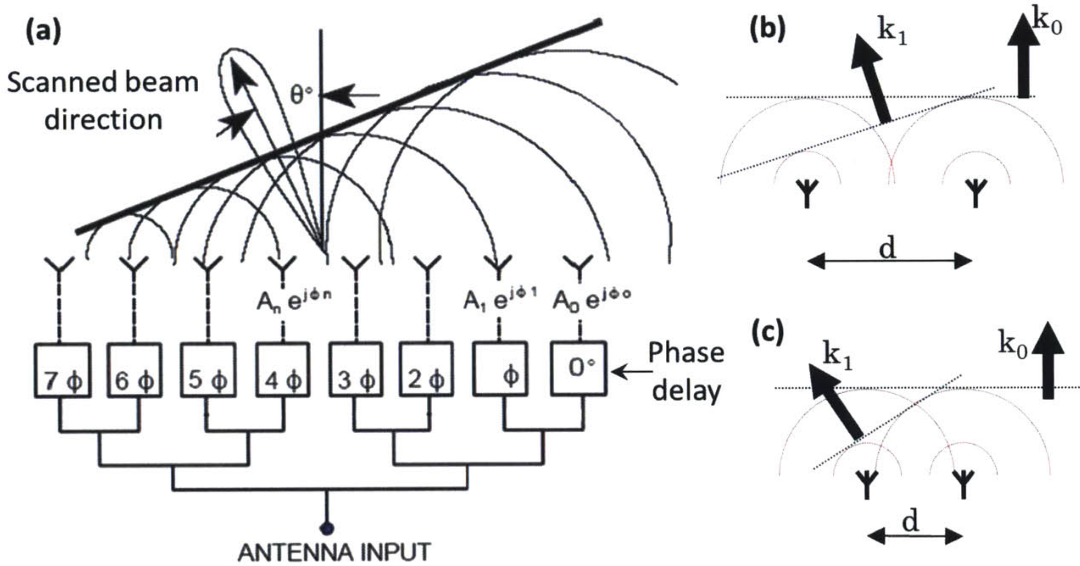

Figure 1.1. Illustration of the phased array basics. (a) Flat wavefront forming and beam steering from an array of emitters with a linearly increasing phase delay. (b)/(c): Higher order emission of an OPA from constructive interference, where larger emitter spacing (b) gives closer high order emission lobes; And smaller spacing (c) gives larger angle separation between emitted beams. The figure is adapted from [8].

(sometimes referred as grating lobes due to their similarity to higher grating order) are emitted to θ_n, where:

$$\sin\theta_n = \frac{\lambda(\Delta\phi + 2n\pi)}{2\pi d}, n \in \mathbb{Z} \tag{1.7}$$

The beam corresponding to $n = 0$ is called the main lobe. And $n \neq 0$ are called higher order lobes or grating lobes. Note that the separation between the main lobe and first order grating lobe increases with decreasing d. Fig. 1.2 illustrates a measured emission pattern captured by an IR viewing card from a 5 μm spacing SiN OPA.

An unambiguous beam steering range is defined as the range in which only the main lobe is visible and no grating lobes, as illustrated in Fig. 1.3. Due to the symmetry of the

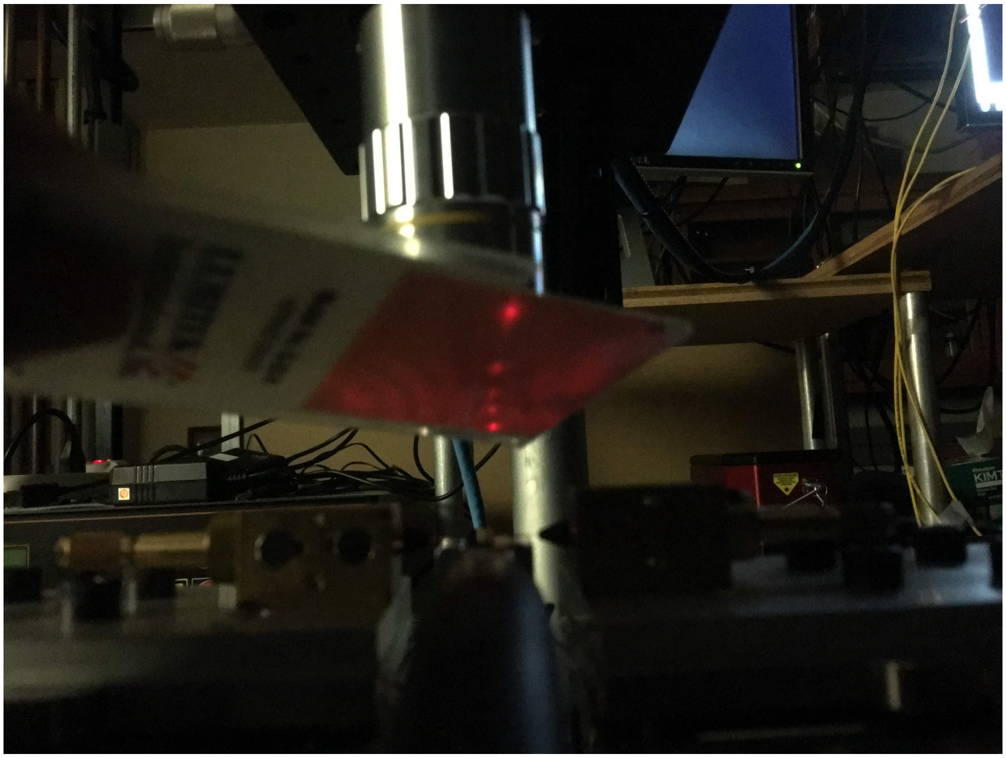

Figure 1.2. Far field emission with multiple lobes from a 5 μm pitched OPA.

beam steering scheme, this could be retrieved by putting $\Delta\phi = \pm\pi$ into eq.1.6. Then the unambiguous range is given by:

$$-\sin^{-1}\left(\frac{\lambda}{2d}\right) \leq \theta \leq \sin^{-1}\left(\frac{\lambda}{2d}\right) \tag{1.8}$$

When $d < \lambda$, a single-lobe steering range is defined as the range in which higher order grating lobes are not visible in the whole 180°range, as illustrated in Fig. 1.4. This range is given by:

$$\frac{d}{\lambda} < \frac{1}{1+\sin|\theta|} \tag{1.9}$$

Especially, when $d = \lambda/2$

$$-90^\circ \leq \theta \leq 90^\circ \tag{1.10}$$

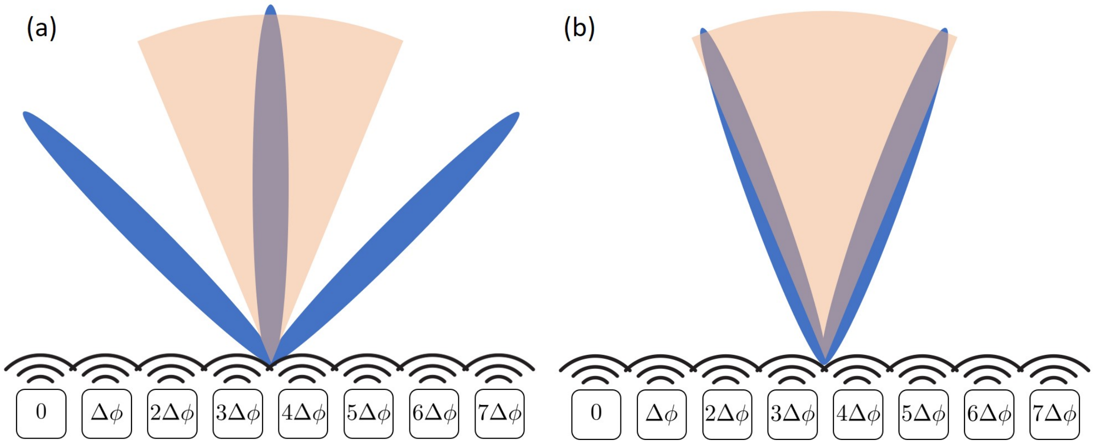

Figure 1.3. Illustration of the unambiguous beam steering using an example phased array with $d = \sqrt{2}\lambda$. The pink shaded area indicates the unambiguous range. (a) $\Delta\phi = 0$ and (b) $\Delta\phi = \pm\pi$

The equation shows that if the spacing of the emitter array d is set to $d \leq \lambda/2$, both the unambiguous and single lobe beam steering range will be the full visible range of 180°. Thus aliasing-free beam steering is achieved.

Another critical aspect of the emitted pattern is the far field beam width, often defined as the full-width half maximum (FWHM) of the optical beam. This FWHM represents the spatial resolution of the OPA and could be expressed as[9]:

$$\Delta\theta_{3\mathrm{dB}} = \frac{c_1}{\cos\theta}\frac{\lambda}{Nd} \tag{1.11}$$

where $\Delta\theta_{3\mathrm{dB}}$ (in radian) is the FWHM of the emitted beam, θ is the steering angle discussed earlier. And N is the number of emitters. Thus Nd is the effective aperture size of the array. c_1 is a constant related to the emitted beam profile. For a uniform rectangular array, the power profile of the beam is a sinc function. And $c_1 = 0.886$ as a result of the solution of $\sin \pi x/\pi x = 1/\sqrt{2}$. For example, the resolution of an OPA-based LiDAR often requires 0.1° beam over ±30° for fine item identification at up to 200 m. At an operating wavelength of 1550 nm, the required array size would be about 0.9 mm.

While a half-wavelength pitched emitter array seems to be the most straightforward solution towards aliasing-free beam steering, the design is hard to realize due to the strong

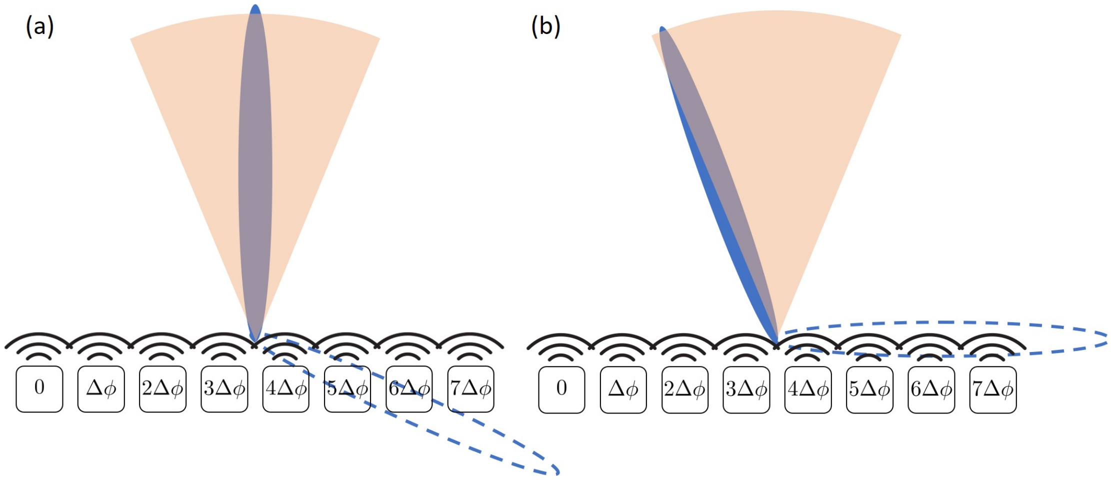

Figure 1.4. Illustration of the single beam steering using an example phased array with $d = \sqrt{2}\lambda/2$. The pink shaded area indicates the single beam steering range. The dashed lobes are theoretically predicted higher order lobes which are not in the visible range of $[-90°, 90°]$. Note the difference from Fig. 1.3.

evanescent coupling between waveguides at such a small waveguide spacing, which introduces phase and power error along the emitter array and greatly degrades the far-field beam-forming. Efforts have been made to achieve aliasing-free beam steering with different approaches. Sparse aperiodic arrays [10], [11] are used to break unwanted extra grating lobes through the randomized placement of the emitters and redistribute the optical power from the extra lobes over the full FOV as background. While achieving grating lobe-free beam steering, this design does not increase the power efficiency in the main beam and thus suffers from a lower signal-to-noise ratio (SNR) as a result of higher background. Index-mismatched waveguide array[2] achieves uniform half-wavelength pitched emitter array by limiting evanescent coupling between waveguides using propagation constant mismatch[12]. Due to the mismatch in the k-vector, this approach is currently limited to a 1-D edge emitter array, limiting the output beam steering and confinement in only one dimension. Furthermore, extra optical/mechanical components (e.g., cylindrical lens) are required for two-dimensional beam steering and confinement.

In this thesis, we demonstrate the optical phased array based on uniform half-wavelength spaced grating emitter array. Two-dimensional beam confinement and a record-high aliasing-free beam steering field-of-view of 135° from grating emitter are measured from a 32 channel

SiN/Si hybrid OPA. Evanescent coupling between waveguides are suppressed by metamaterial-based **e**xtreme **ski**n-**d**epth (e-skid) waveguides[13]. The e-skid waveguides utilize an alternating air-silicon multi-fin side cladding. The high index contrast of those sub-wavelength ridges provides strong anisotropy, which leads to faster decay of the evanescent wave for transverse electric (TE) input modes, thus limiting evanescent coupling between closely spaced waveguides. High emission power from the OPA is realized by using a silicon nitride (SiN) and silicon hybrid platform. Furthermore, we extend the concept of the half-wavelength-pitched emitter array to the design of a broadband 8×8 silicon photonics switch and an OPA design with two-dimensional end-fire emitter array.

2. DESIGN OF COMPONENTS FOR OPTICAL PHASED ARRAY

A typical OPA system requires four major components in general: a power splitter to divide the input light into different waveguides for emission; phase shifters tune the phase of each antenna; a group of recombiners will adjust the array into desired spacing and emitter array radiates to generate the desired pattern, as shown in Fig. 2.1. It is worth noting that an OPA could also be inversely used as a receiver. When used as a receiver, the phase shifters control the emitter array's direction to collect the light. And combiners (originally power splitters) combine the optical power to a single output. In this chapter, the design of those components will be discussed in detail.

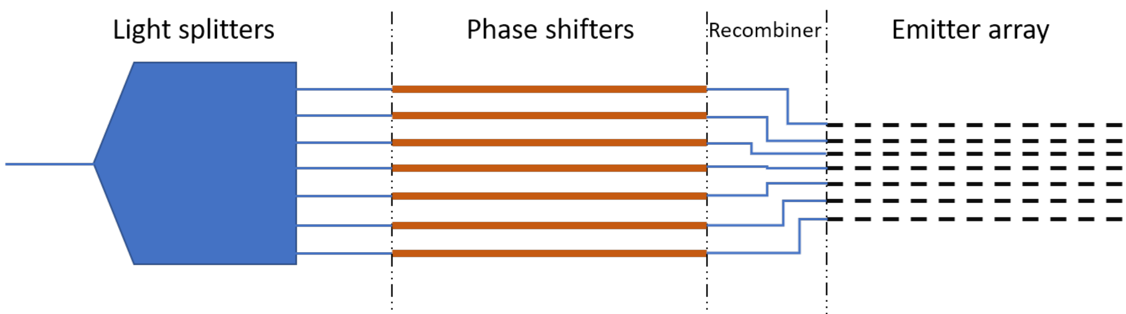

Figure 2.1. Essential components of an OPA: Power splitters, phase shifters, recombiners and emitter array.

2.1 Multimode interference couplers

Power splitters are arguably the most developed component in OPAs so far. 50:50 1×2 multimode interference (MMI) couplers are broadly used to split input light into 2^n channels through a n stage MMI tree. Cascade evanescent coupling has also been demonstrated to utilize cascaded optical phase shifters for simplified system control[14]. An example of the cascade evanescent coupler is shown in Fig 2.2. One drawback of this cascaded design is that as the portion of power coupled is different at each stage of the coupler, each coupler has to be designed separately and is thus less tolerant to potential fabrication variations.

The utilization of star couplers is also reported for natural Gaussian apodization in the emitters[15].

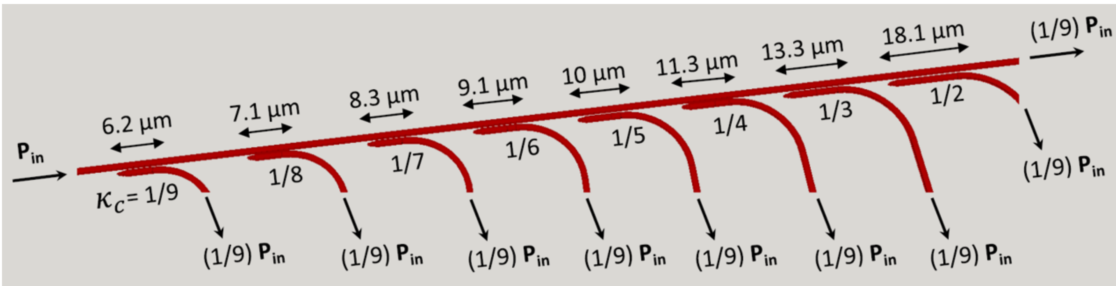

Figure 2.2. Example of cascade evanescent couplers, adapted from [9].

As discussed in chapter 1, OPAs for LiDAR application require large aperture size for small spot size in the far field. For example, an OPA with 1 mm aperture size and $\lambda/2$ spacing between emitters at 1550 nm would need an array of 1290 emitters. Moreover, if using a cascaded 1×2 MMI tree, 11 stages are needed. Thus, a low-loss design of MMI splitter is crucial. This section discusses the design of a low loss 1×2 MMI for both silicon on insulator (SOI) and silicon nitride (SiN) platforms.

A basic scheme of an MMI splitter is shown in Fig 2.3. Notice that for both input and output waveguides, a taper is included to reduce the possible reflection when the input mode is sent into the body of the MMI coupler. The gap between the two output tapers (taper gap in Fig 2.3) is always kept at > 50 nm to avoid sharp corners in the device that may be sensitive to fabrication variations.

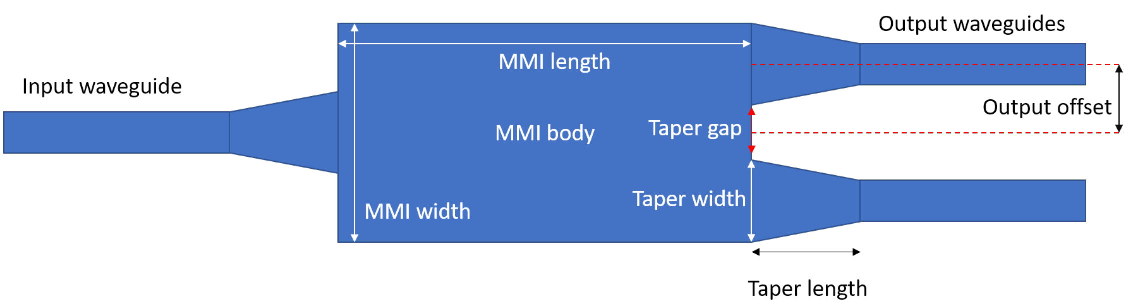

Figure 2.3. Basic scheme of a 1×2 MMI splitter, with parameters used in optimization.

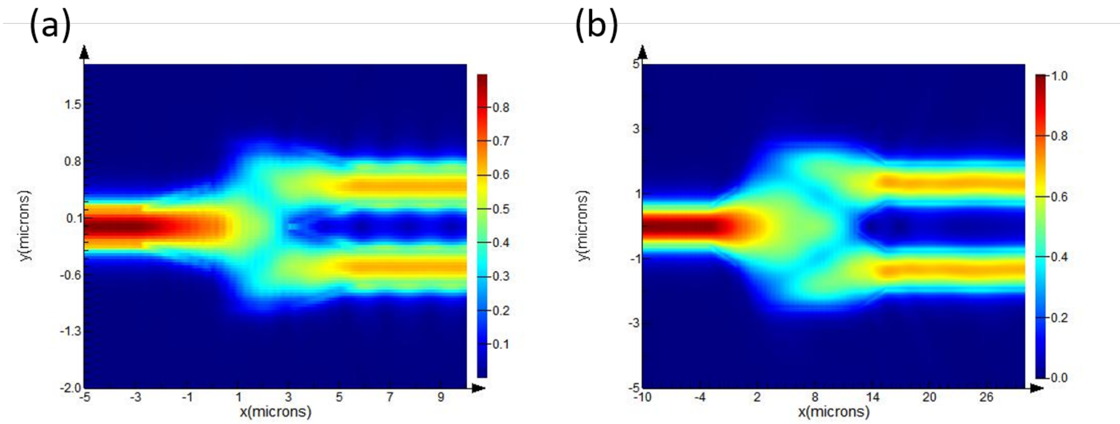

Figure 2.4. E-field distribution of designed MMI coupler in (a) SOI (b) SiN platform. E-field is sampled along the plane parallel to the center of the input waveguide.

Finite Difference Time Domain (FDTD) simulations were performed using commercial software Lumerical FDTD solution^{TM}. The result is shown in Fig 2.4 and Table 2.1. We can see that the simulated insertion loss (IL) of these two designs are well below 0.1 dB, making them suitable for use in large-scale OPAs.

Table 2.1. Design and performance of MMI in SOI and SiN platform

Parameter	**SOI**	**SiN**
Input waveguide (width×height, nm)	450×220	1200×300
MMI body length (um)	3	12.5
MMI body width (um)	2	5
Taper length (um)	2.8	3
Taper width (um)	1	2.34
Output offset (um)	0.5	1.33
Insertion loss (dB)	0.02	0.07

2.2 Silicon nitride - silicon (SiN/Si) power coupler

2.2.1 Introduction

Numerous high performance OPA demonstrations are on SOI platform, mainly because of the high refractive index of silicon. Silicon waveguides have strong optical confinement and allow emitters to be placed closer without evanescent coupling between adjacent emitters, pushing forward the dream-land where $d \leq \lambda/2$. There are already demonstrations of OPAs with half-wavelength spacing[2], [16]. However, these designs rely on the difference of propagation constant between adjacent waveguides to limit coupling between them and are therefore required to use edge emitters. These emitter arrays are hard to scale up. Furthermore, 1D edge emitter array has a large divergence angle in the other direction and is not suitable for autonomous vehicle applications. Another problem is that silicon waveguides cannot handle high optical power. And demonstrations of any SOI OPA system that can deliver high enough power for long-range detection are thus limited.

Silicon nitride, on the other hand, is also a popular material in silicon photonics. SiN can handle high optical power and is widely used in microresonators for Kerr comb generation. However, SiN waveguides suffer from low optical confinement due to their lower refractive index ($n = 2$ at 1550 nm compared to $n = 3.48$ for silicon at 1550 nm). Optical phased arrays in silicon-nitride platforms have been demonstrated [17], [18], but they all have relatively larger antenna pitch ($\sim 2\mu$m) in order to avoid crosstalk between emitters. To solve this problem, we designed a power coupler between silicon nitride and silicon waveguides to bridge between SOI/SiN platform. High emission power from OPA could then be achieved by using SiN waveguides for high optical power input and Si waveguides and emitters for small antenna pitch.

A further illustration of the benefit from a high power OPA in terms of its detection range could be derived from the LiDAR Equation[19]. Here the detected signal of a LiDAR system could be described as:

$$P(r) = KG(r)\beta(r)T(r) \tag{2.1}$$

where $P(r)$ is the detected power from an object at distance r. K is the system factor of LiDAR, determined by system parameters as input laser power, temporal pulse width *etc.*

The term $\beta(r)$ is the backscattering coefficient at distance r. And $T(r)$ describes the loss of light during the roundtrip to distance r. The geometric factor $G(r)$ is usually given by

$$G(r) = \frac{O(r)}{r^2} \tag{2.2}$$

where $O(r)$ is the overlap function determined by the emitter and detector optics. The r^{-2} term indicates the backscattered light being distributed onto a spherical surface with radius r. The quadratic decay of the detected signal to distance is in contrast with that of its radio-frequency counterpart, which decays quartically, and is due to the highly collimated output of LiDARs with large apertures.

As stated in Eq. 1.11, the divergence angle of OPA output is inversely proportional to its effective array size Nd. A large array aperture (usually millimeter scale) is required to achieve plane wave-like emission. For OPAs with a smaller number of channels, a focusing lens will be used to help collimate the beam within the detection range, thus maintaining the r^{-2} in the geometric factor. Due to its enhanced power handling capacity, a hybrid OPA can increase the detection length over Si OPAs. For example, a 256-channel hybrid structure could have 256 times the emitted power over that of a Si OPA, assuming that each emitter (the last stage in the distribution tree) of the hybrid OPA carries the same amount of power of the input waveguide (the first stage in the distribution tree) of the Si OPA. As a result, the hybrid OPA could achieve 16 times the detection range of a Si OPA with the same amount of channels.

2.2.2 Design

An overview of the implementation of the coupler design is shown in the layout in Fig. 2.5. First, high input power is sent into a SiN waveguide and then split into smaller portions through a cascaded 1×2 MMI tree. Next, when the power at the end of the MMI tree is low enough for a Si waveguide to handle, a SiN/Si coupler will couple the light from SiN waveguide to silicon. Finally, the array of Si waveguides will go through phase control and be adjusted into suitable array pitch and then emit through grating emitters.

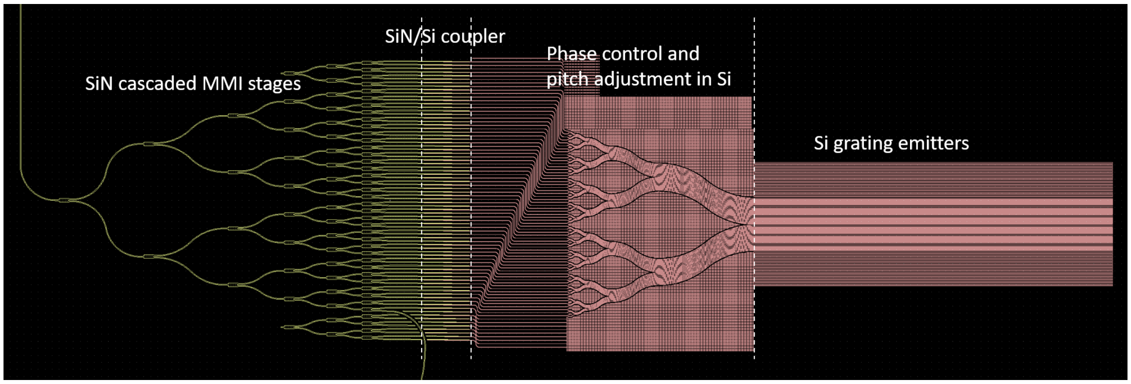

Figure 2.5. Scheme of implementing SiN/Si coupler to optical phased array design. Yellow waveguides are silicon nitride and pink ones are silicon.

A design scheme of the SiN/Si coupler is shown in Fig. 2.6a below. It consists of two tapers, one after the input SiN waveguide and the other before the output Si waveguide. The input optical mode in SiN will be expanded by the taper and will overlap with the expanded mode caused by the Si taper. As a result, the light will couple from SiN waveguide to Si. The two tapers are placed back-to-back to maintain a constant gap between SiN and Si. The size of the tip of the tapers is kept at 100 nm to reduce variation during fabrication; thus, we can achieve better phase and power uniformity. Fig 2.7 shows the process flow for the fabrication of the device. SiN and Si are on different layers. And the distance between two layers has been minimized to 200 nm for better device performance. FDTD simulation is performed to evaluate the performance of the device, as shown in Fig. 2.6b. The insertion loss of the device is 0.2 dB, which makes it suitable for application in large-scale OPAs.

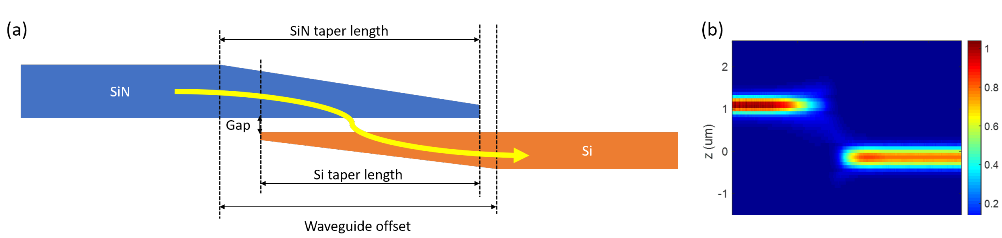

Figure 2.6. Design (a, top view) and simulation result (b, side-view) of a SiN/Si coupler. The blue waveguide is SiN and the orange one is Si. Yellow arrow indicates the direction of power coupling.

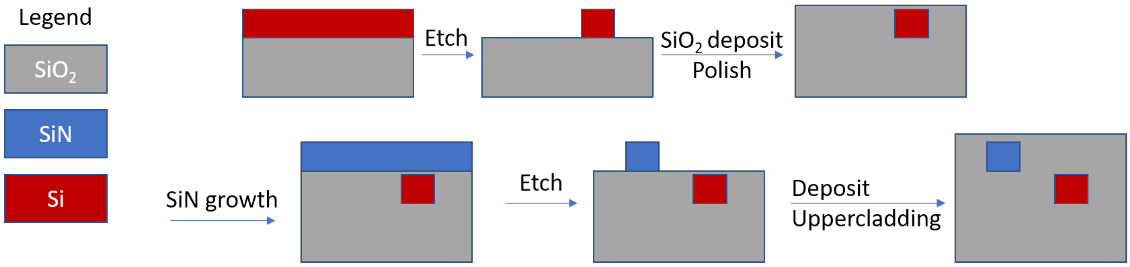

Figure 2.7. Simplified fabrication process flow for SiN/Si hybrid structure.

2.3 Phase shifters

Phase shifters are an important component in optical phased arrays. Most OPA system demonstrations features either thermal-optic phase shifters[14] or electro-optic phase shifters [20]. Liquid crystal based phase shifters are also reported[18]. The use of liquid crystal phase shifter is because that the SiN waveguide they chose to use at visible wavelength suffers from low thermal-optic coefficient and no significant electro-optic property. In this chapter, we will present our design and simulation of phase shifters, both electro-optic based and thermal-optic based.

2.3.1 Lithium niobate electro-optic phase shifter

Low-loss integrated lithium niobate (LN) modulators have been made possible thanks to the recent progress in LN thin film fabrication[21]. An example design of the LN phase shifter is shown in Fig. 2.8. The design utilizes a slab LN waveguide with a gold electrode on each side. We chose x-cut lithium niobate to yield the highest response from the applied electric field's horizontal component.

Assuming a uniform electric field E is applied to a LN waveguide, the refractive index change due to electro-optic effect is given by:

$$\Delta n = \frac{1}{2} n_{\mathrm{e}}^3 r_{33} E \tag{2.3}$$

thus shifted phase $\Delta\phi$ is

$$\Delta\phi = \frac{\pi}{\lambda} n_{\mathrm{e}}^3 r_{33} E L = 2\pi \frac{\Delta n L}{\lambda} \tag{2.4}$$

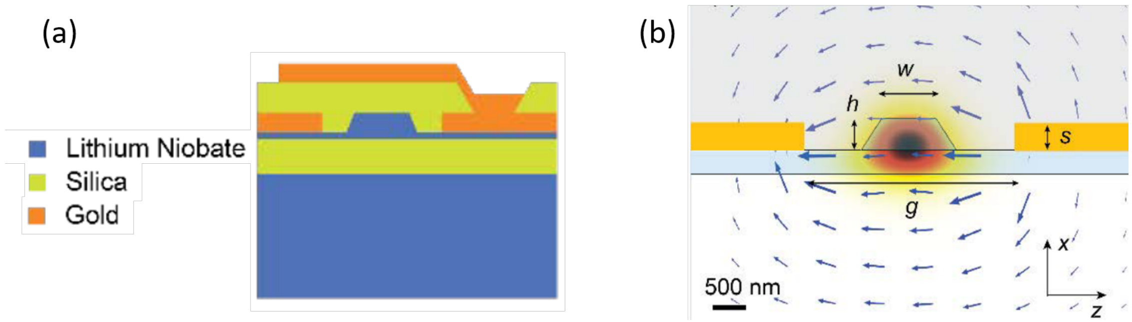

Figure 2.8. (a) Design of a LN phase shifter. (B) Optical TE mode in LN slab waveguide and applied electric field. Figures adapted from [21]

Here $n_e = 2.21$ is the refractive index of LN along the fast axis, $r_{33} = 31$ pm/V is the largest component in the electro-optic coefficients of LN. L is the length of the device λ is the operating wavelength. Simulation of a LN phase shifter is carried out using both Comsol® multiphysics and Lumerical mode solution™. The structure used in the simulation is shown in Fig. 2.9.

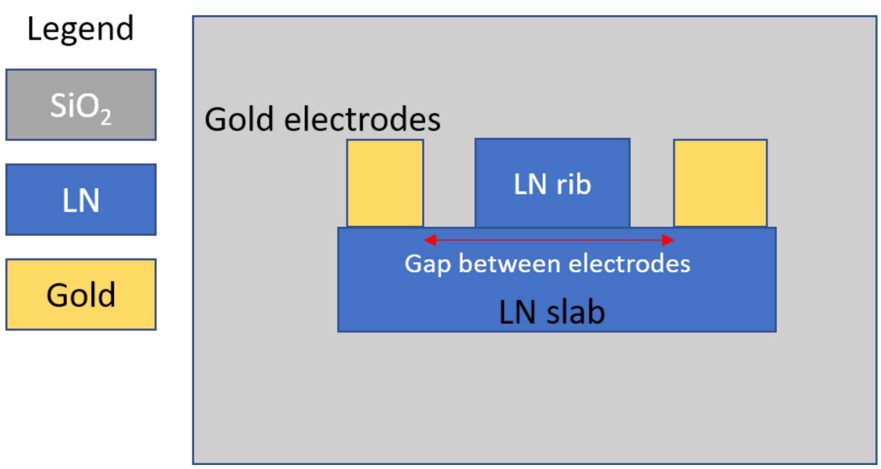

Figure 2.9. The cross section of the LN phase shifter used in simulations

One important aspect of the phase shifter is optical loss, which mainly comes from the absorption of the metal electrodes. As shown in Fig. 2.10, the size of the LN slab waveguide and the gap between gold electrodes are optimized to minimize optical loss while keeping the electrodes as close as possible. The finalized design is tabulated in Table 2.2.

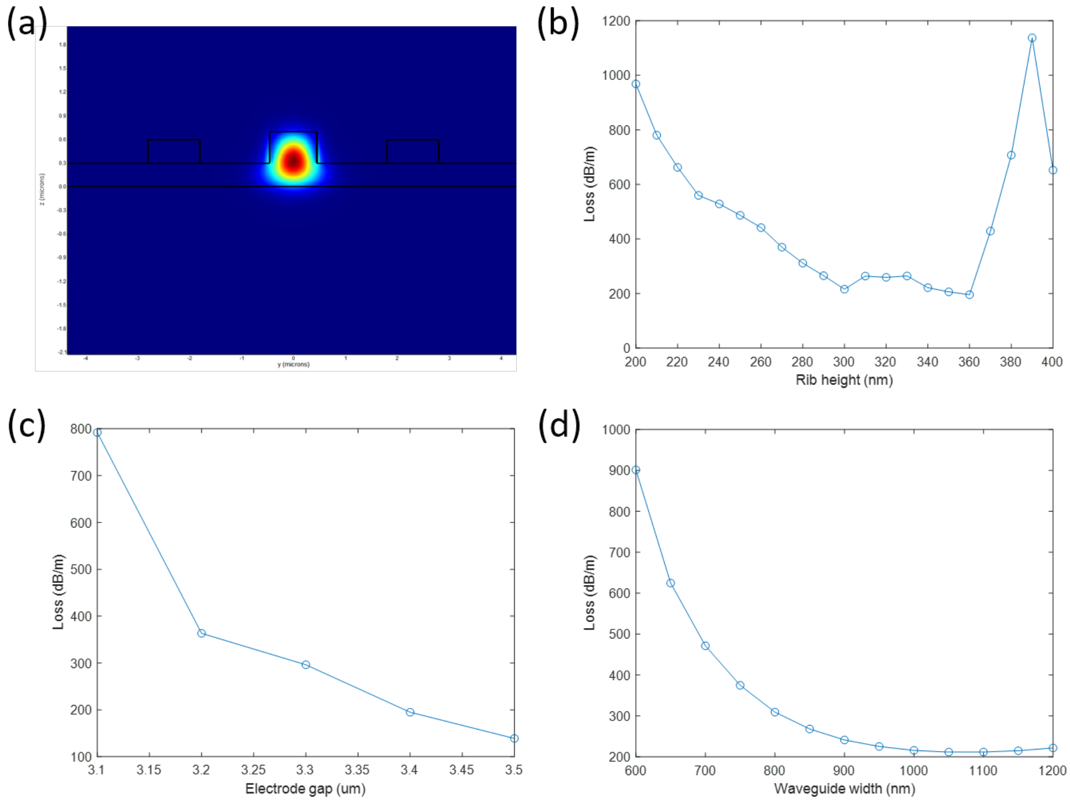

Figure 2.10. (a) Simulated optical TE mode profile. (b-d) are the optical mode loss with respect to (b) rib waveguide height; (c) waveguide width and (d) gap between gold electrodes while keeping other parameters constant.

Electrostatic simulation of the designed device is then performed in Comsol multiphysics to determine Δn_{eff} of the LN waveguide under applied electric field. Once the coefficient α in

$$\Delta n_{\mathrm{e}ff} = \alpha V_{\mathrm{in}} \tag{2.5}$$

is determined, following Eq. 2.4 we can get

$$V_\pi L = \frac{\lambda}{2\alpha} \tag{2.6}$$

(although in OPA applications, $V_{2\pi}L$ is of more interest, we still follow the widely accepted notation of $V_\pi L$ here).

Table 2.2. Design and performance of LN phase shifter

Parameter	Value
LN rib waveguide (width×height, nm)	870×360
LN slab height (nm)	240
Electrodes gap (μm)	3.5
Optical mode loss (dB/cm)	1.39

The simulation result is shown in Fig. 2.11. The electric field in both rib waveguide and slab are simulated with Comsol multiphysics, and the resulting change in material index is put into Lumerical mode solution to find corresponding Δn_{eff}. The simulation result shows $\alpha = 2.35\times10^{-5}$. Thus, the performance of the device is $V_\pi L = 3.3$ V×cm, comparable to that of integrated LN modulators. Thus, these LN electro-optic phase shifters can integrate with silicon photonics through techniques like wafer bonding and are expected to be a promising solution for phase shifters in OPA.

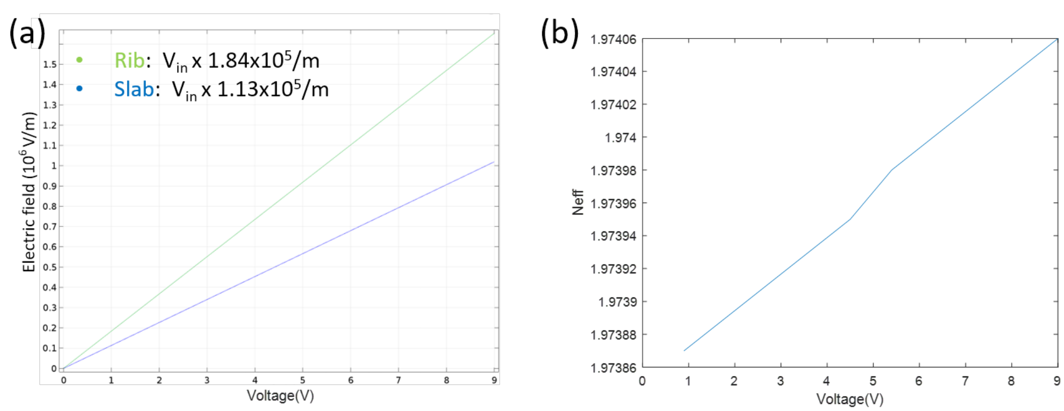

Figure 2.11. Simulated (a) Electric field in waveguide; (b) effective index with respect to input voltage.

2.3.2 Thermal-optic phase shifter

Another broadly adapted phase shifter used in optical phased array design is microheater-based thermal optical phase shifters. Those phase shifters are easy to implement but often have high power consumption and high thermal crosstalk. In this section, the design and simulation of a low-power thermal phase shifter are discussed.

The traditional design of a thermal-optic phase shifter is usually a straight heater wire on top of the waveguide. The waveguide is also cladded with a thick top cladding (usually $> 2\mu$m) to avoid optical absorption from the resistor wire. As shown in Fig. 2.12(a) and (c), because SiO_2 has a low thermal conductivity ($\kappa = 1\text{Wm}^{-1}\text{K}^{-1}$), most heat is conducted onto the silica cladding instead of the waveguide itself in this design.

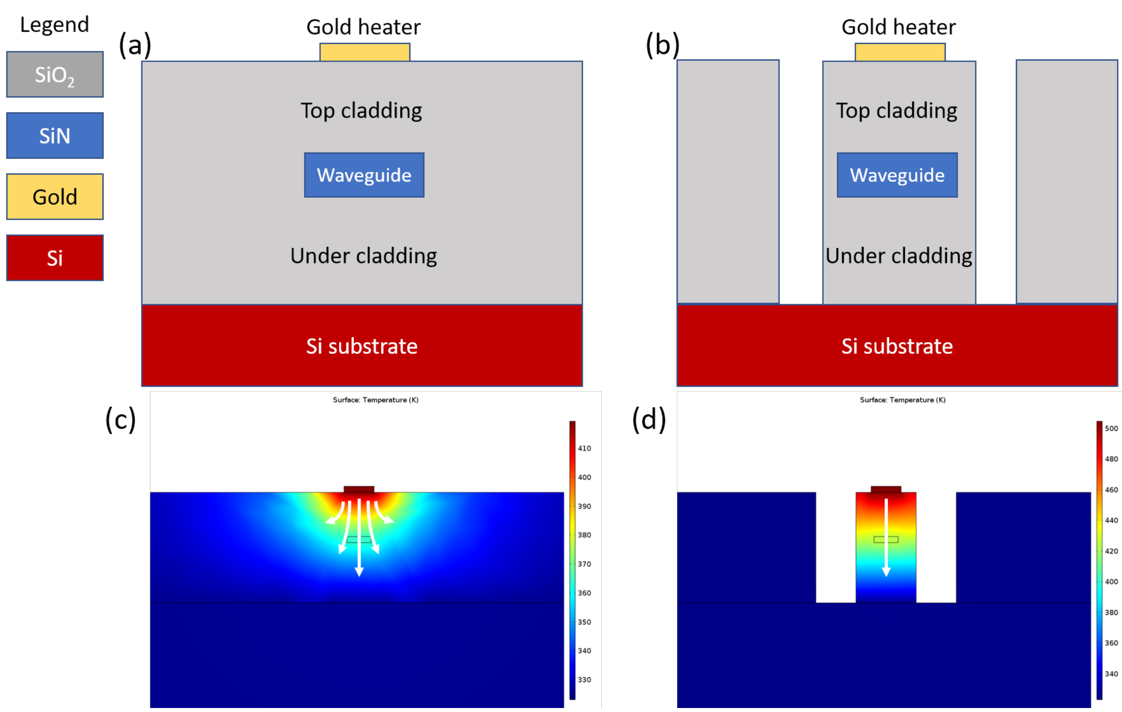

Figure 2.12. Cross section of the heater design. (a) Traditional heater line. (b) Etched heater design. (c) Thermal simulation of design (a); (d) Thermal simulation of design (b). (c) and (d) are done using Comsol multiphysics using the same boundary condition. Top cladding thickness = 2μm; under cladding thickness = 3.5μm;

Our improved heater design is shown in Fig. 2.12(b), where both the top and under cladding around the heater are etched. As air is an even worse heat conductor compared to SiO_2, this will effectively isolate the waveguide being heated and redirect more heat onto the waveguide. Corresponding thermal simulation is shown in Fig. 2.12(d). We can see that when the cladding around the waveguide is etched, the waveguide is heated to 430 K compared to 360 K in Fig. 2.12(a). The ambient temperature in the simulation is set to room temperature (300 K), showing that the improved design has a 100% increase in heating efficiency. Power consumption calculated from the simulation is 0.2 W per 2π phase shift from the following formula:

$$\Delta\phi = 2\pi\frac{\Delta nL}{\lambda} = 2\pi\frac{\alpha\Delta TL}{\lambda} \tag{2.7}$$

where $\alpha = 2.4 \times 10^{-5}\mathrm{K}^{-1}$ is the thermo-optic coefficient of silicon nitride.

This power consumption could be further improved by implementing a much thicker under cladding. When thermal equilibrium is reached, all the heat generated by the heater is dissipated into the Si substrate (here we assume that heat conducted by air is negligible and silicon is a good enough heat conductor with $\kappa = 148\ \mathrm{Wm}^{-1}\mathrm{K}^{-1}$, so that Si substrate stays at near room temperature). Following Newton's cooling law, the temperature distribution is linear from the heater to the substrate when the structure is well isolated (as shown in Fig. 2.12(d)). Making the under cladding thicker effectively brings the waveguide closer to the heater than the substrate (which acts as a heat sink here). In return, the power needed from the heater to keep the waveguide at the desired temperature is significantly reduced, shown in Fig. 2.13.

The accumulated phase of the waveguide increased from 1 radian to 4.3 radians when the etched cladding thickness went from 3.5 μm to 22.5 μm. As a result, our single heater wire can now produce 2π phase shift with as little as 50 mW input electric power. But the benefit of thicker under cladding comes with a longer thermal response time, which we will be discussing below.

Optical phased array-based LiDAR system requires rapid beam steering for both high resolution and frame rate. The response time of the phase shifter is crucial in acquiring that. Fig. 2.14 shows the simulated rising and falling edges of a heated SiN waveguide shown in Fig. 2.12(b). The rise time is defined as the time required for the response to rise from 10% to 90% of its final value[22] (and 90% to 10% for fall time). The yellow and purple lines in the figure indicate the 10% and 90% of the output step height. As a result, the rising edge

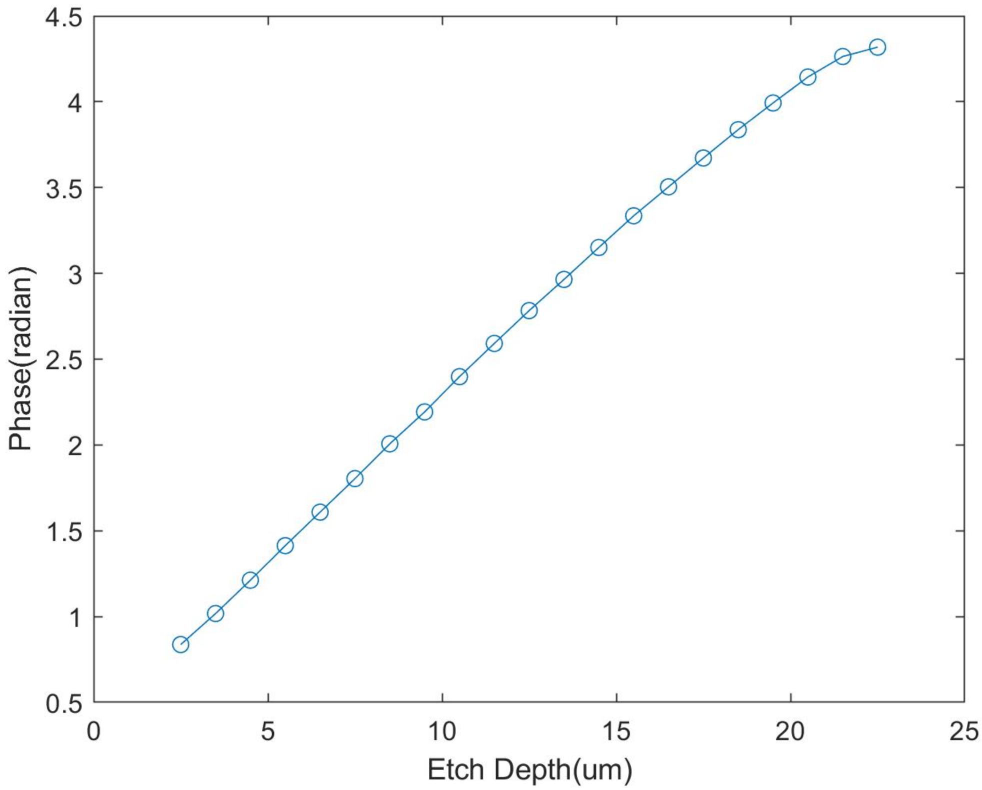

Figure 2.13. The amount of phase accumulated along heater with increasing undercladding thickness (cladding beside waveguide is fully etched). Simulated using the same input voltage for the heater.

of the simulated SiN thermal-optic phase shifter is $\sim 30\ \mu$s, and the falling edge is less than 50 μs from a 1.2 V voltage pulse.

To emulate the case of fast sweeping, a group of step function is sent into the heater wire for simulation, as shown in Fig. 2.15. A total of 25 increasing voltage steps are sent in 5 ms. From Fig. 2.15 bottom, we can see that the phase response from the waveguide follows the trend of the input voltage. However, due to the excessive heat accumulated, we failed to observe any clear step in the phase response after 3 ms of heating. This shows that 0-2π phase sweep within 5 ms is possible, indicating a scanning rate of at least 200 lines per second. In order to have more precise beam positioning, a shorter rising/falling time is required to have a sharper phase response.

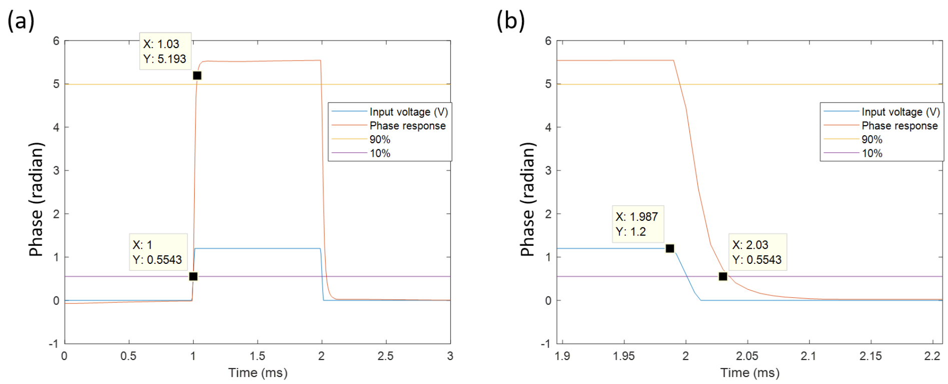

Figure 2.14. The (a) rising and (b) falling edge of the phase response from the heated silicon nitride waveguide. Simulated by sending in a 1.2 V voltage pulse into the heater. Under cladding thickness is 3.5 μm.

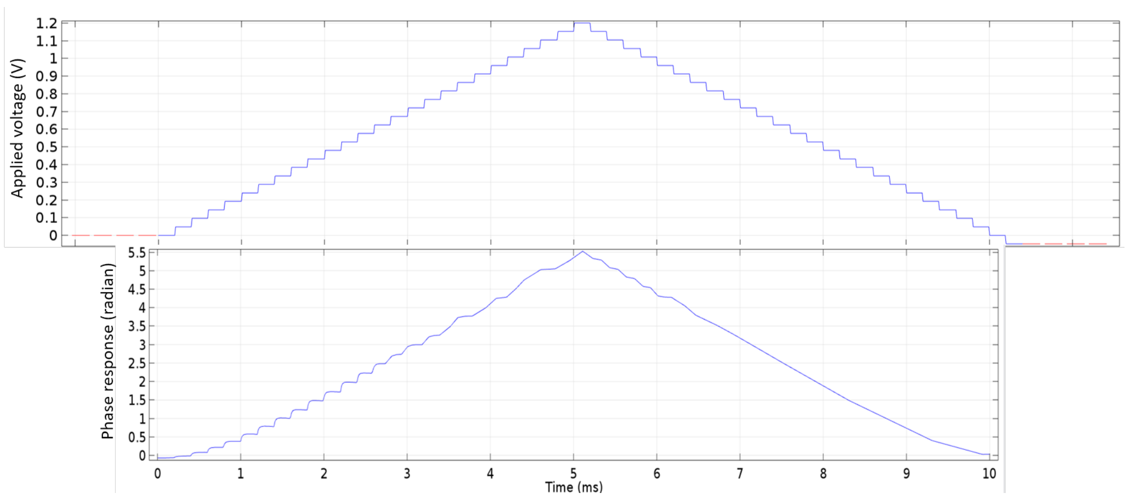

Figure 2.15. Simulation of a continuous voltage sweep of the heater wire. Top is the input voltage; Bottom is the Accumulated phase from the heated waveguide.

The performance could be further improved by implementing either an external cooling system or a design for lower heater power. The latter may be accomplished through the use of silicon waveguide instead of SiN, which has a thermo-optic coefficient of $1.8 \times 10^{-4}\text{K}^{-1}$, one order of magnitude higher than that of SiN. As shown earlier in Fig. 2.13 and 2.14, thicker under cladding requires less power for phase shifting at the price of slower scanning speed. For thermo-optic (TO) phase shifters on Si waveguides (for designs on both Si and hybrid platform), standard cladding thickness could be used to achieve a potentially faster scanning speed. Fig. 2.16 shows the simulated rising and falling edges of a heated silicon waveguide. The rising edge is 30 μs, and the falling edge is 34 μs from a 0.4 V voltage pulse for $0-2\pi$ phase sweep, showing that Si waveguides are $\sim$ 30% faster in phase response compared to SiN waveguides shown in Fig. 2.14.

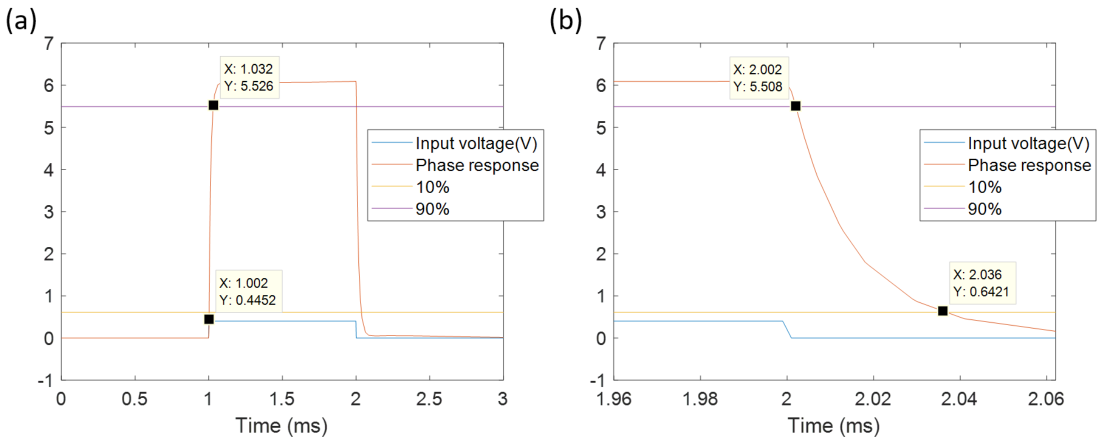

Figure 2.16. The (a) rising and (b) falling edge of the phase response from the heated silicon waveguide. Simulated by sending in a 0.4 V voltage pulse into the heater. Under cladding thickness is 2 μm.

2.4 Emitter array

The emission from a grating emitter in the longitudinal direction (i.e., the direction along the waveguide) is pointed towards ϕ as illustrated in Fig. 2.17 where [23]

$$\sin \phi_N = \frac{n_{eff} - N\lambda/a}{n_{cladding}} \tag{2.8}$$

here n_{eff} is the effective index of the grating and $n_{cladding}$ the index of cladding. a is the grating period. In a broadly accepted case where silica upper cladding is used, $n_{cladding} = 1.44$ at 1550 nm. Notice that ϕ_N is used to represent the emission angle of the N_{th} lobe of the grating. As discussed in earlier chapters, multiple lobes of emission should be avoided as it redirects power from the main lobe to grating lobes, thus reducing the overall emission efficiency of the main lobe. In our design, we usually set $n_{eff} = \lambda/a$ to make sure that only the $N = 1$ lobe is supported. We can steer the output beam in the longitudinal direction by changing the input wavelength.

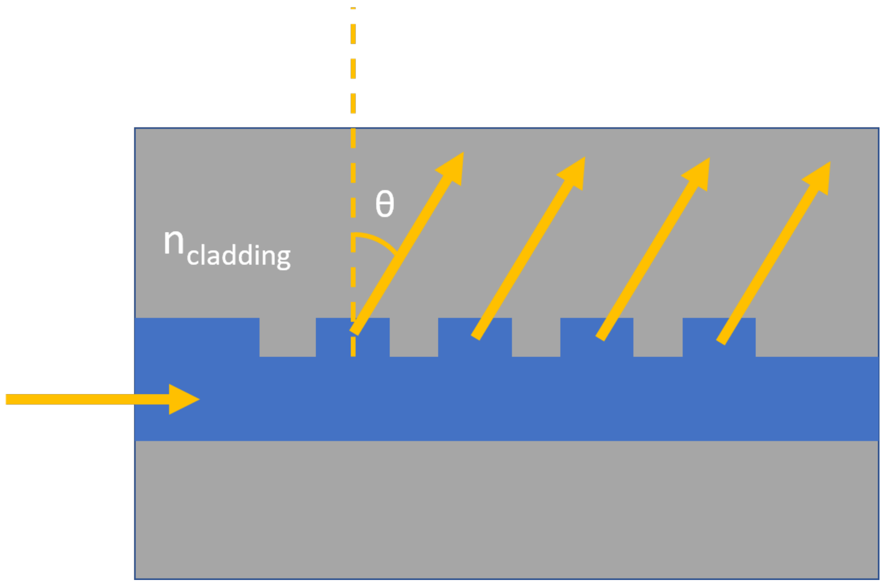

Figure 2.17. Illustration of the emission angle ϕ in a grating coupler.

A grating emitter is realized mainly through periodic perturbation of the waveguide. The strength of emission correlates with the scale of the perturbation. For uniformly distributed perturbation along the grating, a linear attenuation model may be applied

$$I(z) = I(0)\mathrm{e}^{-\alpha z} \tag{2.9}$$

where α is the attenuation constant related to the emission strength of the grating. For a grating emitter of fixed length, larger α (in absolute value) leads to more power emission. However, as the emitted power decays exponentially along the grating, larger α will lead to smaller effective aperture size and larger beam divergence. To quantify this effect, we can rewrite Eq. 2.9 to its normalized form

$$I(z) = I(0)\mathrm{e}^{-(\alpha L)\times z/L} \tag{2.10}$$

$$I(L)/I(0) = \mathrm{e}^{-(\alpha L)} \tag{2.11}$$

where L is the total length of the grating, which makes αL the normalized attenuation constant (which is unitless). Assuming negligible loss from the grating itself, the far field beam divergence angle is proportional to αL and emitted power is proportional to $1 - e^{-\alpha L}$. Fig. 2.18 shows the simulated result of the total emitted power with respect to the attenuation constant. Using $L = 1$ mm and $\lambda = 1550$ nm, αL between 1.7 and 2.2 is considered a good trade-off between emission and beamwidth. Around 85% to 90% of the power is emitted in this region, and the beamwidth is $\sim 0.17°$.

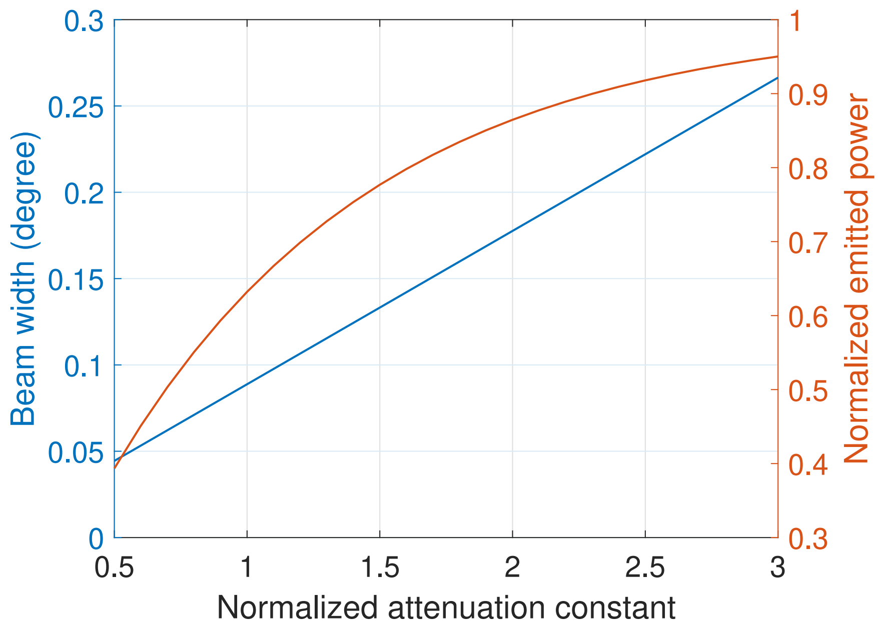

Figure 2.18. Simulation of beam divergence angle and emitted power with respect to emission strength. The simulation uses $L = 1$ mm and $\lambda = 1550$ nm.

Other approaches have been made to maximize the aperture size from a grating of fixed length. Apodization of the grating for larger aperture has been demonstrated by increasing the emission strength along the grating to compensate for the exponential decay[24]. n_{eff} and grating period a is matched along the grating to ensure that the output beam is always emitted to the same direction.

Perturbation on the grating is mainly realized in two ways: either at the top of the grating (top-etched grating) or on the sides of the grating (sidewall grating), as shown in

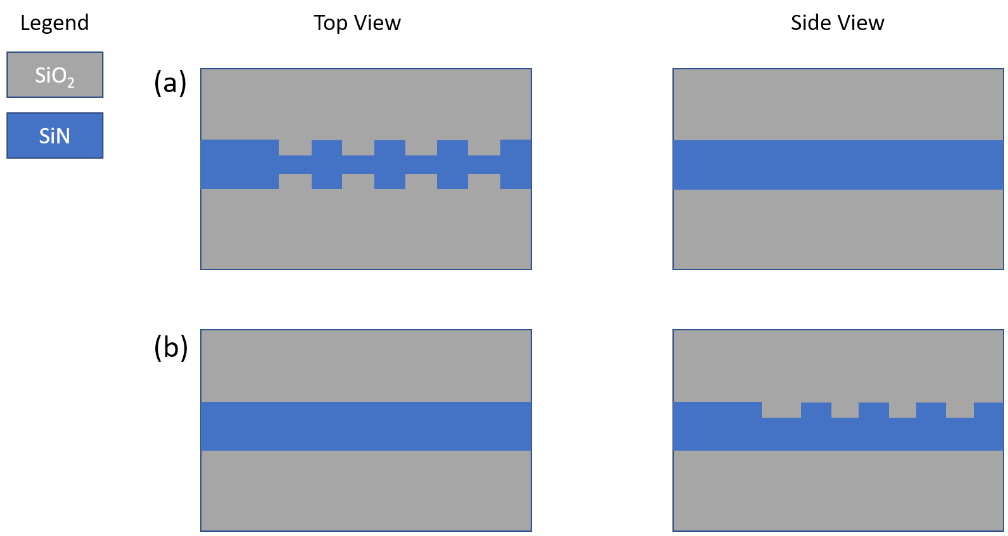

Figure 2.19. Illustration of different grating types. (a) sidewall grating. (b) top-etched grating.

Fig. 2.19. As for fabrication, sidewall gratings are easier to fabricate as all the structures are of the same height and require only one exposure for patterning. However, the drawback is that sidewall gratings are up/down symmetric. Due to this symmetry, the power emitted from the top of the grating will always be 50% of the input power if the interference from the back-reflection of the substrate is omitted.

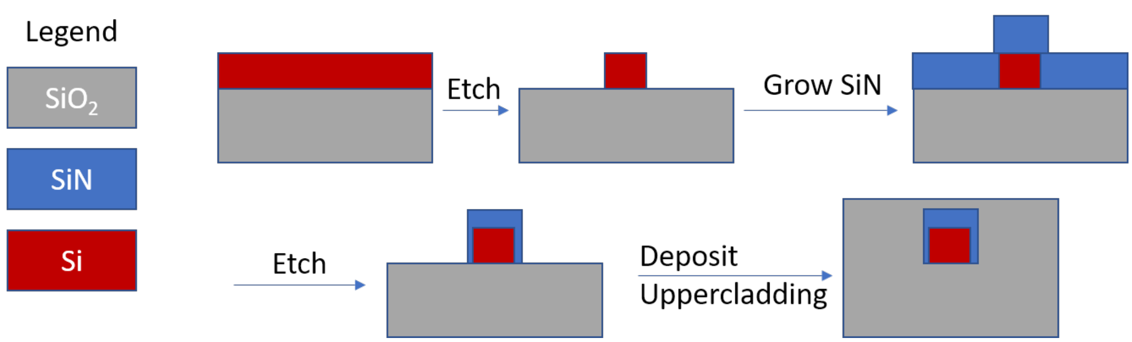

Figure 2.20. Proposed fabrication process flow for SiN/Si hybrid structure.

Breaking the vertical symmetry of the grating coupler is for potentially higher emission efficiency to the top with proper design[25]–[27]. The optimum condition is when there are two diffraction centers within each grating period. And the diffraction centers needs to be placed with a $\lambda/4$ offset both horizontally and vertically to achieve a complete constructive interference[28]. Unidirectional grating emitters based on two SiN layers have been demonstrated with a high directionality of >90%[29], [30]. This method utilizes two silicon nitride layers to acquire the $\lambda/4$ offset requirement between diffraction centers. The drawback of this design is that extra power splitting/phase control mechanisms need to be applied (e.g., adiabatic couplers[31]). And top-etched grating, by its nature, is capable of breaking this vertical symmetry. For our SiN/Si hybrid platform, we propose an alternative fabrication process to enhance the directionality of the top-etched grating, as shown in Fig. 2.20. SiN-cladded silicon structure could be achieved by following the procedure. And we designed a SiN/Si hybrid grating with high directionality by utilizing the interference between emission from SiN and Si layers. The SiN-cladded silicon is used as a single-mode waveguide as a whole; thus no power re-distribution between different material/layers is required during the operation. The design and simulation result is shown in Fig. 2.21. The parameters used are tabulated in Table 2.3, which shows a directionality of 88%.

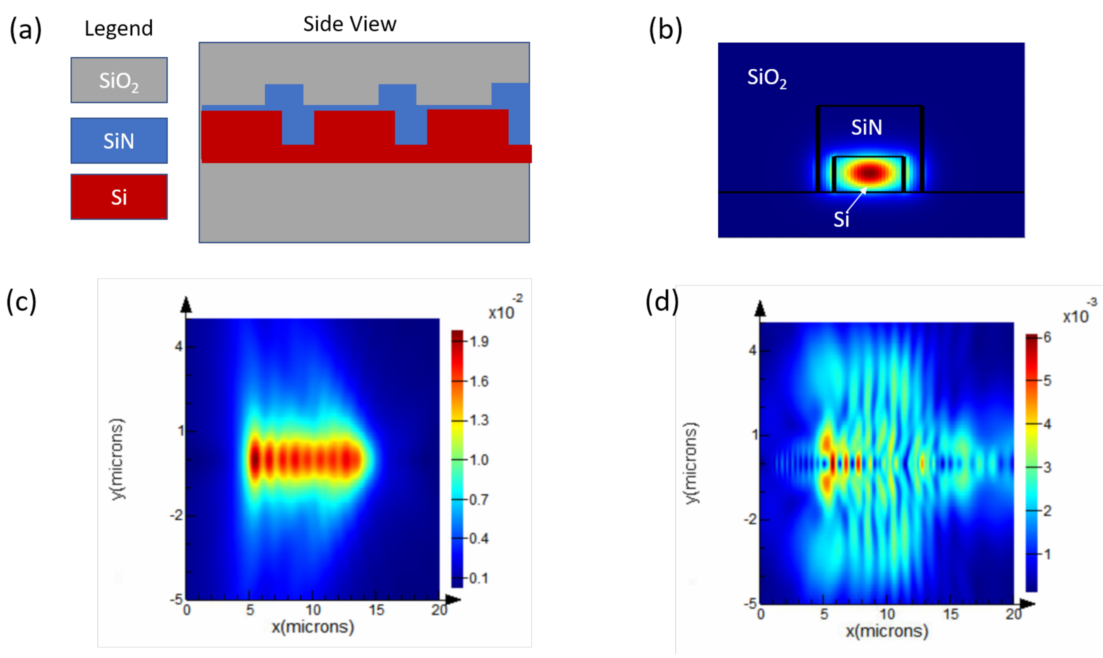

Figure 2.21. Design and simulation of the hybrid grating (a) Illustration of the grating design (b) Simulated mode profile in Si/SiN hybrid waveguide. (c) Simulated emission from the top of the grating. (d) Simulated emission from the bottom of the grating.

Table 2.3. Design and performance of SiN/Si hybrid grating

Parameter	Value
Si waveguide (width×height, nm)	490×280
SiN layer thickness (nm)	300
Si etch depth (nm)	12
SiN etch depth (nm)	200
Si grating duty cycle	70%
SiN grating duty cycle	60%
offset between Si and SiN grating (nm)	150
Directionality	88%

For the SiN cladded silicon waveguide, both Si and SiN are etched to form a set of top-etched grating on its own. Because the optical mode is still primarily confined in the Si part, as shown in Fig2.21(b), SiN layer is etched more than the Si to have comparable emission strength. Then the SiN grating is offset along the waveguide with respect to the Si grating to let the emission from those two gratings interfere constructively. As a result, the directionality of the hybrid grating is simulated to be 88% at an offset of 150 nm, which shows great potential for application in a high-efficiency OPA system.

For emitter spacing, as described by Eq. 1.8, an optical phased array system with spacing less than $d = \lambda/2$ can achieve the maximum possible unambiguous beam steering range of 180°. There has been several demonstrations of OPA with $d = \lambda/2$ [2], [16]. The $\lambda/2$ spacing is achieved by introducing propagation constant mismatch between adjacent waveguides to limit the maximum power coupling. However, those designs are based on edge emission with a pseudo-1D aperture, which makes the output beam diverges rapidly over the other dimension. This section will introduce our design of $\lambda/2$ spaced emitter array based on grating emitters for large emission aperture.

Recently reported extreme skin-depth (e-skid) waveguides use cladding pairs with small periodicity and high index contrast to shorten the decay length of evanescent waves, thus reducing evanescent coupling between waveguides at small pitch[13]. The schematic and simulated field profile of an e-skid waveguide with multilayer cladding is shown in Fig. 2.22.

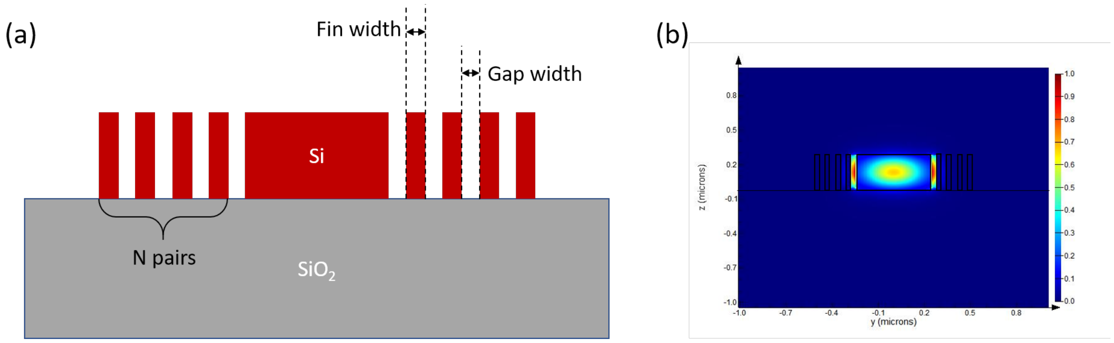

Figure 2.22. (a) Illustration of a e-skid waveguide with periodic cladding pairs (b) Simulated mode profile in e-skid waveguide.

The effectiveness of the e-skid structure is simulated using Lumerical mode solution. The simulation is based on the coupled-mode theory (CMT) for optical waveguides[32], where the coupling length L_c equals to

$$L_c = \frac{\lambda}{2(N_s - N_a)} \tag{2.12}$$

Here λ is the wavelength, N_s and N_a are the effective index of the symmetric and anti-symmetric supermodes. The structure used for coupling length simulation is shown in Fig. 2.23. And the simulated coupling length of the e-skid waveguides is shown in Fig. 2.25. In this simulation, we set the spacing between adjacent waveguides as 775 nm (half of the 1550 nm operating wavelength for aliasing-free beam steering) and set the number of cladding pairs besides the main waveguide to 5.

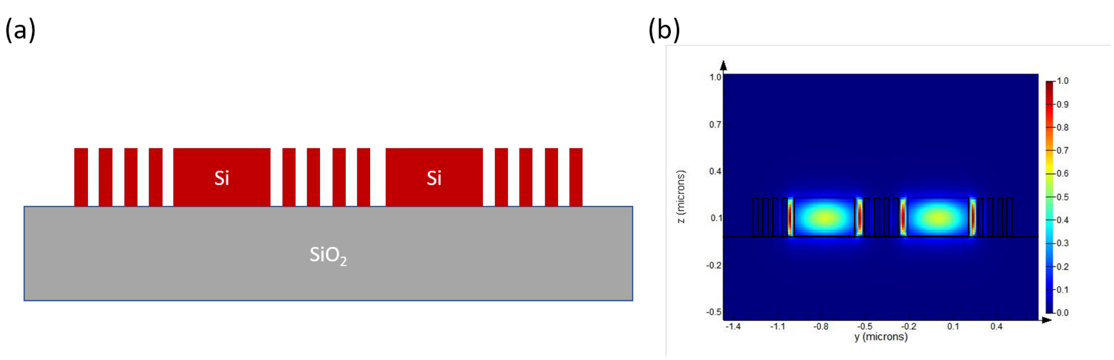

Figure 2.23. (a) Waveguide structure and (b) simulated mode profile used in coupling length simulation based on CMT.

During simulations using Lumerical software, it is worth noting that the result greatly depends on the grid size used in simulation. Fig. 2.24 contains results of coupling length simulation at different grid size. It could be seen that the result first oscillates and then converges beyond a certain grid size. In this case the result converges beyond a grid number of 140, which corresponds to a grid size of 15 nm. The simulations in this thesis are validated in a similar way that ensures the result to be converged.

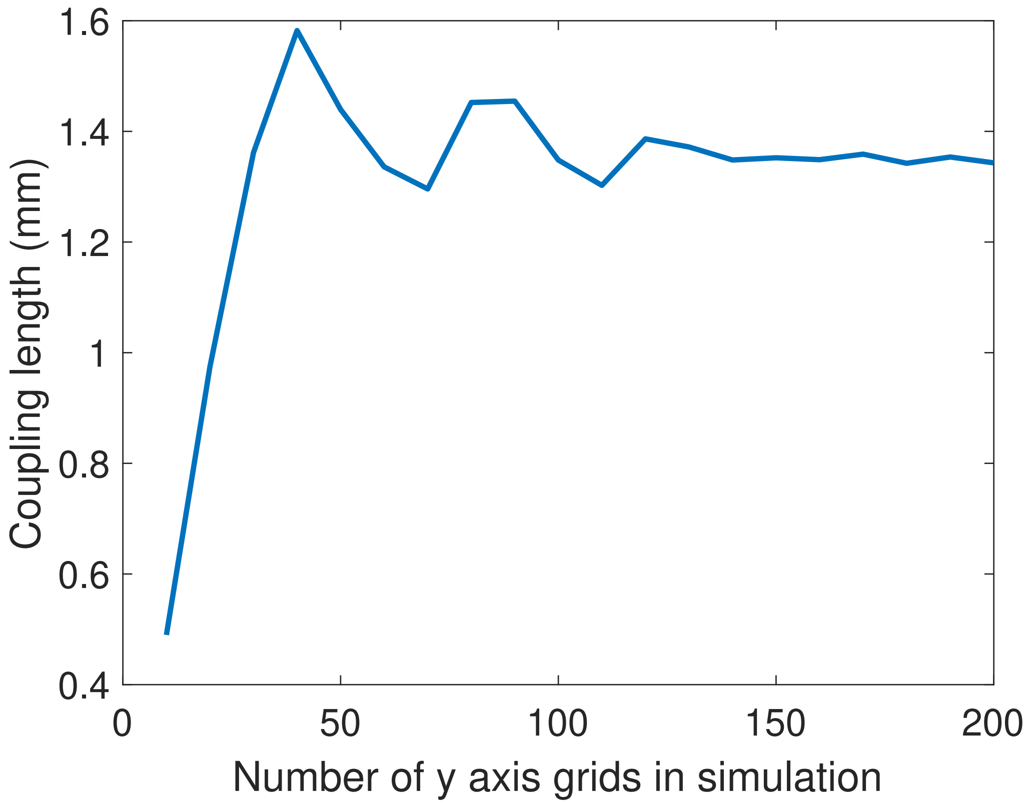

Figure 2.24. Simulated coupling length with respect to y-axis grids in simulation.

Fig. 2.25(a) shows that for an e-skid waveguide with five cladding pairs, its coupling length is at least 1 cm long in the single mode regime (400 nm$\times$ 220 nm to 500 nm$\times$ 300 nm) and could be as long as several tens of centimeters. Tolerance of fabrication error is also considered. Fig. 2.25(b) shows the coupling length when the dimension of the fabricated waveguide is offset from its designed parameter by $\pm$5 nm in either waveguide width or height.

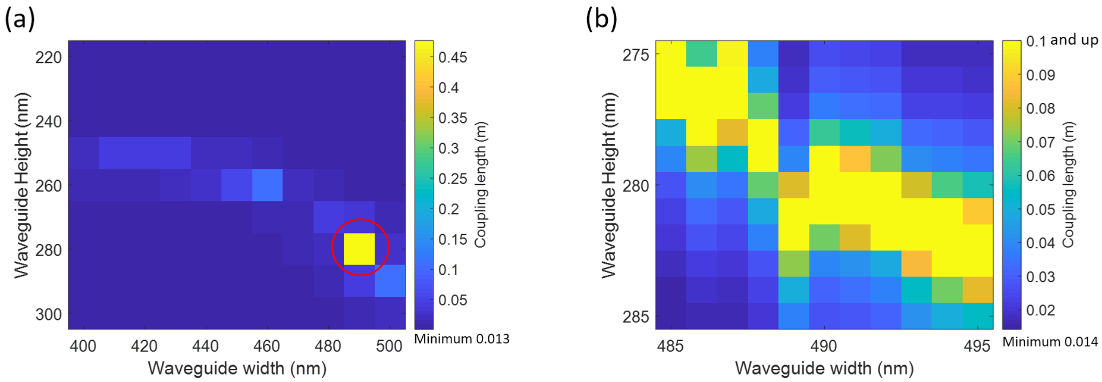

Figure 2.25. Simulation of the coupling length of the E-skid waveguide. (a) coupling length of the waveguide with respect to waveguide width and height. (b) Zoomed in view of the area indicated by the red circle in (a).

A coupling length of more than 10 cm could still be observed even when the waveguide has a slight variation in its dimensions, showing good robustness of the system.

To verify the performance of the e-skid structure, an array of e-skid emitters with spacing $d = 775$ nm and length $L = 200$ μm is simulated using Lumerical FDTD solution. Beam steering in the simulation is achieved by sending input modes with linear phase differences into the e-skid array. The far-field emission from the simulated array is shown in Fig. 2.26, indicating an aliasing-free beam steering in the range of $\pm 70°$. Notice that only the far-field image with $\Delta\phi$ of up to 70°is shown. Recall from Eq. 1.11 that the beam divergence angle of an OPA scales with $\frac{1}{\cos\theta}$. When the beam is steered further, the output beam also quickly broadens. At $\theta = 75°$, the beam width is already 3.8 times the original beam. Beams with larger θ are thus obviously not suitable for practical use due to their low power density.

2.5 Fabrication of the device

Yun Jo Lee performed the fabrication of the OPA devices in this thesis. This section introduces the fabrication process.

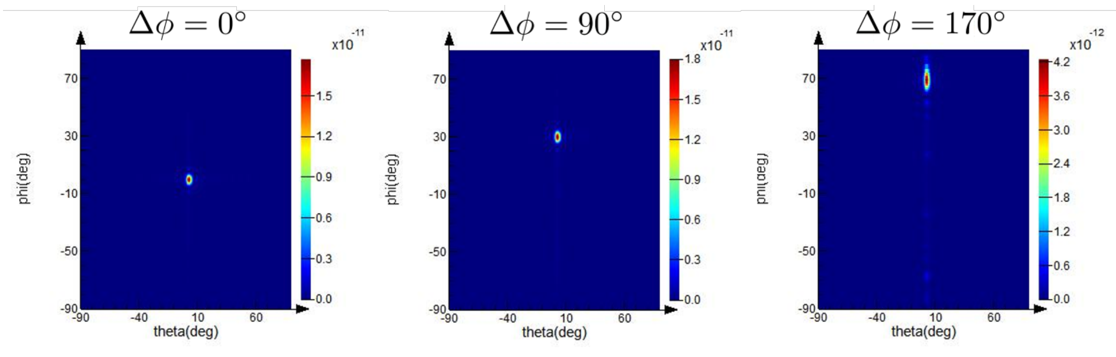

Figure 2.26. Simulated far-field emission from a e-skid emitter array. Phase difference $\Delta\phi$ in the array is (from left to right) 0°, 90°and 170°.

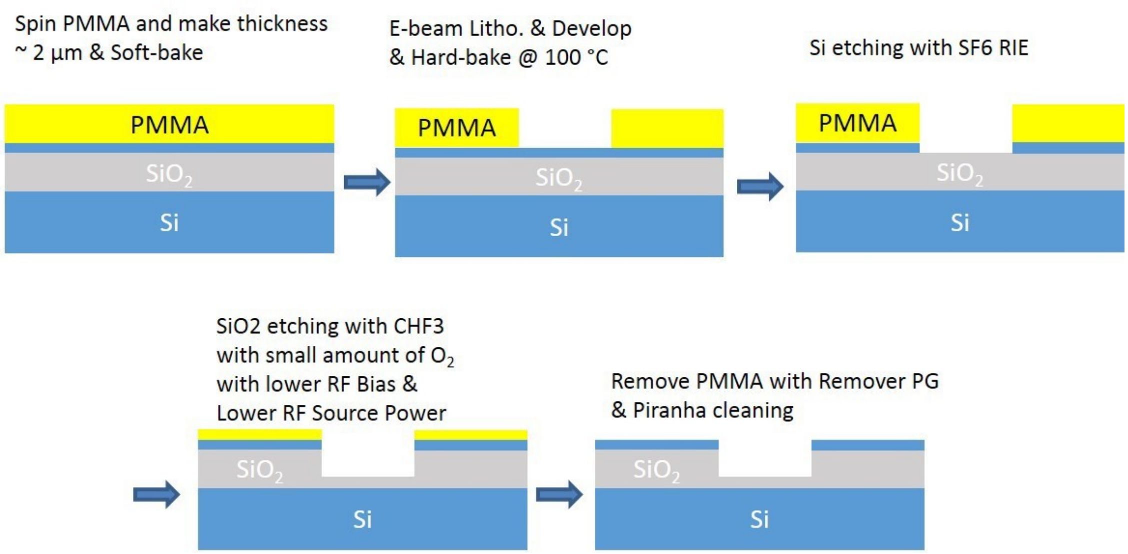

Figure 2.27. Fabrication process of alignment marks on SOI. Courtesy of Yun Jo Lee.

2.5.1 Fabrication of alignment marks

The fabrication of alignment marks on the SOI substrate is critical to the performance of the device, as the relative positioning between Si and SiN layers needs to be precise. Stoichiometric Si_3N_4 is widely used in photonic integrated circuit (PIC) applications due to its low propagation loss and broadband transparency. The most common way of deposition of stoichiometric Si3N4 is low pressure chemical vapor deposition (LPCVD) for its purity, low amount of defects, and uniform coverage. The typical selection of materials for alignment marks of the electron-beam (e-beam) lithography process is metals. Gold and platinum, for example, are preferred in semiconductor fabrication processes for their high contrast rate from the substrate during e-beam scanning. However, such metals are not compatible with the LPCVD silicon nitride deposition, which runs at 900°C. Therefore, etched alignment marks are chosen for our SiN/Si hybrid structure. The depth of those etched alignment marks on the SOI substrate needs at least 1.5 µm to obtain enough contrast during the e-beam processing.

The fabrication process of the etched alignment marks is shown in Fig. 2.27. Polymethyl methacrylate (PMMA) is spun onto the sample at 2000 rpm to achieve 2 µm thickness and then soft-baked at 180 °C for 90 seconds. The alignment mark patterns are then written using e-beam lithography with the dose of 2200 μC/cm^2. PMMA is developed afterward in the solution of 1:3 methyl isobutyl ketone : isopropyl alcohol (MIBK:IPA) for 2 minutes. The sample is then put onto the hot plate for hardbake at 100 $\circ$C for 1 minute. During the hardbake, the PMMA resist hardens and thus increases the chemical resistance for further etching. We used the reactive ion etching (RIE) process to etch the alignment marks. The RIE process can achieve the anisotropic shape of the etched geometry. Sulfur hexafluoride (SF6) is first used for minimizing the resist reduction during etching. Then RIE etching is performed with fluoroform (CHF_3) and O_2 for the deep etching of the buried oxide layer. Next, solvent stripper Remover PG is applied to the sample for more than 10 minutes. Then, the piece is soaked into Piranha solution, a mixture of sulfuric acid (H_2SO_4) and hydrogen peroxide (H_2O_2), which is a strong acid solution that can clean organic residue on the substrate. The cleaning process with piranha solution is essential for the fabrication of e-skid fin structures because the solution helps the silicon surface to be hydrophilic[33], which increases the adhesion between silicon surface and hydrogen silsesquioxane (HSQ). This allows for the integrity of the narrow fin structures during e-beam lithography and the development process.

Figure 2.28 presents the fabrication flow of the hybrid structure as the next step. First of all, e-beam resist XR-1541-004 is spun onto the sample at 6000 rpm. The resist is a 4 % HSQ resist diluted in MIBK solution. This spinning process creates an HSQ layer of 60 to 70 nm thickness. Then, the HSQ was soft-baked at 120 °C for 3 minutes on a hot plate. The Soft-baking process is critical for drying out the solvent inside the resist

Figure 2.28. Fabrication process flow of SiN/Si hybrid structure. Courtesy of Yun Jo Lee.

and increasing the adhesion between the silicon film and the resist. The e-beam writing of the silicon waveguide patterns is performed with the base dose of 900 μC/cm^2 with the customized proximity effect correction (PEC). The HSQ resist is developed through an 80-second immersion in 25 % Tetramethylammonium hydroxide (TMAH) solution. The sample is dipped into the solution of 6:1 buffered oxide etch (BOE) for 5 seconds and then rinsed the sample with distilled water to remove HSQ resist residue. The low-temperature oxidation (LTO) process deposits a thin layer of ($\sim$ 150 nm) silicon dioxide between silicon and silicon nitride layers. Stoichiometric SiN is deposited through LPCVD process to a total thickness of 300 nm. The e-beam lithography is then run for writing the Si3N4 waveguide structures. To fabricate the Si3N4 layer, flowable oxide - 16 (FOx-16) e-beam resist was spun with a spin rate of 8000 rpm. This produces a thicker ($\sim$ 600 nm) HSQ resist. The sample is soft-baked at 120 $\circ$C for 3 minutes on a hot plate. And e-beam writing of the patterns is done with the base dose of 1100 μC/cm^2 with customized proximity effect correction. RIE process with CHF3 and O2 is performed to etch the SiN. The remaining Fox-16 is removed by immersing the sample into BOE solution for $\sim$ 10 seconds and then rinsed with distilled water. Finally, the sample is put into the LTO chamber. Silicon dioxide is deposited as an upper cladding with a thickness of 2.5 μm.

During the fabrication process, it is worth noting that the air gaps in between e-skid waveguide fins are crucial for the device's performance. Preserved air gaps help maintain high index contrast in the multi-layer cladding, thus leading to faster decay of evanescent waves for less crosstalk in the waveguide array. Fig. 2.29 shows the simulated coupling length when different portion of the designed air gap is covered by SiO_2. At 100% coverage, the coupling length degrades to 1/7 of the original design (200 μm vs. 1.5 mm). Fig. 2.30 illustrates the process of depositing SiO_2 on top of e-skid fin array structures. As shown in Fig. 2.30b, the initially grown SiO2 on top of e-skid fin structures gradually closes the gap above the groove between silicon fins. This hinders the further deposition of silicon oxide into the gap, so, as a result, the air gap between e-skid cladding fins is preserved. Scanning electron microscope (SEM) images of the fabricated e-skid waveguide are shown in Fig. 2.31. To account for the minimum feature size in fabrication, the Si waveguide used is 450 nm$\times$220 nm. The number of cladding pairs is reduced to 4, yielding a minimum feature size of 36 nm.

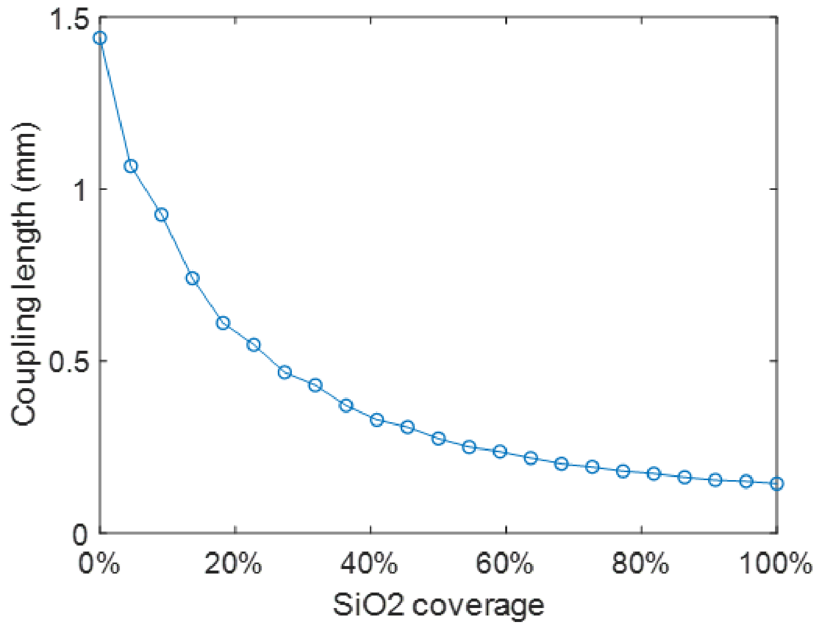

Figure 2.29. Simulation result of the coupling length of e-skid waveguide with respect to the portion of air gaps covered by SiO_2. The coupling length is extracted from CMT.

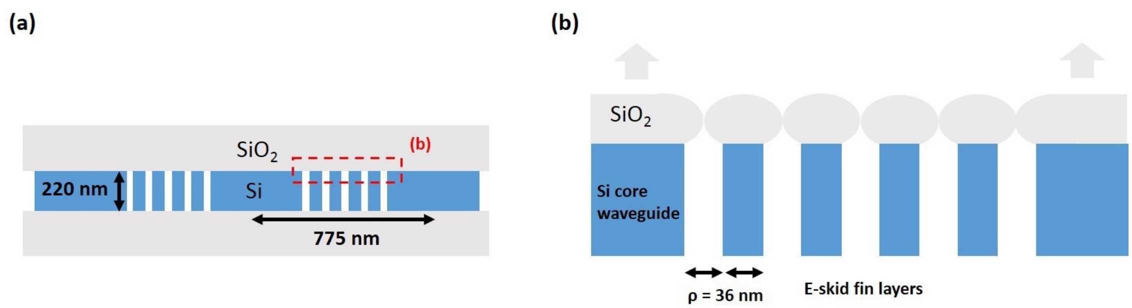

Figure 2.30. Illustration of preserving air gaps in e-skid fin structure. Courtesy of Yun Jo Lee.

Unlike sparse waveguide structures, the dense waveguide array in the OPA design is difficult to write using e-beam lithography because of the electron scattering effects. Once the focused electron beam hits the resist at the targeted area, it scatters in the resist layer first. This process is known as forward scattered electrons. After that, the e-beam scatters

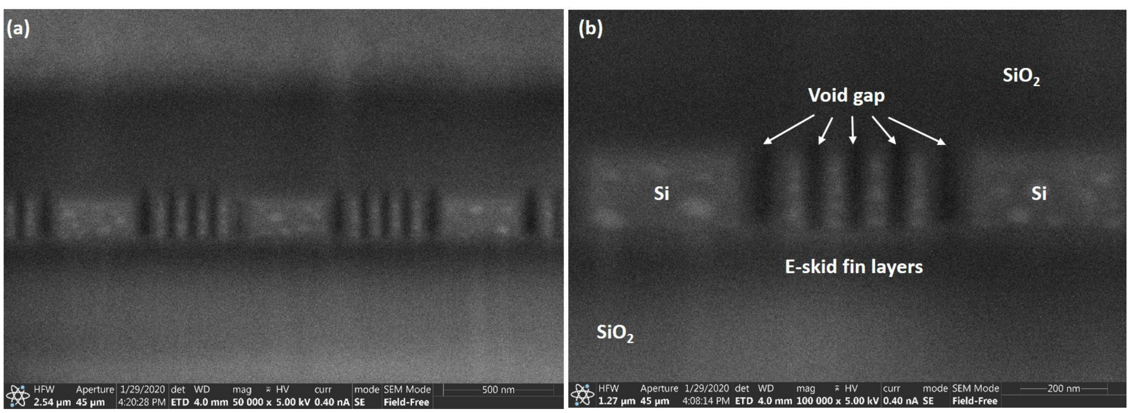

Figure 2.31. Cross-sectional SEM image of the fabricated device. Courtesy of Yun Jo Lee.

in the film or substrate material beneath. These back-scattered electrons create secondary electrons at the resist and substrate layers. These extra electrons add up to the total resist exposure dose, which leads to over-exposure of some dense patterns, known as the 'proximity effect'[34]. Therefore, different dose variations are applied to the device writing process in different pattern densities to correct the proximity effect. Fig. 2.32 and Fig. 2.33 show the effect of proximity effect on the fabricated devices and the device after proximity effect correction(PEC).

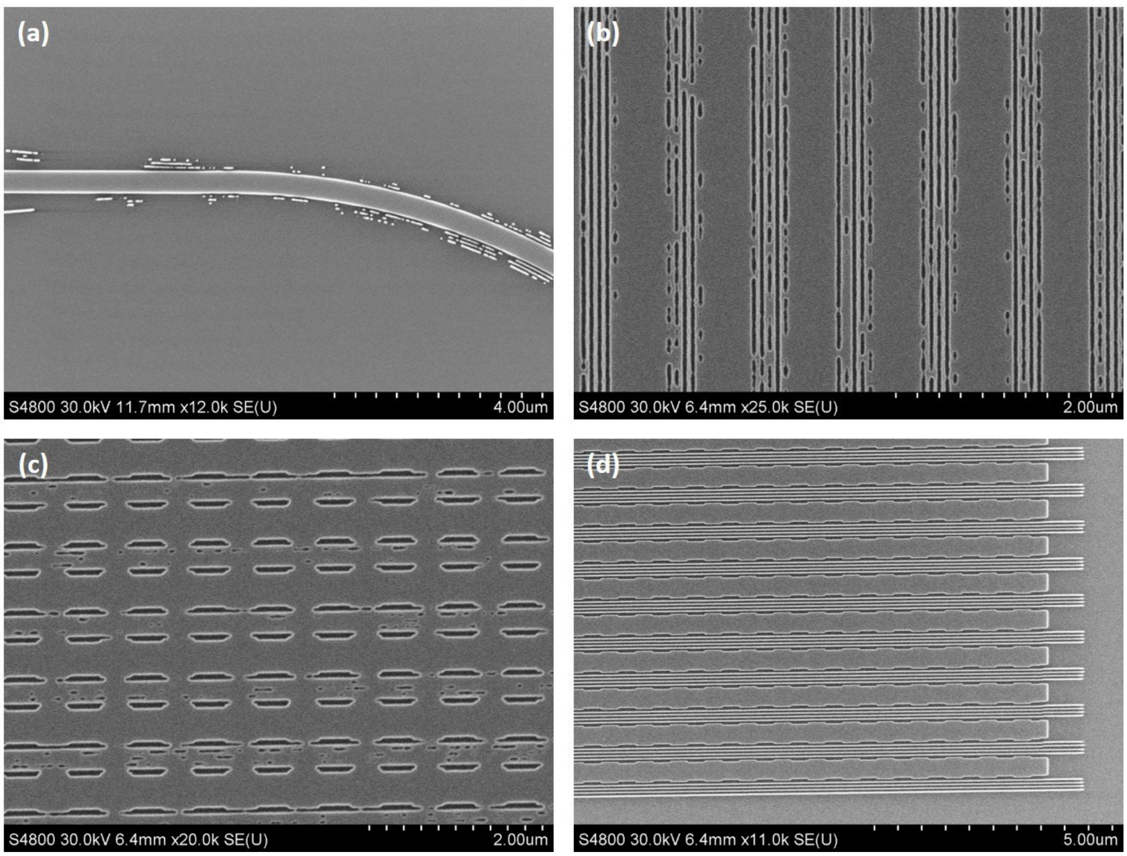

Figure 2.32. SEM images of e-skid waveguide arrays with e-beam lithography errors. Courtesy of Yun Jo Lee.

2.5.2 Experimental result

Yun Jo Lee fabricated a chip with test structures following the process flow in Fig 2.28 to evaluate the performance of the coupler design. The layout of the fabricated device is

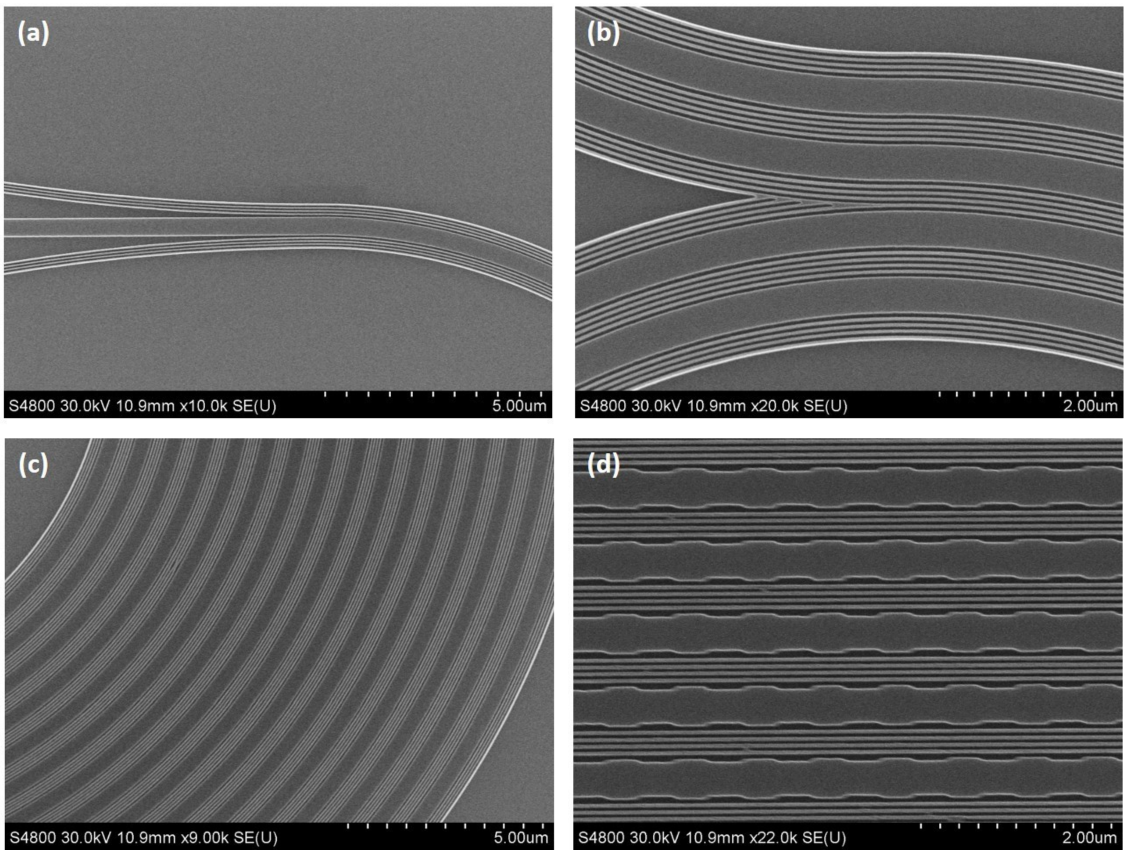

Figure 2.33. SEM images of e-skid array after proximity effect correction (PEC). Courtesy of Yun Jo Lee.

shown in Fig 2.34, where devices in Fig. 2.34a contains waveguides as a reference while Fig. 2.34b features a 1×8 MMI tree with SiN/Si coupler to show increased power capacity of the device compared to structures using pure Si.

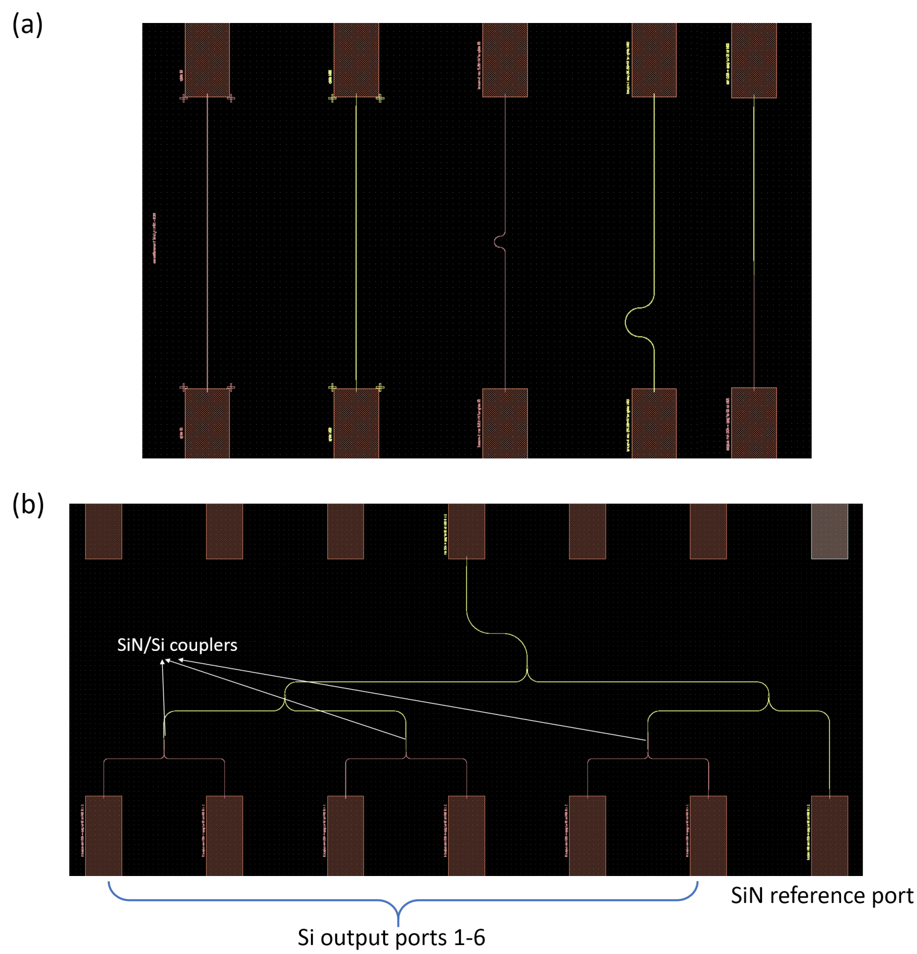

Figure 2.34. Layout of the test device (a) From left to right, Si straight waveguide; straight SiN waveguide; Si waveguide with 20 μm bending radius; SiN waveguide with 50 μm bending radius; SiN/Si coupler with 400 nm gap width. (b) A 1×8 MMI tree with SiN input and Si output. Yellow waveguides are silicon nitride, and pink ones are silicon. Orange rectangulars are U-grooves for edge coupling.

The result of the measurement is shown in Fig. 2.35. We can see from Fig. 2.35a that the output from SiN waveguides grows proportional to the input power while output from a Si waveguide grows linearly to $\sim$ 5 mW and then starts to drop with increasing input power. This is because the free carriers in Si absorb light and turn optical power into thermal energy. When the input optical power is high, the absorption heats the waveguide and produces more free carriers, leading to more absorption. This positive feedback loop causes the output power to drop with increasing input power and limits the power handling of Si waveguides. The coupling loss of the inverse taper edge coupler is measured by a test structure consists of two edge couplers connected by a short waveguide. The total loss of the device is measured to be 6 dB. The propagation loss for the straight waveguide in the test structure is negligible, thus a 3 dB fiber-to-chip edge coupling loss could be assumed. We can then estimate that the maximum power in Si waveguide without noticeable absorption is $\sim$ 10 mW. Similar observation shows that fabricated SiN/Si coupler has 0.5 dB higher insertion loss than straight waveguides and has a power handling capability of 5 mW.

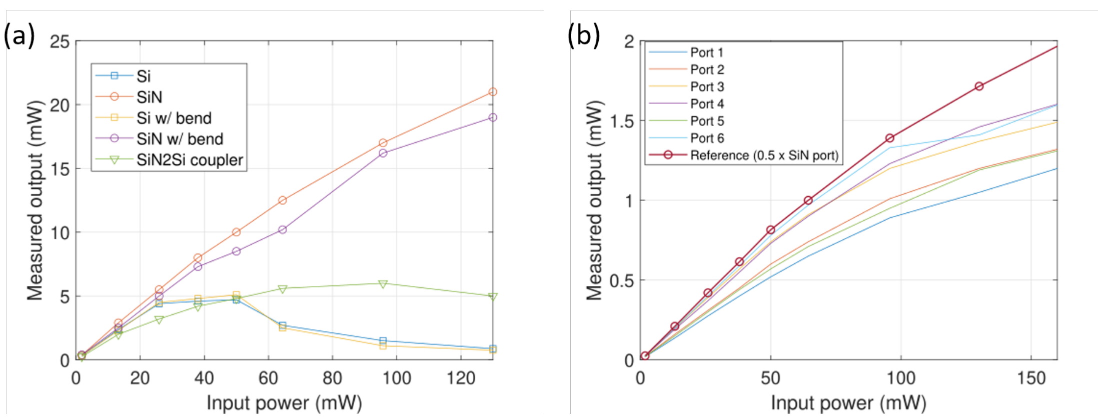

Figure 2.35. Testing result of devices in (a) testing structures in Fig. 2.34a; (b) ports of the 1 $\times$ 8 MMI tree in Fig. 2.34b. The output power from a Si structure is read after 1 minute cooldown time to allow possible two-photon absorption in Si waveguides.

Fig. 2.35b shows the output from a 1 $\times$ 8 MMI tree utilizing the SiN/SI coupler. The output power from 6 Si ports shows fair agreement with 1 dB power variation. Taking the same 3 dB coupling loss assumption as earlier, we estimate the power inside the device to be $\sim$ 24 mW, two times the maximum power of a silicon waveguide. One could easily imagine higher power capacity when more stages of the cascaded MMI coupler are implemented. Measurement results of the complete OPA device will be discussed in the next chapter.

3. HALF-WAVELENGTH PITCHED SILICON NITRIDE-SILICON OPTICAL PHASED ARRAY

For OPA designs in automobile applications, its primary performance focus usually falls into these two major categories: emission power, which relates to its ranging ability, and field-of-view. In [17], Poulton et al. demonstrated 400 mW continuous wave (CW) emission from a 9.1 W input. The reported device uses SiN as emitter material, which has lower propagation loss[35], low nonlinearity, and allows for higher guided power. Meanwhile, silicon-based OPA remains popular for its ability to achieve smaller emitter pitches and the ease of phase modulation. SiN/Si hybrid OPAs are being demonstrated recently to take advantage of both materials and aim to achieve high emission power and large steering angle at the same time[36]–[38].

3.1 Design

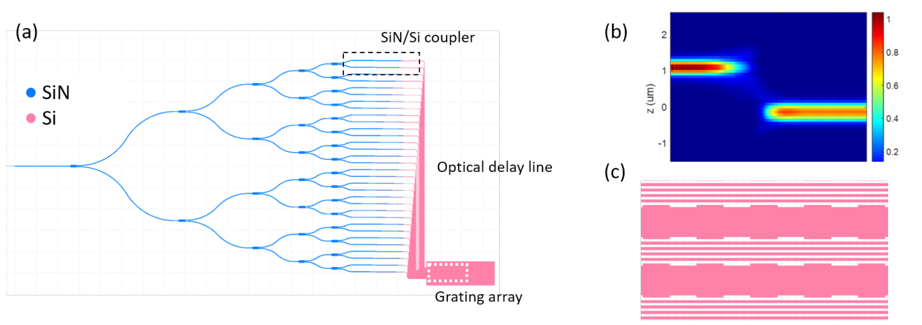

Figure 3.1. (a) Schematic of the 32 channel SiN/Si OPA. (b) Simulation of the power propagation in SiN/Si coupler (black boxed region in Fig. 1a) (c) Zoom-in view of a part of the e-skid grating emitter array(white boxed region in Fig. 1a)

The schematic of our proposed SiN/Si 32 channel hybrid OPA is shown in Fig. 3.1a, where we integrated a SiN layer on a 220 nm SOI platform. SiN waveguide with a reverse taper is used for input power coupling. After a cascaded multi-mode interferometer (MMI) splitter tree, the input light is divided into 32 channels. Fig. 3.1b shows the power propagation profile of the SiN/Si dual layer power coupler, with a designed insertion loss <0.1 dB. Fig.

3.1c shows the multi-layer fin-shaped e-skid cladding around the sidewall grating emitter array. The strong anisotropy of the multi-layer cladding strongly confines the TE-like mode by controlling the skin-depth of the evanescent wave for faster decay, thus limiting the evanescent coupling between emitters, which allows the emitter array to be placed at a half-wavelength pitch. In our design, this corresponds to 775 nm emitter spacing at 1550 nm working wavelength.

As a proof of concept, we introduced an L-shaped optical delay line to take the place of on-chip phase shifters[39], which adds the same amount of path length difference Δx between emitters. At any given wavelength λ, the phase difference between emitters are:

$$\Delta\phi = \frac{n_\lambda \Delta x}{\lambda} 2\pi \tag{3.1}$$

where n_λ is the effective index. Thus, changing the input wavelength tunes the phase profile of the emitters and effectively steers the beam without any active components on the chip. The silicon waveguide delay line is 24 μm between adjacent channels and is designed to provide 2π phase delay from wavelength tuning between 1520 - 1560 nm, thus achieving full-range beam steering from wavelength tuning. The grating emitters are 150 μm long with constant 30 nm perturbation on both sizes of the 450 nm wide silicon waveguide. Yun Jo Lee fabricates the designed device.

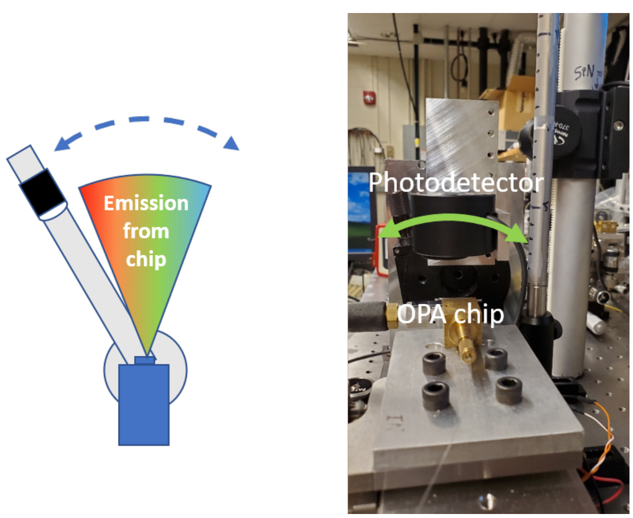

Figure 3.2. Experimental setup: illustration(left) and actual setup (right).

3.2 Measurement

The measurement setup is shown in Fig. 3.2. We used a free-space power detector instead of a high NA lens system to avoid the possible aberration during measurement over a large field of view. The detector is fixed to a rotational stage. The center of the stage is aligned to the center of the emitter array on the chip. The lateral emission pattern over $-65°$ to $90°$ off axis are recorded with a 1-degree interval by the power detector (access to $-90°$ to $-65°$ are limited due to constrains in the setup). The longitudinal angle (controlled by operating wavelength) and lateral angle (controlled by the phase difference between emitters) from the OPA emission are first measured and are shown in Fig. 3.3. The rotational stage sweeps through the emission pattern from two orthogonal directions and samples the longitudinal and lateral emission. As shown in the example of Fig. 3.3b-c, this particular emission has a lateral diverge full-width half-maximum (FWHM) angle of 9°and a longitudinal divergence angle of 2°.

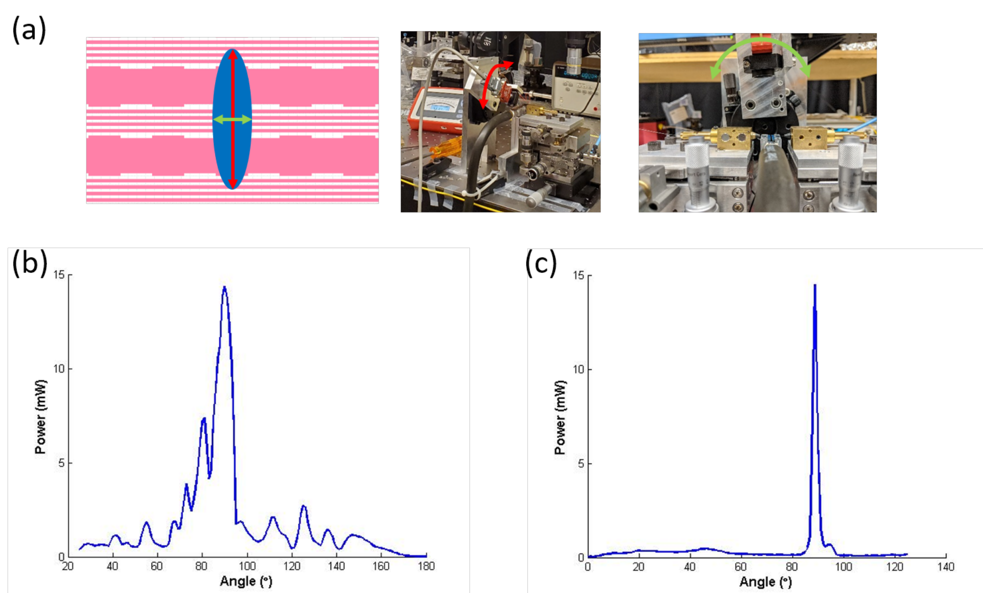

Figure 3.3. (a) Illustration and experimental setup for longitudinal and lateral angle measurement. (b) Example lateral emission. (c) Example longitudinal emission

Because the input wavelength controls both lateral (fast) and longitudinal (slow) steering for our OPA device, for each measurement, we first fix the input wavelength, then align the longitudinal angle of the emission to the detector. Finally, the detector is rotated laterally to the emitter array and captures the emission pattern. As a proof of concept, we tested a 16-channel OPA with 775 nm spacing e-skid grating emitter array and 14 μm difference L-shaped optical delay line. The phase delay $\Delta\phi$ introduced by tuning the wavelength is given by:

$$\Delta\phi = \Delta\left[\frac{Ln_{\text{eff}}}{\lambda}\right]2\pi \tag{3.2}$$

where n_{eff} is the effective index of the waveguide. And $L = 13230$ nm is the normalized path length difference in the device. The expected phase shift and corresponding beam location are illustrated in Fig. 3.4

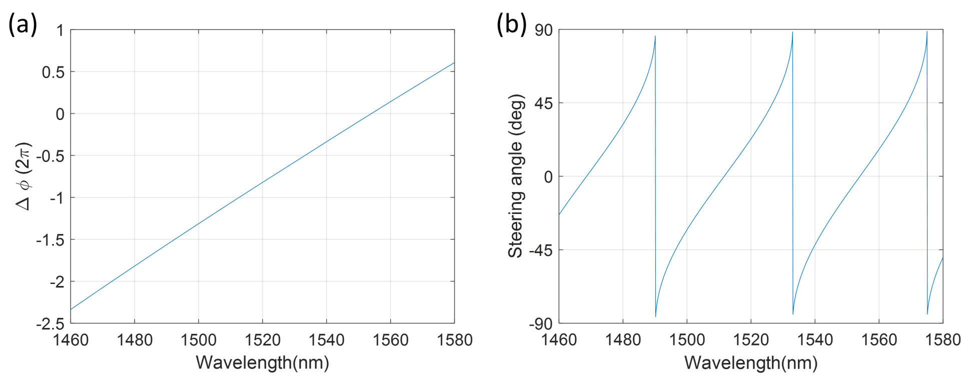

Figure 3.4. (a) Calculated phase difference from wavelength tuning (normalized to 2π) (b) Converted beam location from the phase shift obtained in (a).

The measurement result from the 16-channel device is shown in Fig. 3.5. Fig. 3.5b shows the high level of agreement between measured beam positions and expected beam positions from simulation of the optical delay line in Fig. 3.4. The measured emission has an FWHM of $\sim 6°$, which matches the calculation from the emitter array size.

The power of the measured beam in Fig. 3.5 varies with different input wavelengths and steering angles. This is determined by the constructive/destructive interference between the upward emission and the back-reflection from the silicon substrate, as illustrated in Fig. 3.6a. FDTD simulation is performed to quantify the effect of back-reflection on the emission

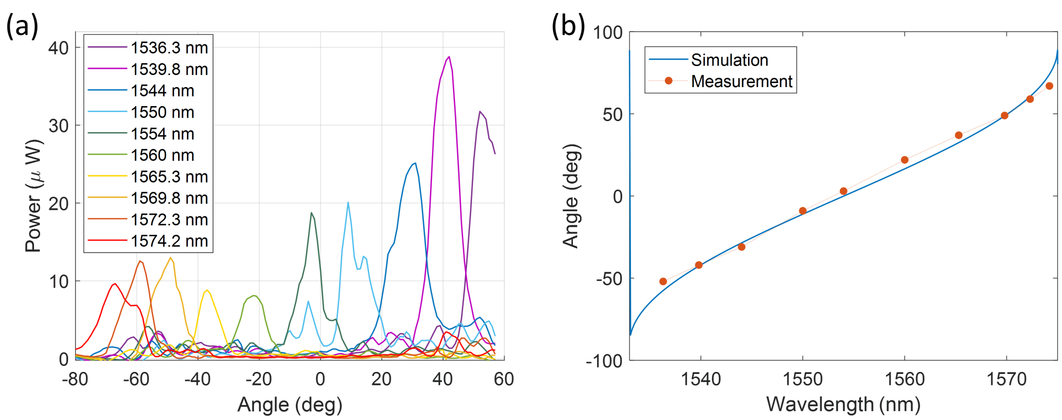

Figure 3.5. (a) Measured beams with different wavelength input, showing an aliasing-free FOV of 120°. (b) Measured steering angle compared with simulation result from the optical delay line.

pattern. The result is shown in Fig. 3.6b, which matches closely to the measurement result of Fig. 3.5a.

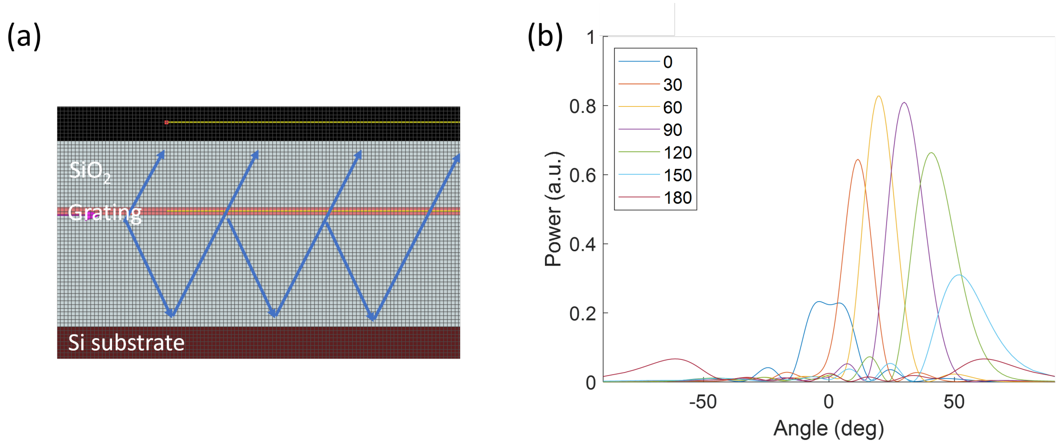

Figure 3.6. (a) Illustration of the interference between back-reflection and emission (b) Simulated emission profile considering the effect of back-reflection.

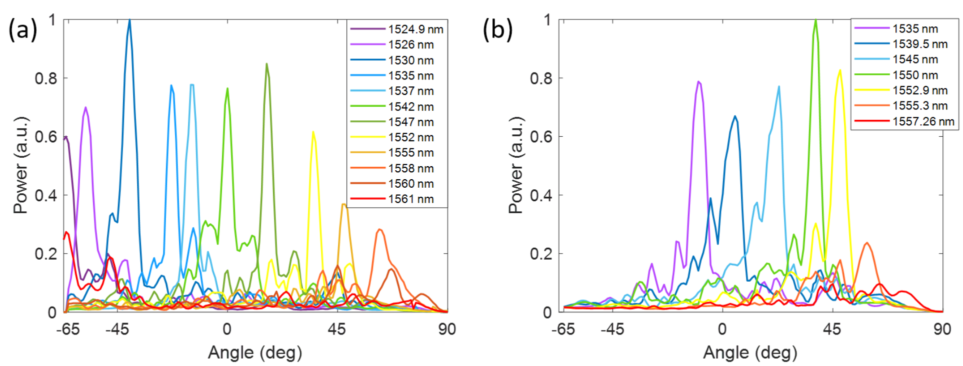

Figure 3.7. (a) Measurement result from 32 channel Si OPA; (b) Measurement result from 32 channel SiN/Si OPA.

We repeat the same set of experiments on 32-channel OPA devices. The measured lateral beam-steering at different wavelengths are shown in Fig. 3.7. Two different types of device are measured in this experiment: a 32 channel silicon-based OPA with 775 nm emitter spacing is measured to demonstrate the large FOV beam-steering using wavelength tuning, which shows 135° aliasing-free steering as in Fig. 3.7a; and a 32 channel SiN/Si hybrid OPA with 775 nm emitter spacing is also measured with an aliasing-free FOV of 70° (Fig. 3.7b). The smaller FOV is limited by the insufficient wavelength tuning from the erbium-doped fiber amplifier(EDFA) in the setup. The two types of devices share the same type of silicon e-skid grating emitter design.

3.3 Beam de-convolution

3.3.1 De-convolution

A low-power free-space detector is used in the measurement with 2 mm effective area size. We take into account the effect of the detector size to the measured beam width: when the detector is placed at a fixed distance from the chip, the measured data is the convolution between the actual emission profile and a gate function formed by the detector over the measurement FOV. In order to de-convolute the detector function from the measurement, we model the process as follows: the measured power profile $\boldsymbol{y}$ is the convolution between the original emission $\boldsymbol{x}$ and the detector function $\boldsymbol{A}$,

$$\boldsymbol{A}\boldsymbol{x} = \boldsymbol{y} \tag{3.3}$$

where the detector coefficient matrix A is:

$$\boldsymbol{A} = \begin{bmatrix} 1 & ... & 1 & 0 & 0 & ... & 0 \\ 0 & 1 & ... & 1 & 0 & ... & 0 \\ ... & & & & & & ... \\ 0 & ... & 0 & 0 & 1 & ... & 1 \end{bmatrix} \tag{3.4}$$

Here the number of rows N_R corresponds to the measurement field-of-view. And within each row, the length of the series of ones is N_D, which represents the size of the power detector. The number of columns is then $(N_R + N_D - 1)$. From this definition, the de-convolution process to solve for x can be approximated by finding the least-squares solution for $\boldsymbol{A}\boldsymbol{x} = \boldsymbol{y}$:

$$\min \|\boldsymbol{y} - \boldsymbol{A}\boldsymbol{x}\|_2^2 \tag{3.5}$$

The solution is:

$$\boldsymbol{x}^* = (\boldsymbol{A}^T\boldsymbol{A})^{-1}\boldsymbol{A}^T y \tag{3.6}$$

For example, a near-perpendicular emission pattern (32 channel SiN/Si device, 1545 nm input, shown in Fig. 3.3b and Fig. 3.7b) is chosen for the process. And the resulting de-convolved profile is shown in Fig. 3.8a. We can see that there is a strong oscillating zig-zag pattern across the beam profile. With some negative power values, this is not a good representation of the emitted beam. The reason for this is that the above de-convolution process does not consider the possible errors caused by inaccurate detector positioning or power fluctuation in measurement. Furthermore, during the de-convolution, those errors are accumulated along the solution $\boldsymbol{x}$, causing the oscillating pattern. To minimize the effect of the error in the experiment, we can add a $L2$ regularization term $\boldsymbol{Bx}$, where:

$$\boldsymbol{B} = \begin{bmatrix} 1 & -1 & 0 & 0 & ... & 0 \\ 0 & 1 & -1 & 0 & ... & 0 \\ ... & & & & & ... \\ 0 & ... & 0 & 0 & 1 & -1 \end{bmatrix} \tag{3.7}$$

The number of rows N_R still corresponds to the measurement field-of-view. The $(1, -1)$ term helps to constrain the difference between adjacent values in solved $\boldsymbol{x}$, thus prevents any negative values in $\boldsymbol{x}$. And the objective function with regularization becomes:

$$\min \|\boldsymbol{y} - \boldsymbol{Ax}\|_2^2 + \alpha\|\boldsymbol{Bx}\|_2^2 \tag{3.8}$$

where α is the regularization parameter. The solution is then:

$$\boldsymbol{x}^* = (\boldsymbol{A}^T\boldsymbol{A} + \alpha\boldsymbol{B}^T\boldsymbol{B})^{-1}\boldsymbol{A}^T y \tag{3.9}$$

The de-convolved profile with regularizer is shown in Fig. 3.8b, which is free from the zig-zag artifact. During the de-convolution, we set the number of rows N_R to 10 times the measurement FOV in degrees, which effectively interpolates the retrieved beam profile by 10X to get a 0.1°resolution. The exact process is applied to all measured data in Fig. 3.7. And the resulting data are shown in Fig. 3.9a-b and provide more details on the beam width and main lobe power. Note that emission profiles that were cut-off by the measurement FOV are omitted in the de-convolution process (e.g., the 1524.9 nm line in Fig. 3.7a).

The beam width from an OPA emission is expected to be[9]:

$$\Delta\theta_{3\mathrm{dB}} = \frac{c_1}{\cos\theta}\frac{\lambda}{Nd} \tag{3.10}$$

where $\Delta\theta_{3\mathrm{dB}}$ is the FWHM of the emitted beam, θ is the beam steering angle, N is the number of emitters, and d is the spacing between emitters. c_1 is a constant related to the emitter power profile. Here $c_1 = 0.886$ for a rectangular emission window. We normalize the beam width at different emission angles by factoring out the term $1/\cos\theta$. The narrowest normalized beam width is 3.56° for Si OPA (1526 nm input) and 3.89° for SiN/Si OPA (1550 nm input). The phase error between emitters from the lack of individual phase shifters mainly contributes to the FWHM difference compared to the expected value of 3.17°, obtained from the emitter array size 775 nm × 32.

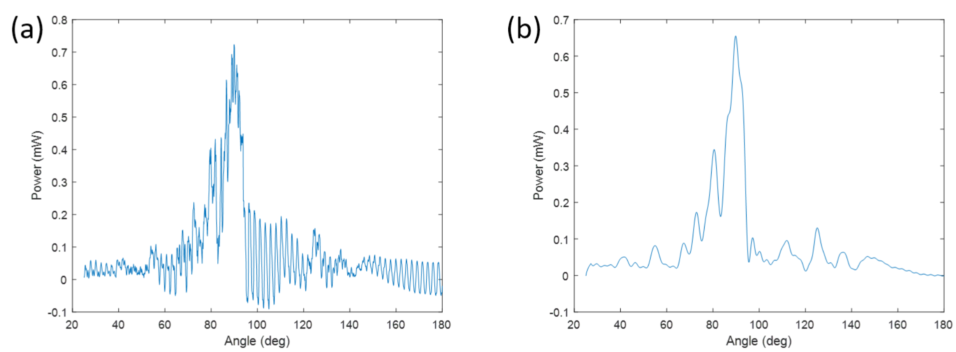

Figure 3.8. De-convolved beam profile (a)without regularization. (b) with regularization term $\boldsymbol{Bx}$

3.3.2 Emitted power

Further measurements are performed to verify the correctness of the de-convolution process. As shown in Fig. 3.10, a high-power detector is used to measure the emitted power from the OPA from different heights. The emission profile is sampled by the 5 mm effective aperture size of the detector. We used the same emission profile in Fig. 3.8 (32 channel SiN/Si device, 1545 nm input) for easier alignment during the experiment, as the emission profile has a near-perpendicular main lobe. The measured power with 1 W/1.6 W input

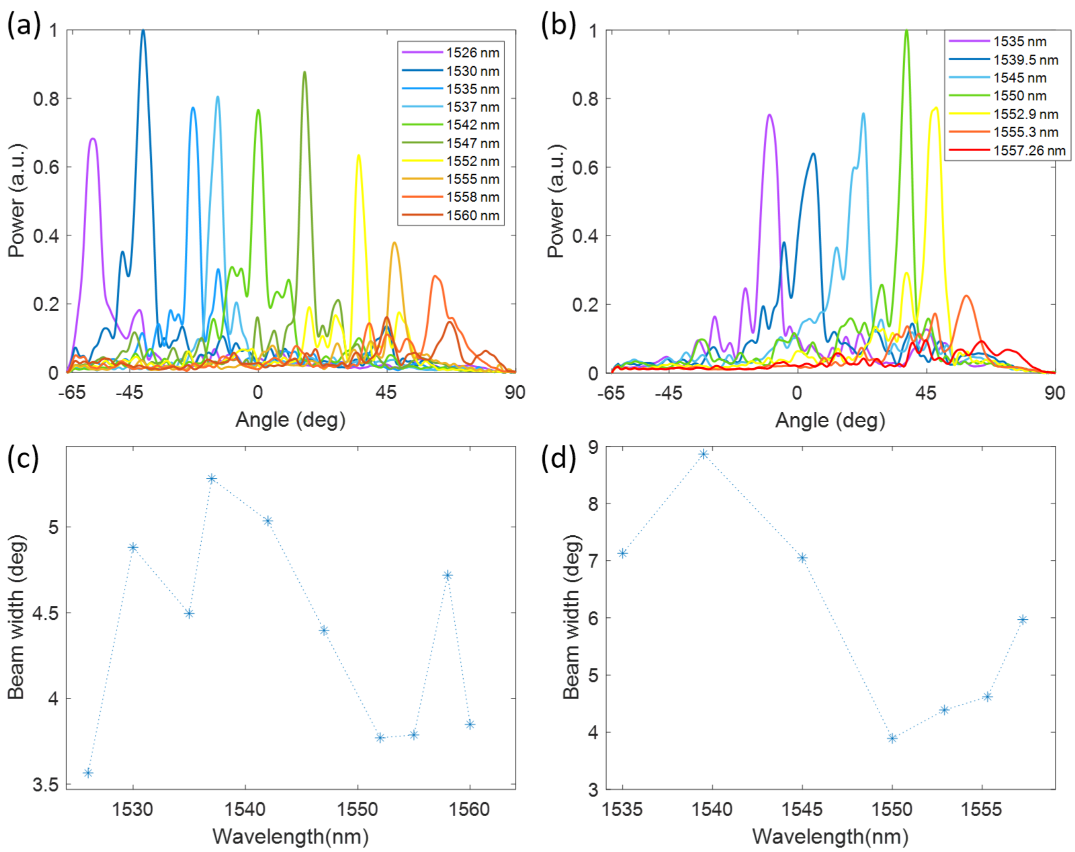

Figure 3.9. (a) De-convoluted beam profile of 32 channel Si OPA; (b) De-convoluted beam profile of 32 channel SiN/Si OPA; (c) Normalized beam FWHM of 32 channel Si OPA; (d) Normalized beam FWHM of 32 channel SiN/Si OPA.

power is shown in Fig. 3.11, with detector range from the OPA chip being ~ 0.5 cm to 20 cm.

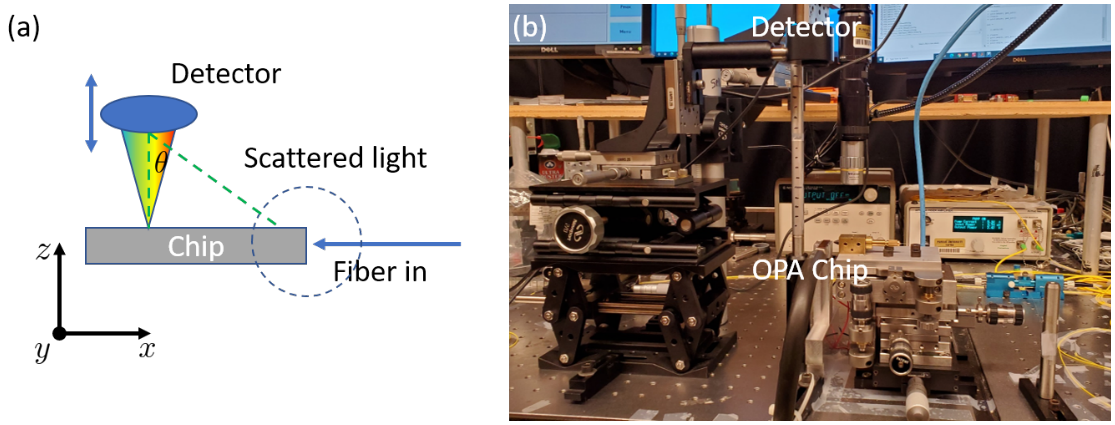

Figure 3.10. Illustration (a) and actual setup (b) of the verification measurement.

The reading from the power detector consists of two parts during the measurement: the emission from the OPA and the scattering from the chip facet. The scattered power captured by the detector can be modeled as the following: Assuming the coupling facet (interface between the lensed fiber and edge coupler on chip) is at the origin, the scattered light is uniformly distributed in space:

$$f(x, y, z) = \frac{C}{4\pi(x^2 + y^2 + z^2)} \tag{3.11}$$

where C is the total scattered power. Assuming 3dB coupling loss from fiber to chip, C is 50% of the input power. The amount of scattering captured by the detector is:

$$P = \iint_D f \cos\theta dxdy = \iint_D \frac{C \cos\theta}{4\pi(x^2 + y^2 + z^2)} dxdy \tag{3.12}$$

where D is the detector area. $\cos\theta$ is the angle formed by the vertical direction and the connection between the coupling point and the center of the detector. In the actual experiment, we adjust the detector so that the effective detector area is parallel to the chip surface and aligned to the emission aperture of the chip on x and y axes.

The calculated scattered power with respect to the detector distance is shown in Fig. 3.12. As the power scales inverse proportionally with the square of the distance, the amount

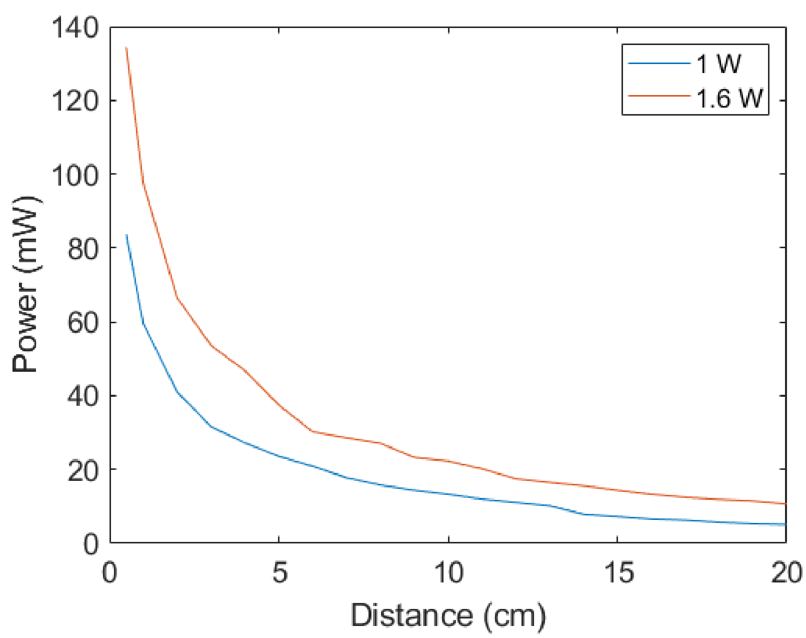

Figure 3.11. Measured power from 32 channel OPA with 1 W/1.6 W input power.

of scatted light captured by the originally measured emission (Fig. 3.3b) should be negligible. By integrating the de-convoluted beam profile (Fig. 3.8b) over different field-of-view (representing different measurement distance in Fig. 3.11) and adding the calculated scattering, the calculated results from de-convolution are shown in Fig. 3.13. The calculated power matches well with the measurement, thus showing good precision of the de-convolution process.

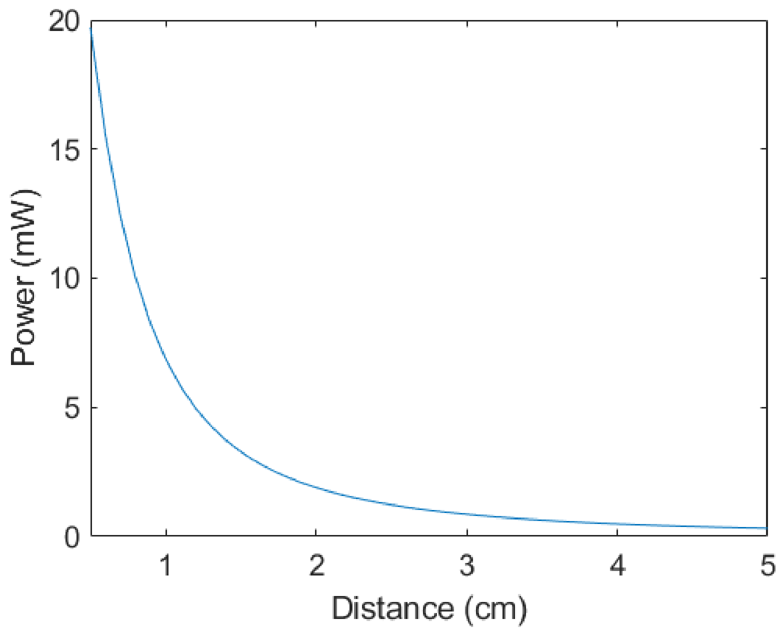

Figure 3.12. Calculated scattered power captured by the detector.

To measure the maximum emission power from the device, we chose 1550 nm input for a 32 channel SiN/Si OPA. The emission profile has relatively lower phase noise than other wavelengths, as depicted in Fig. 3.8b. Three different power levels were sent into the 32 channel SiN/Si OPA after EDFA: 0.5 W, 1 W, and 1.6 W. Both the measured and de-convolved data are shown in Fig. 3.14(a-b). The total beam power is obtained by integrating the de-convoluted power over the beam width. The result is shown in Fig. 3.14c, which gives a maximum emission power of 44.38 mW at 1.6 W input and shows a strong linear relationship between input and output power profiles. To the best of our knowledge, this is the highest amount of CW power measured from a Si OPA emitter array. It should also be noted that strong vibration of the input fiber occurs at a high input power level. The effect of the vibration on the chip coupling affects the maximum amount of power that could be sent into the chip, along with the capability of the available EDFAs. With negligible nonlinearity observed during the measurement, it is expected that higher emission power could be achieved from this design. The total emission efficiency into free-space is 10% (160 mW out of 1.6 W input), obtained by integrating over full measurement FOV. The power efficiency of the main beam is $\sim 3\%$. Without any fine phase-aligning mechanisms, the emission efficiency is already comparable to what's reported in [17].

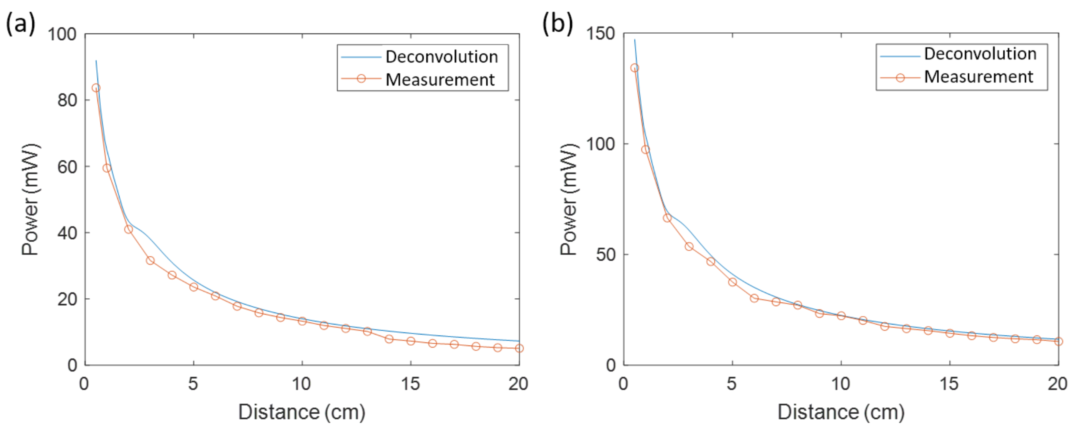

Figure 3.13. Expected power level from de-convolution compared to measurement results at (a) 1W; (b) 1.6 W input power.

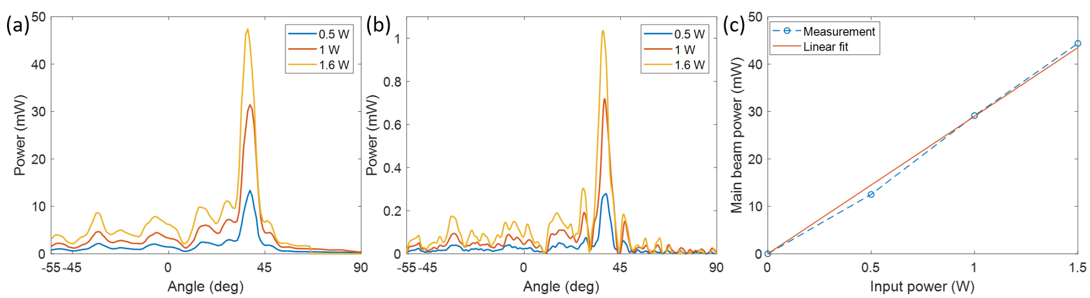

Figure 3.14. (a) High power emission measurement from 32 channel SiN/Si OPA; (b) Deconvolved result of (a); (c) Emitted main beam power with respect to input power

3.4 Phase noise retrieval

To better understand the effect of phase error on our device, Finite Difference Time Domain (FDTD) simulations were performed using commercial software Lumerical FDTD solution™. In the simulation, the input amplitude and phase of 32 emitters are optimized to reconstruct the example de-convolved emission profile in Fig. 3.14b using particle swarm optimization (PSO)[40]. The figure of merit is defined as the residual sum of squares (RSS) between simulated far field emission and de-convolved emission profile. And the best-matching reconstructed profile is shown in Fig. 3.15a along with its measured pairing profile after 100 iterations. The power in the main beam is expected to be ~ 2.5X of the measured power if the obtained phase error is suppressed, as shown by simulation results in Fig. 3.15b. Thus, the phase error obtained through simulation is mainly caused by the system's lack of individual phase control. Fig. 3.15c illustrates the impact of half-wavelength pitched OPA on main beam power efficiency. For the emission angle ($\sim 37°$ off-axis) illustrated in Fig. 3.15, further simulation shows that if the emitter spacing extends from $\lambda/2$ to λ while keeping the same phase/power error, the power efficiency of the main beam rapidly drops to $\sim 50\%$ of the original beam as a result of emerging grating lobes. It is worth noting that the non-monotonicity of Fig. 3.15c results from the phase/power noise applied in the simulation.

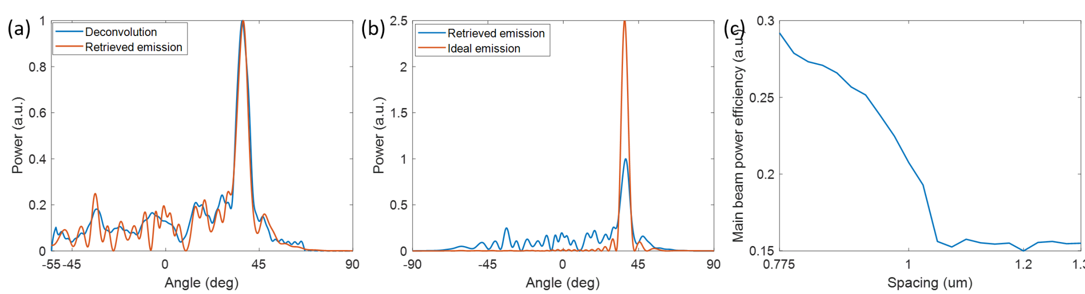

Figure 3.15. (a) Comparison between measured and simulation retrieved emission profile; (b) Comparison between retrieved ideal emission profile; (c) Main beam power efficiency with respect to OPA emitter spacing

Table 3.1. Summary of related OPA work

Year	Emitter spacing/ # of emitter	Steering range (°)	Beam size (°)	Ref., notes
2016	Non-uniform, ~1 mm	51	3.3	[41]
2017	4μm×1024	-	0.02	[17], 400 mW emission from SiN array
2018	775 nm× 64	>160	1.6	[2], 1D end-fire array
2019	1.65 μm×512	56 × 15	0.04	[4]
2019	1.3 μm×24	>40	-	[42]
2019	0.8 μm×16	64	6.7	[43], 1D end-fire array
2020	775 nm×16	120	6	[44], earlier work from the author
2021	775 nm×32	135	3.6	This work

3.5 Summary

In this chapter, we demonstrated an aliasing-free optical phased array with half-wavelength emitter pitch and high emission power. SiN/Si hybrid platform is used to direct high power onto the device while maintaining a low emitter pitch. E-skid waveguide is used to minimize the input spacing to half wavelength. A record-high FOV of 135°is measured along with high emission power (44 mW), making the design promising for long-range LiDAR systems.

In Table 3.1, we have summarized the design parameters and results from several high-performance OPAs for comparison.

4. TWO-DIMENSIONAL OPTICAL PHASED ARRAY

4.1 Introduction

Currently, there are two major concerns regarding the application of OPA LiDAR systems: power efficiency, which limits the detection range of a LiDAR, and two-dimensional beam steering range. Most studies on OPA now focus on an array of waveguide grating antennas for a 2D converged beam emission. However, grating emitters often suffer from low efficiency caused by downward emission towards the substrate. Efforts have been made to address this problem by introducing reflectors[45], [46] or asymmetric grating design[29]. Still, its loss is much higher than in-plane devices. Also, 2D beam steering for a grating antenna array is often realized through wavelength tuning in addition to the phase control. Due to the limitation in tunable laser sources, wavelength tuning has a slower speed and a narrower field of view than those based on thermal or electro-optics phase shifters, limiting the steering performance on the second dimension. On the other hand, 1D end-fire $\lambda/2$ spaced array, as demonstrated in[2], [47], could account for higher power efficiency for its in-plane design, along with large field-of-view. However, such a 1D array could only provide beam convergence in one dimension and require additional mechanisms for two-dimensional beam focusing and steering. The idea of a multi-layer OPA with a 2D edge emitter array has been discussed[48], [49], with limited performance from large emitter pitch and small scale.

In this section, we propose the design of a scalable multi-layer OPA for 2D solid-state beam steering operating at a single wavelength. This design consists of a 2D edge emitter array with a uniform half-wavelength pitch both horizontally and vertically; thus an aliasing-free $180° \times 180°$ field of view could be achieved with high emission efficiency. Furthermore, the evanescent coupling between the densely packed emitters is suppressed by the use of index-mismatched waveguides[2], [50] and e-skid waveguides[13].

4.2 Structure design

Fig. 4.1a is an illustration of the multi-layer OPA design. The power in the input waveguide (shown as the green part in Fig. 4.1a) is first split into M branches through a cascaded 1×2 MMI tree (# of stages $= \log_2 M$), then each branch is directed to its designated layer (gray ones) through a series of evanescent couplers (similar to Fig. 3.1b), designed to have <0.1 dB insertion loss. Within each layer, we further split the input using another MMI splitter tree (blue) and control the phase of the resulting output waveguides with individual thermal phase shifters (not shown). After phase shifting, the waveguides are routed to the chip's end and packed densely for edge emission (orange).

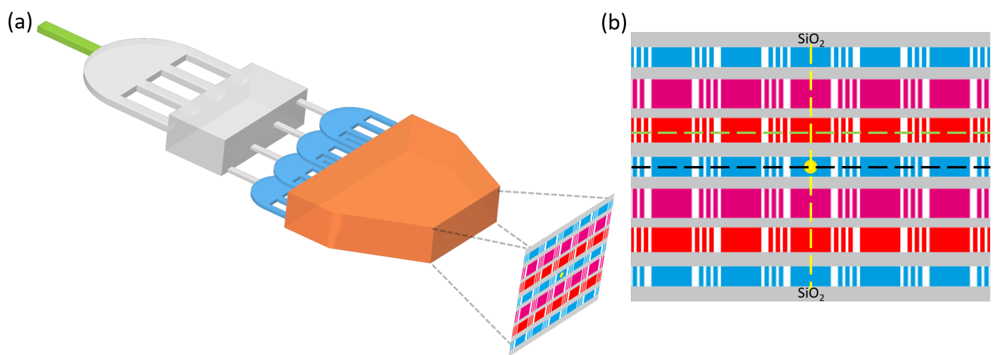

Figure 4.1. (a) Illustration of the multi-layer OPA structure. (b) Cross-sectional view of the waveguide array. Different colors indicate the different thicknesses of the Si waveguides. The yellow spot indicates the position of the power input for the crosstalk simulation in section 3.

The unambiguous field-of-view θ_{FOV} of an OPA is given by:

$$\theta_{\text{FOV}} = 2\sin^{-1}\left(\frac{\lambda}{2d}\right) \tag{4.1}$$

where λ is the operating wavelength and d is the emitter array pitch. Here we propose the design for a dense 2D emitter array by controlling evanescent crosstalk through both propagation constant mismatch and the use of e-skid waveguides. The designed waveguide array has a pitch of 775 nm in both dimensions with low crosstalk, which enables a full $180° \times 180°$ aliasing-free field-of-view at an operating wavelength of 1550 nm. An illustration of the closely-packed array is shown in Fig. 4.1b.

The waveguides between different layers are phase-mismatched by cycling through three different waveguide thicknesses so that waveguides of the same height are separated by 1.5 λ vertically. Power coupling within the same layer is controlled by utilizing asymmetric e-skid waveguides of the same core width. As shown in Fig. 4.2b, the strong anisotropy of the multi-layer cladding strongly confines the TE-like mode by controlling the skin-depth of the evanescent wave for faster decay, thus enhancing the coupling length L_0. At the same time, the asymmetric placement of multi-layer cladding between waveguides (shown in Fig. 4.2a, type A waveguide features a narrower first air gap compared to its type B neighbor) creates the index mismatch needed for limiting maximum coupling between adjacent waveguides. Layers of different thicknesses are stacked in an alternating fashion: the waveguide above type A (with narrower first air gap) is type B (with wider first air gap), and vice versa (Fig. 4.1b). This pattern in the layer stacking further helps control the vertical crosstalk between layers. The maximum power coupled between waveguides ($\mathcal{T}$) with phase mismatch, derived from coupled mode theory (CMT), is limited by[12]

$$\mathcal{T} = \frac{\pi^2}{4}\mathrm{sinc}^2\left[\frac{1}{2}\sqrt{(\frac{\Delta\beta L_0}{\pi})^2 + 1}\right] \tag{4.2}$$

where $\Delta\beta$ is the phase mismatch and L_0 is the coupling length. It could be derived from the above equation that the product $\Delta\beta L_0$ determines the maximum coupling. In our design, the use of e-skid waveguides greatly enhances L_0. And $\Delta\beta$ is provided by the asymmetric cladding placement for lower crosstalk.

4.3 Result and Discussion

Finite Difference Time Domain (FDTD) simulations were performed using commercial software Lumerical FDTD Solution$^{\mathrm{TM}}$ to characterize the system performance. Optimization of the e-skid waveguide design is performed through a 3D FDTD simulation where the maximum coupled power $\mathcal{T}$ is parameter swept with respect to Si fin width ($\mathrm{w_{Si}}$) and air gap width ($\mathrm{w_{air}}$). The simulation model is a 5×1 single-layer waveguide array as shown in Fig. 4.2a. All waveguides have a width of 450 nm to ensure single TE (transverse electric) mode operation with low propagation loss at the center wavelength of 1550 nm. The waveguide array has a center-to-center pitch of 775 nm. The minimum feature size in the design is set to 30 nm to reflect limitations in fabrication. The smaller first air gap ($\mathrm{Gap_A}$ in Fig. 4.2a) is also set to 30 nm to provide the maximum asymmetry for phase mismatching between

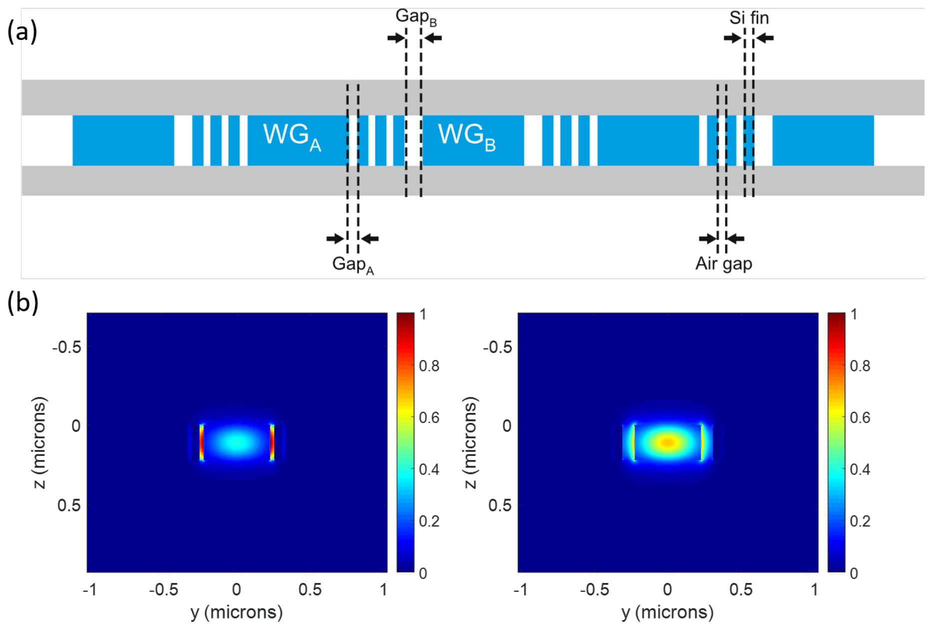

Figure 4.2. (a) Detailed schematic of the e-skid waveguide array in a single layer(black line in Fig. 4.1b). (b) Example of electric field profile of the fundamental mode in type A waveguide (left) and B (right), assuming $\mathrm{Gap}_\mathrm{A} < \mathrm{Gap}_\mathrm{B}$.

neighbors. The simulation result is shown in Fig. 4.3 where maximum coupling ($10\log(\mathcal{T})$, in dB) is plotted against Si fin width and air gap width for both 3- and 4-layer cladding. The red region on the bottom right of each subplot indicates parameters that did not meet the 30 nm feature size criterion. A cladding layer number of 3 and $\mathrm{w_{Si}} = 50$ nm and $\mathrm{w_{air}} = 30$ nm are chosen with a peak crosstalk of -23.47 dB, indicated by the green arrow in Fig. 4.3. The chosen parameters also provide a smooth neighborhood that will help overcome potential fabrication variations.

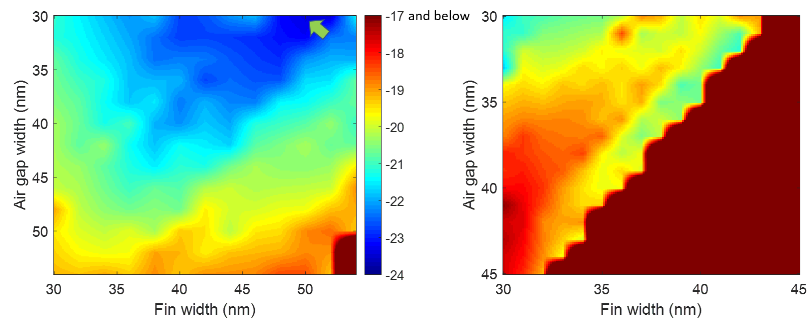

Figure 4.3. Maximum crosstalk (in dB) in the same layer vs. Si fin width and air gap width in e-skid multi-layer cladding. Left: result for 3-layer cladding; Right: result for 4-layer cladding. The green arrow indicates the set of parameter used in following discussions.

To verify the performance in the multi-layer design, 3D FDTD simulation is run on a simulation model with 5 (horizontal)×7 (vertical) waveguide array as shown in Fig. 4.1b, which includes a basic repeat unit in all directions around the input waveguide. Different colors in Fig. 4.1b are used to indicate three different waveguide thicknesses: blue (220 nm), red (270 nm), and magenta (350 nm). The center-to-center pitch of the array is 775 nm both horizontally and vertically. The length of the waveguide array is 300 μm. A TE mode was sent into the center waveguide (type B waveguide with 450 nm×220 nm core, indicated by the yellow dot in Fig. 4.1b) in the FDTD simulation. This waveguide has presumably the weakest light confinement, thus would reveal the strongest crosstalk in the system. The areas of interest are the same horizontal layer (yellow line in Fig. 4.1b), the vertical plane (black line in Fig. 4.1b), and the adjacent horizontal layer (green line in Fig. 4.1b), respectively.

The result is shown in Fig. 4.4. The strongest coupling between neighboring waveguides is less than -23 dB in the same layer and less than -25 dB vertically.

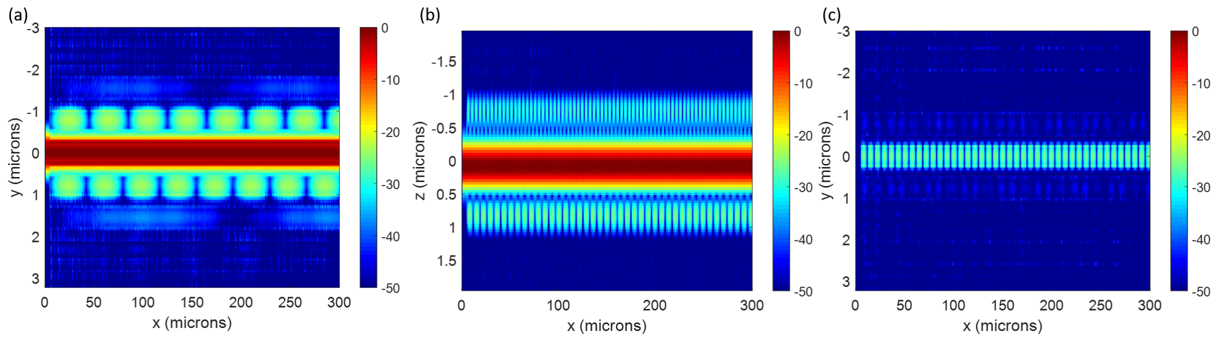

Figure 4.4. Simulation of power propagation in the waveguide array with propagation constant mismatch (in dB). (a) Power profile in the horizontal plane (black line in Fig. 4.1b). (b) Power profile in the vertical plane (yellow line in Fig. 4.1b). (c) Power profile in adjacent horizontal plane (green line in Fig. 4.1b).

The final waveguide routing towards the emission plane is arguably the most critical section of the design. As shown in Fig. 4.5a, the final stage of routing could be realized by adding an MMI splitter tree for each layer and phase shifters for individual waveguides. Waveguides from different layers are then brought together through an interleaved fashion: e.g., odd-numbered layers are placed on the left of Fig. 4.5a and even-numbered ones on the right. Later, when those layers are combined, the waveguides that run parallel on top of each other are separated by λ, thus minimizing the crosstalk in between. The drawback of this approach is that it introduces more interlayer waveguide crossings in the place of adjacent parallel waveguides. Illustrated in Fig. 4.5b, left-most waveguide in even-numbered layers and right-most waveguides needs to cross waveguides in adjacent layers $2(n-1)$ times before arriving at the emission plane. Finally, FDTD simulations are run for the structure in Fig. 4.5b for verification of potential scattering during the process. We simulated the propagation of a 2-layer, 8 waveguide crossing section with silicon thickness 220 nm and 270 nm, as those two layers have weaker confinement compared to the 350 nm layer.

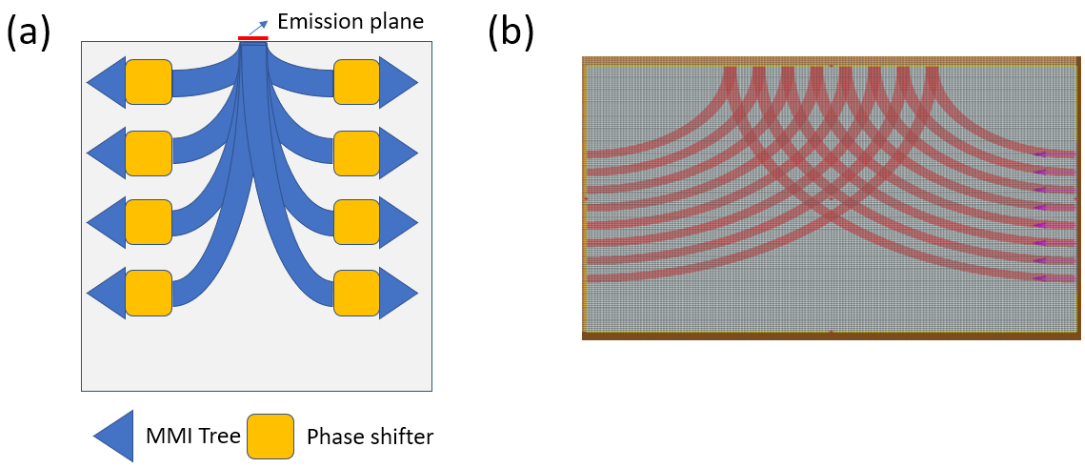

Figure 4.5. (a) Diagram of the combining region of the 2D emitter array; (b) Illustration of waveguide crossing.

The simulation result of the waveguide crossing is shown in Fig. 4.6. The difference between the resulting optical mode at the emission is negligible, showing that the waveguide crossing has little effect on the final emission profile.

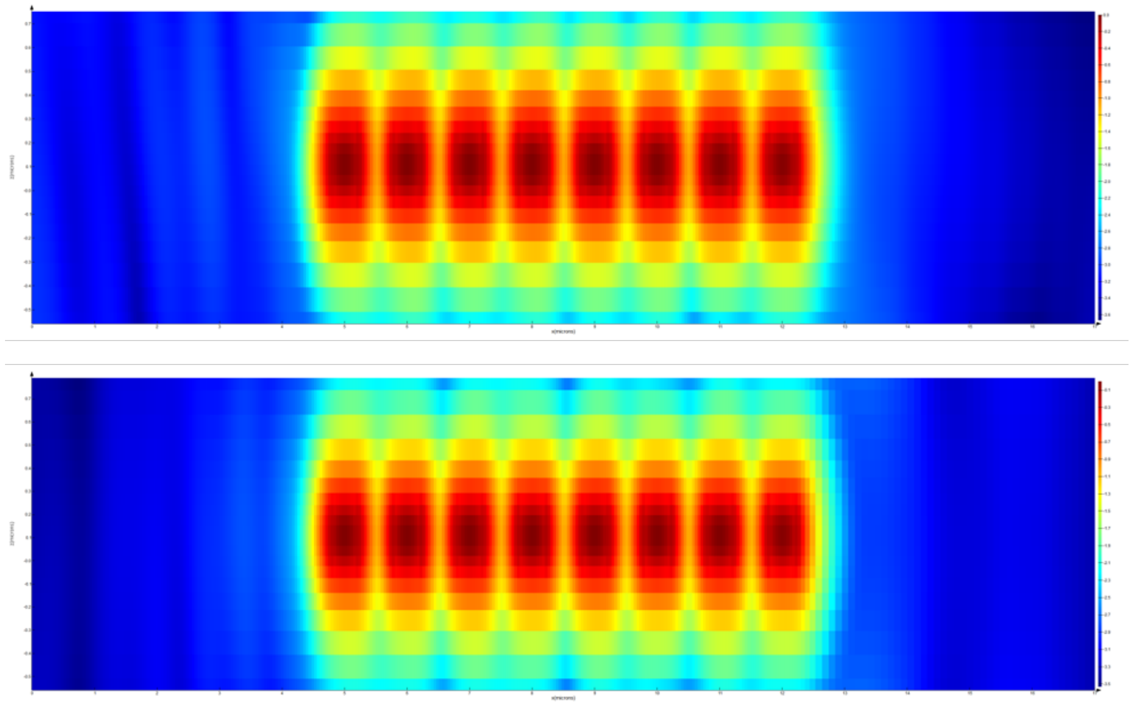

Figure 4.6. Simulated waveguide output without (top) and with (bottom) waveguide crossings.

Fig. 4.7 shows the effect of potential horizontal misalignment between layers during fabrication, which is modeled by a 5×3 waveguide array with offset introduced in the center layer to the other layers. The amount of misalignment is normalized to the array pitch size (775 nm). The peak crosstalk first drops due to the increase of spacing between vertical waveguides when increasing the misalignment. Then it increases as the alternating pattern of the array is broken. With maximum misalignment (i.e., the type A waveguides now stack directly on top of each other), the design observes the strongest crosstalk but still less than -22 dB, proving that the array design is immune to horizontal misalignment between layers. This is important as it could allow such OPAs to be fabricated using techniques that could efficiently stack up layers, such as the bonding of pre-patterned membranes, but not so good in achieving accurate alignment between the layers.

Another serious issue that the field of silicon photonics has always faced is the waveguide coherence in mass productions, which would limit the performance of large-scale OPAs. In addition, random fluctuations in structures could occur in long waveguides, introducing phase and power error into the system and affecting the output beam quality. The effect of such noise in our design has been modeled and simulated as follows: The E-field from a single edge emitter with phase and power noise could be expressed as:

$$E_{\mathrm{i}}(t) = (A_{\mathrm{i}} + A_{\mathrm{noise_i}})\mathrm{e}^{-\mathrm{i}[\omega t + (\phi_{\mathrm{i}} + \phi_{\mathrm{noise_i}})]} \tag{4.3}$$

where $A_{\mathrm{noise_i}}$ and $\phi_{\mathrm{noise_i}}$ are noise terms for power and phase from fabrication non-uniformity.

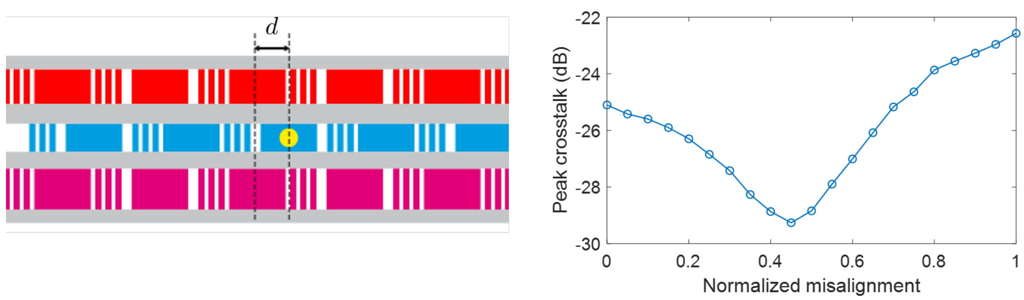

Figure 4.7. Effect of misalignment between layers. The top and bottom layer remain aligned while the middle layer is shifted laterally by an amount d (normalized to the array pitch size 775 nm)

To better illustrate the effect of the power noise, we simulated the light propagation within a vertical slice of the emitter array with 40 layers through FDTD. The electric field intensity of the cross-section across 500 μm of propagation is plotted in Fig. 4.8a. Power variation across waveguides can be observed in a periodic pattern. Fig. 4.8b shows the slice of E-field intensity at the end of 500 μm propagation and has a standard deviation of 0.12 across all waveguide powers.

The average e-field intensity during the propagation is recorded in Fig. 4.9. For each cross-section with given propagated length x, the power's standard deviation in all waveguides is calculated. And the average of such standard deviation during 500 μm propagation is 11.6%, as shown in the orange curve in Fig. 4.9a. Note that the fluctuation of the average power in Fig. 4.9a is caused by numerical errors in the large-scale simulation. Moreover,

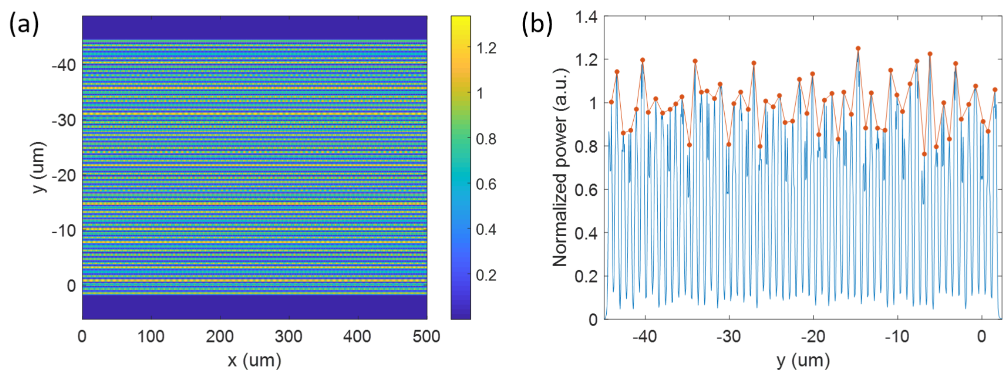

Figure 4.8. (a) E-field intensity of the waveguide array across 500 μm of propagation. (b) E-field intensity sampled at the end of 500 μm propagation.

power profile from each cross-section is used to simulate a corresponding emitted beam profile (while assuming perfectly aligned phase), overlapped and plotted in Fig. 4.9b-c. We could see that $\sim 10\%$ of power noise minorly affects the output beam quality.

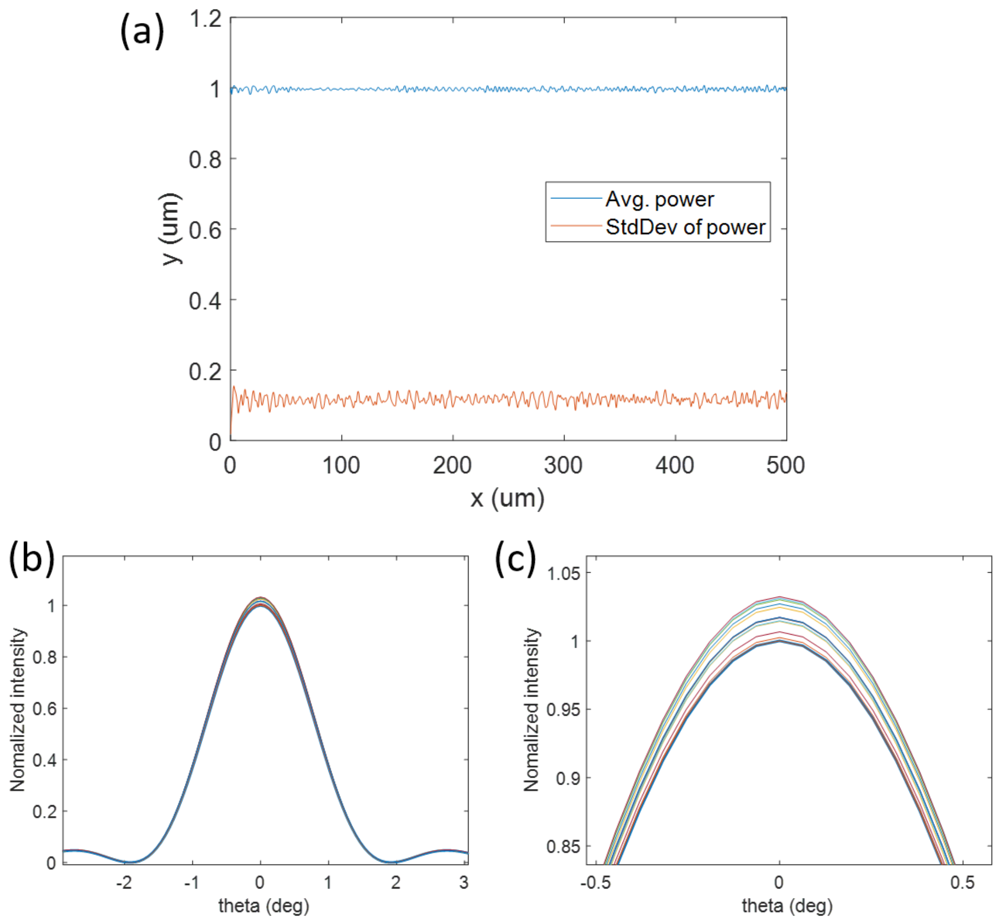

Figure 4.9. (a) Standard deviation of e-field intensity of the waveguide array across 500 μm of propagation. (b) Simulated emission from each slice of power profile in (a). (c) Zoom-in view of (b).

To evaluate the impact of any given noise level, one would traverse all possible power levels and phase within the noise level limit for every emitter in the system because, though counter-intuitive, the highest impact of noise to the system does not usually happen when all values reach their minimum or a combination of extreme values. To emulate such traversing process with efficiency, we modeled the noise terms $A_{\text{noise}_\text{i}}$ and $\phi_{\text{noise}_\text{i}}$ to follow a uniform distribution with zero mean. A random noise value is assigned to each emitter element in each simulation iteration. The worst-case scenario is recorded between different iterations, and the simulation cycle stops when the property of interest (e.g., signal-to-noise ratio (SNR) and full-width half-Maximum (FWHM)) converges.

The actual simulation models the emission from a 40×40 2D emitter array under different levels of power or phase noise. Each emitter is set as an electric dipole for simplicity. The number of iterations for each noise level was set to 10 to balance between accuracy and efficiency. The worst-case scenario among the 10 iterations was chosen for evaluation. The results are shown in Fig. 4.10, where the max noise level shows the extreme values used in the simulation (e.g, a max power noise of 0.1 means that $A_{\mathrm{noise_i}} \in [-0.1, 0.1]$). we could see that the power variation between emitters has a negligible effect on the signal-to-noise ratio (SNR), full-width half-Maximum (FWHM), and peak power of the far-field beam.

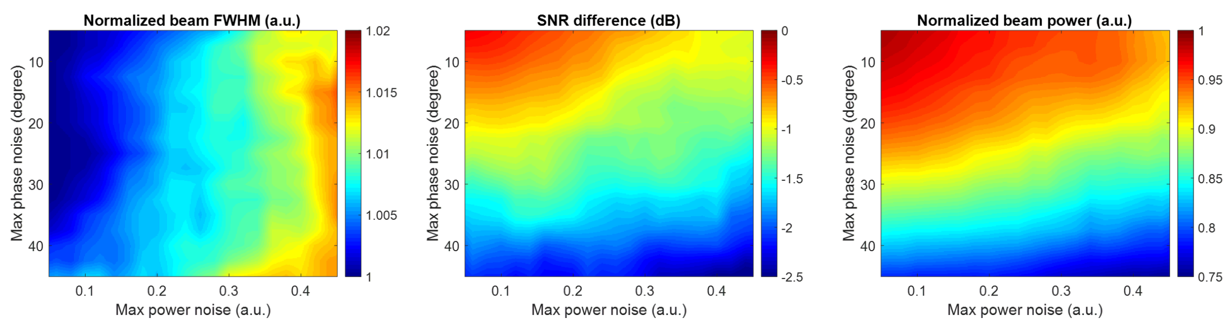

Figure 4.10. The effect of phase and power noise on (a) FWHM, (b) SNR and (c) power of the output beam.

To further investigate the power coupling in the system, 3D FDTD simulation is performed for a 2×3 basic repeat unit over 300 μm propagation length with all 6 waveguides being active. The cross-section of the simulation model is shown in Fig. 4.11a, with the same color notation used in Fig. 4.1b. To show the scalability of our design, periodic boundary conditions are applied to both y and z boundaries, as shown in Fig. 4.11a with the black dashed frame. Fig. 4.11b shows power of electric field on the array cross-section before (left) and after (right) 300 μm parallel propagation. And only barely noticeable differences could be found between the power on the two cross-sections. The optical power inside the 6 different waveguides is monitored and sampled every 0.3 μm along the 300 μm propagation simulation. The resulting power distribution at 1550 nm input wavelength is shown in the histogram in Fig. 4.11c, for both 0 phase input and alternating $0/\pi$ phase input (i.e., the extreme input phase profile where the waveguide with 0 phase are surrounded by four $\pi-$phased neighbors and vice versa). The majority ($> 85\%$) of the sampled points have their optical power within $\pm 10\%$ variation. The standard deviation in optical power is 0.089 and 0.11 respectively for 0 phase input and alternating $0/\pi$ phase input, showing that our design would work in the top left (low-noise) section of Fig. 4.10 with an aligned phase profile at the output facet. The power standard deviation is also listed in Fig. 4.11d under different operating wavelengths, showing the possibility of a low-noise operation ($\text{St.Dev}_{\text{power}} < 0.15$) over a broad bandwidth from 1400 nm to 1600 nm.

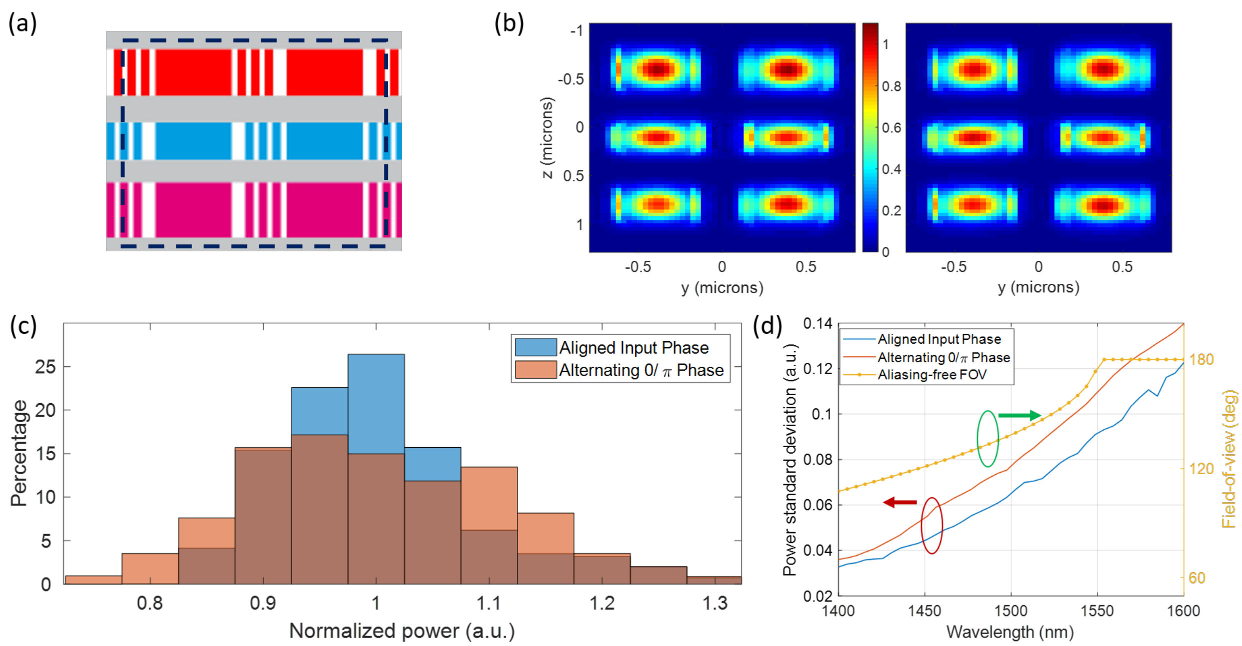

Figure 4.11. (a) Illustration of the power coupling simulation model cross-section. The black dashed frame indicates the periodic boundary used in simulation. (b) E-field intensity profile of the input facet (left) and output facet after 300 μm propagation (right), with aligned 0 phase input. (c) Statistic of power in all waveguides during propagation. (d) The standard deviation of normalized power versus different wavelength.

4.4 Summary

This chapter aims to design a multi-layer optical phased array with $\lambda/2$ emitter spacing in two dimensions. This design is based on a 2D edge emitter array and could deliver a 2D-converged beam to a full $180° \times 180^{\circ}$ aliasing-free field-of-view on a single wavelength. The power crosstalk between closely placed waveguides is suppressed by implementing phase mismatching and silicon e-skid waveguides. The crosstalk in the same layer is controlled by the asymmetric placement of the e-skid multi-layer cladding, which enhances the coupling length and introduces phase mismatch simultaneously. Waveguides in different layers cycles through 3 different silicon thicknesses to eliminate the coupling. Maximum crosstalk < -20 dB is found through 3D FDTD simulation over 300 μm propagation at 1550 nm. The design could maintain low crosstalk when different layers are horizontally misaligned. The effect of possible phase and power error in fabrication is discussed. Moreover, the design could operate in low power noise conditions over 1400 nm to 1600 nm.

5. BROADBAND SILICON PHOTONICS SWITCH BASED ON OPTICAL PHASED ARRAY

5.1 Introduction

Multiport photonics switching has gained increasing popularity for its application as a key component in data center networks [51]–[53]. Multiple platforms are used to realize these optical switches, including microelectroic mechanical systems (MEMS)[54], liquid crystal on silicon (LCOS)[55], InP-based generic integration[56], planar lightwave circuits (PLCs) [57] and silicon photonics. Among those platforms, silicon photonics switches are of particular interest for their potential in minimizing the footprint. Moreover, its complementary metal-oxide-semiconductor (CMOS) compatibility allows for mass-production resulting in low cost. Different topologies have been demonstrated to realize switches with high port-count. Conventional switch elements include Mach-Zehnder interferometer (MZI)[58], [59] and micro-ring resonator (MRR)[60]. While both elements are feasible for a large-scale switch, MZI-based designs feature a broader bandwidth at the cost of a larger footprint. And miniaturization of such switches remains a popular field of study[61].

On the contrary, MRR-based schemes achieve a smaller footprint and are limited by a narrow bandwidth. A large-scale optical switch based on silicon integrated MEMS switch elements is also demonstrated[62]. Featuring a record-high port count of 240×240, the SiPh-MEMS platform shows potentially even higher scalability, with the only drawback being a larger footprint and the high actuation voltage required for the MEMS elements. However, at the same time, the cascaded nature of conventional designs will inevitably accumulate increased crosstalk as the port count scales.

Recently, photonics switches based on optical phased array (OPA) are being demonstrated[63]–[65]. OPA-based switches exhibit a small footprint, low crosstalk for its high selectivity of beams, and a potential non-blocking operation without any waveguide crossings. The major drawback of OPA switches is that they suffer from relatively high insertion loss and high path(or port)-dependent loss (PDL). We take advantage of the half-wavelength pitched emitter array and address these problems by demonstrating a novel design for an

8×8 silicon photonic switch. The PDL in the design is suppressed by minimizing the optical path-length and angular difference between ports.

5.2 Structure design

The schematic of our design is shown in Fig. 5.1. The proposed switch consists of a center coupler region. And two series of optical phase arrays (OPAs) are placed at the input/output sides of the coupler. Each OPA consists of a 4-stage cascaded 1X2 MMI splitter tree and individual phase shifters for each waveguide. The different colored beams in the central coupler region of Fig. 5.1 indicate different working states where the input light from a particular input port is redirected to and collected by different output ports through tuning the phase shifters of the OPAs. The significant advantage of this design over Mach–Zehnder interferometer (MZI) based switches is that the beam steering and receiving process depends only on the configuration of corresponding input/output OPA ports with no waveguide crossing. At the same time, the number of control elements in our design scales linearly to the port count, which also provides much higher scalability than conventional designs with a quadratic dependence.

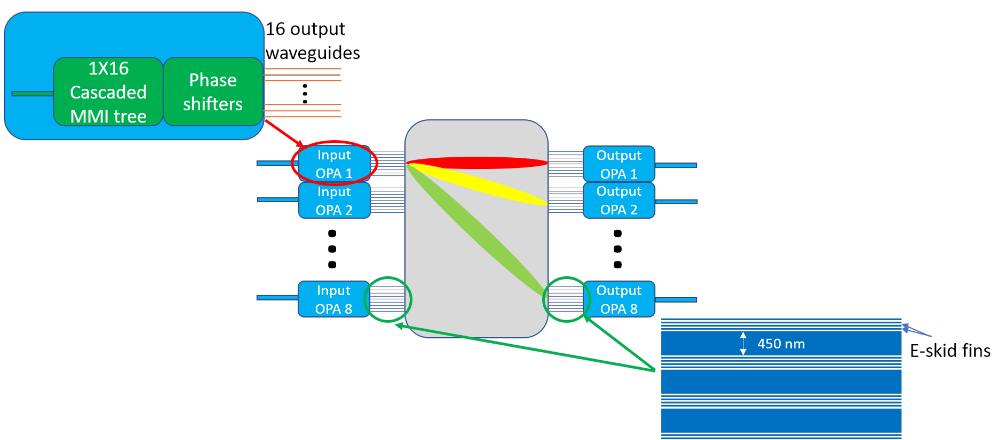

Figure 5.1. Schematic of the 8X8 optical phased array switch.

The proposed device is designed for a 220-nm-thick silicon-over-insulator (SOI) wafer with 2 μm buried oxide (BOX) layer. Metamaterial-based **e**xtreme **skin-d**epth (e-skid) waveguides are applied to 450-nm-wide silicon single-mode waveguides at the end of the

OPAs [13], [66], [67]. This allows for densely packed Si waveguide arrays to operate without crosstalk by limiting evanescent coupling between closely spaced waveguides through the use of the anisotropic metamaterial cladding. The spacing between adjacent silicon waveguides is minimized to maximize the number of ports that could fit in the field-of-view (FOV) of the OPA. All Si waveguides are placed 775 nm apart. And the spacing between adjacent OPA ports is thus 775 nm $\times 16 = 12.4\ \mu$m.

One important aspect of the design is the selection of the material for the central coupler. Unlike grating-based antenna array, the in-plane OPA switch requires extra vertical confinement from the central coupler to help direct the beam. The emission angle of all the beams emitted from an OPA with linear phase difference $\Delta\phi$ can be described as:

$$\sin\theta_m = \frac{\lambda(\Delta\phi + 2m\pi)}{2\pi n_{\text{eff}} d} \tag{5.1}$$

where θ_m is the emission angle of the m_{th} lobe, λ is the working wavelength (1550 nm), and d is the spacing between emitters. n_{eff} is the refractive index of the medium into which the OPA is emitting. And in this case, n_{eff} refers to the effective index of the planar mode inside the coupler. Fig. 5.2 shows examples where silicon and silicon nitride is used as the coupler material (SiO_2 is also included for comparison). It could be seen that using silicon will provide stronger vertical (z-axis) optical confinement for the mode with its higher index but will introduce more grating lobes and a smaller steering range at the same time. And SiN coupler behaves just the opposite way: its lower refractive index could allow for a larger steering range, but more loss is involved in the coupler due to the lack of vertical confinement. The following section will show designs using Si and SiN as the coupler material and compare their performance.

5.3 Result and Discussion

The performance of designed photonic integrated circuits (PICs) is evaluated using commercial software Lumerical Interconnect™. The S-matrix of each PIC element is extracted through 3D FDTD simulations using Lumerical FDTD Solution™, as shown in Fig. 5.3(a). The input light is first sent into a 1×16 multi-mode interferometer (MMI) splitter tree (the

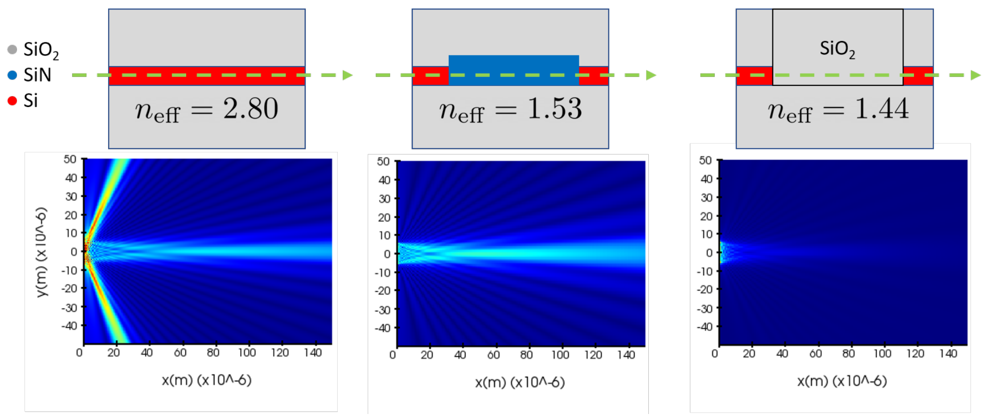

Figure 5.2. Structure (top) and cross-sectional electric field (bottom) at maximum steering angle. The material used for the central coupler region is (a) Silicon; (b) SiN; (c) SiO_2, respectively.

input OPA, which consists of cascaded 1×2 MMIs). After phase tuning, a 3D FDTD simulation is performed over the central coupler region to extract its S-matrix. The light from the output waveguides is collected by 1×16 output OPAs. Individual phase shifters in the output OPA collect/reject light from corresponding waveguides, resulting in corresponding output ports' on/off status.

Two critical problems of optical networks are path-dependent loss (PDL) and optical crosstalk, which would lead to degraded signals and extra power consumption of the system. Path-dependent loss has been widely discussed for optical multistage interconnection networks (OMINs)[68], [69]. And for our design, the PDL is evaluated by comparing the output power between port 1 and 8 with port 1 as the input port: the path $1 \rightarrow 1$ indicates the shortest optical path length, and path $1 \rightarrow 8$ indicates the longest path length and the largest steering angle. As the beam width scales inverse-proportionally with $\cos\theta$, the path $1 \rightarrow 8$ experiences the highest loss from not only longer path length but also higher beam divergence from increased steering. The device loss of these two paths for both 220 nm thick silicon platform and 350 nm thick silicon nitride platform are shown in Fig. 5.3(b) and (c). The maximum beam steering angle required to reach the furthest port is $\tan\theta_{max} = L/(M \times \text{port size})$, where L is the coupler length and M is the number of ports. Increasing device length L helps to decrease θ_{max}, which decreases steering-related loss at the cost of higher propagation loss - preferable for silicon coupler. And similarly, shorter coupler length and larger θ_{max} are preferable for the SiN coupler. The yellow arrows indicate the point when the $1 \rightarrow 8$ has the lowest loss. And the blue arrows show the points that exhibit better PDL at the cost of slightly lower efficiency. In order to gain balance between those factors, device lengths of 400 μm and 270 μm are chosen for 220 nm thick silicon and 350 nm thick silicon nitride, indicated by the blue arrows.

The transmission spectrum obtained from simulation is shown in Fig. 5.4. The figure includes configurations where input port 1 aims at output ports 1 through 8. The transmission at corresponding output ports being aimed at (and set to ON state) is represented by the colored curves; the red curves show the transmission at other output ports (set to OFF state). Detailed transmission from the ON state ports is plotted in the sub-figures on the right. We obtained a wide operating bandwidth of $1500 - 1600$ nm. And a wavelength

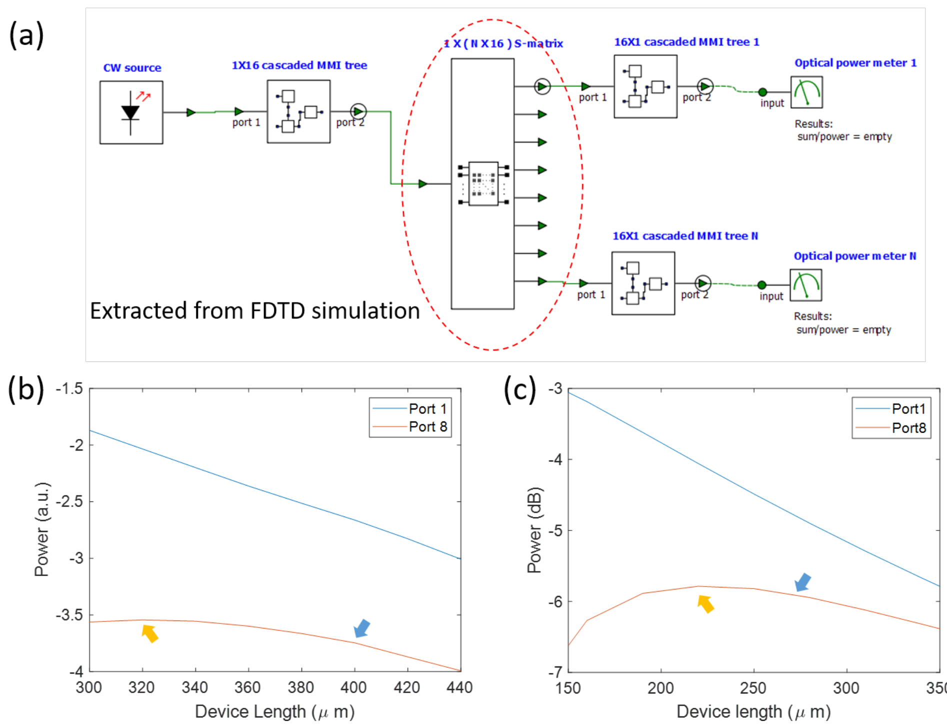

Figure 5.3. (a) Simulation scheme in Lumerical Interconnect^{TM}; (b, c) Device loss for nearest and furthest ports (port 1 and 8, respectively)with respect to device length for devices using (b) 220 nm thick silicon; and (c) 350 nm thick SiN as coupler material.

dependence of less than 1 dB is observed for ports 1 through 8. The extinction ratio of over 40 dB and insertion loss of less than 5.5 dB are achieved for both designs. More specifically, at 1550 nm, 41/45 dB signal-to-noise ratio (SNR) and 3.5/3.8 dB insertion loss are obtained for silicon and silicon nitride designs, respectively. The insets in Fig. 5.4 show the path-dependent loss of the design and is below 1 dB at 1550 nm for both platforms. Given the extra steering range provided by the silicon nitride coupler, four extra ports could be added to the design (port 9 through 12 in Fig. 5.4b), with degraded performance.

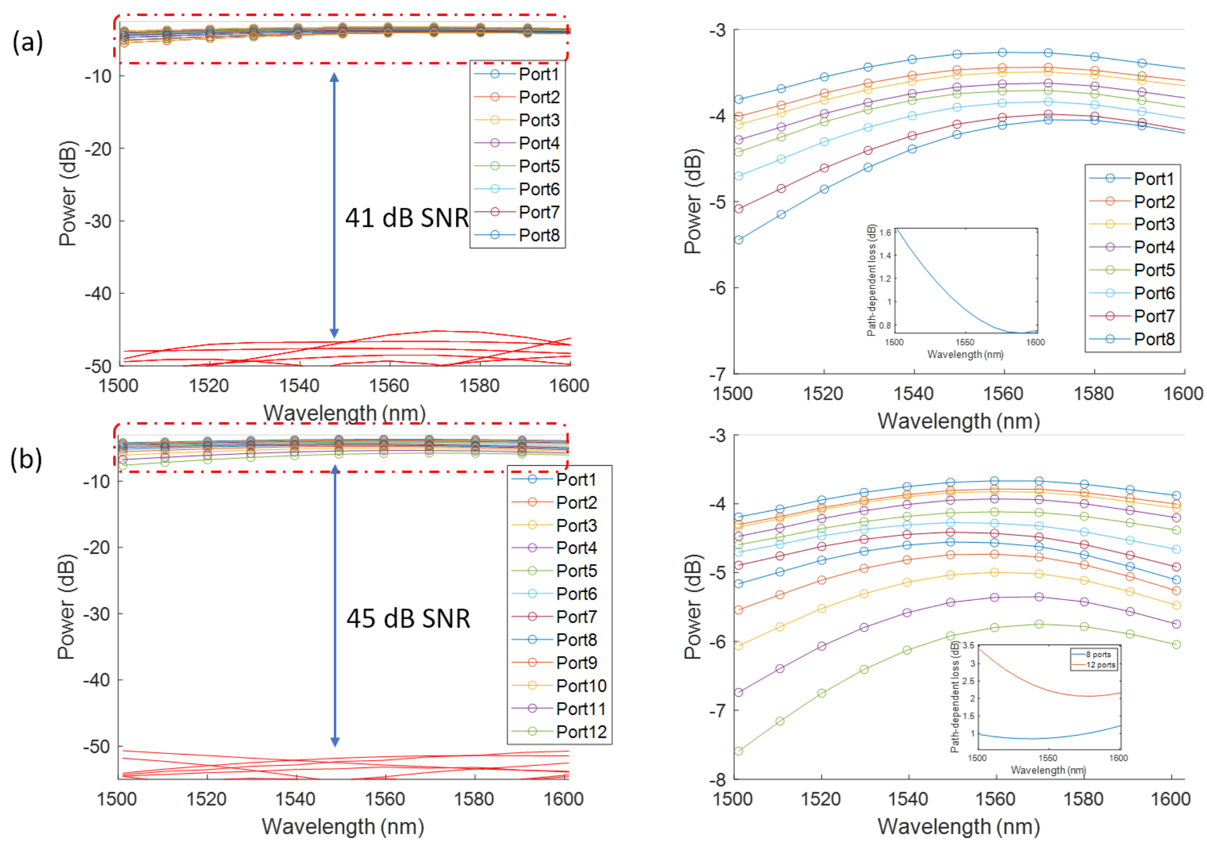

Figure 5.4. (a) Simulation result of the 220 nm silicon device, showing a 41 dB SNR and 0.73 dB minimum PDL; (b) Simulation result of the 350 nm SiN device with 45 dB SNR and 0.85 dB minimum PDL.

One serious issue that the field of silicon photonics has always faced is the random fluctuations of fabrication in mass productions, which would limit the performance of large-scale devices. Random fluctuations in structures could occur in long waveguides or among multiple copies of the same structure, introducing phase and power error into the system and affecting the overall performance [70], [71]. In Fig. 5.5, we showed the effect of fabrication errors on our design. For our system, the fluctuations mainly contribute to the uneven splitting ratio of the MMI splitter tree, which could potentially affect the beam quality inside the coupler, thus affecting the performance of the design. When all MMIs in the splitter tree are ideal, a 'flat' power profile could be expected at the OPA output plane, meaning that all output waveguides have the same power level. However, if unbalanced MMIs are considered, the output power will tend to 'concentrate' in a certain area. Fig. 5.5a shows three characteristic power profiles where unbalanced MMIs are considered in the system: The 'tilted' profile when all MMIs directs higher power to the same direction; the 'max at side' profile when all MMIs directs the majority of power to the sides and 'max at center' to the center. These represent extreme cases of output power distribution and could potentially have the largest impact on the performance. The unbalance of the MMI is quantified as the power difference between two output ports: 0 variation stands for 50%/50% output power splitting, and 0.1 variation stands for 55%/45%. To evaluate the effect of the uneven power profile, the three representative power distributions are applied to both input and output OPAs. The transmission for path $1 \rightarrow 1$ and crosstalk at port 2 (Fig. 5.5b, c); and the transmission for path $1 \rightarrow 8$ and crosstalk at port 7 (Fig. 5.5d, e) are presented at the working wavelength of 1550 nm. As shown in the figure, larger power variation does degrade the device performance, but the effect is marginal. In the worse case scenario, the transmission is lower by 0.25 dB (path $1 \rightarrow 8$, 'Max at sides' profile) and the noise level is higher by 1.8 dB (path $1 \rightarrow 1$, 'Max at center'). The beam formation from an OPA could be seen as an example of N-slit diffraction, which is less susceptible to power variation in individual sources but relies more on the phase relationship. It is worth noting that in some cases (e.g., path $1 \rightarrow 1$, 'Max at sides'), the crosstalk at the adjacent OFF state port is even lower than a uniform power profile. In such cases, the background power is distributed more evenly across multiple output ports, resulting in lower peak transmission and lower peak crosstalk at the same time. And in our design, we assume that individual phase shifters are used to align the phase of each channel at the output facet. While phase error greatly impacts beam quality, it could be compensated by fine-tuning individual phase shifters. Effective algorithms for controlling a large number of phase shifters have been widely reported and implemented [72], [73], which would ensure the robustness of the design.

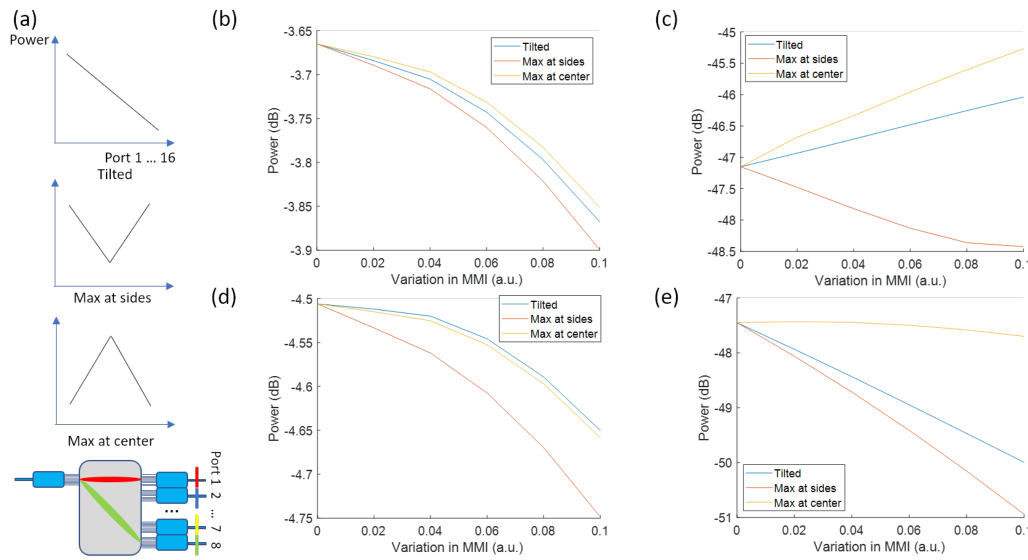

Figure 5.5. (a) Illustration of the 3 representative power distributions at the end of the splitter tree for unbalanced MMIs; (b, c) Performance of the 270um SiN device when aiming at port 1 (b, red line, ON state) and the crosstalk at port 2 (c, blue line, OFF state); (d, e) when aiming at port 8 (d, yellow line, ON state) and the crosstalk at port 7 (e, green line, OFF state) with respect to different MMI power variation.

If we utilize the 2D edge emitter array proposed in Fig. 4.1b to take the place of 1D OPA emitters, a 64×64 OPA-based 3D switch could be realized while keeping the same maximum device width as an 8×8 2D in-plane switch. The general concept is illustrated in Fig. 5.6a. As the 2D emitter array provides beam confinement in both dimensions, the coupler material could be chosen to be air ($n = 1$). The switch will work in a grating lobe-free condition while best utilizing the half-wavelength pitched emitter array. While the number of grating lobes and propagation loss is no longer present in the 3D switch design, the design goal is further simplified into gaining balance between emitter size (beam confinement at the cost of device width) and coupler length (smaller maximum steering angle at the cost of more beam divergence). A corner emitter and the diagonal receivers (labeled from 1 to 8 with increasing distance from the corner emitter) are chosen to represent the performance of the design best. The FDTD simulation result from several different parameter combinations is shown in Fig. 5.6b. The structure includes transceiver and receiver planes, which consists of 8×8 emitter and receiver elements. Each element is a 2D waveguide edge emitter array, as illustrated in the inset of Fig. 5.6a. As expected from the results of the in-plane switches, the use of smaller emitter element size or longer device length could result in less PDL, but at the cost of higher overall loss.

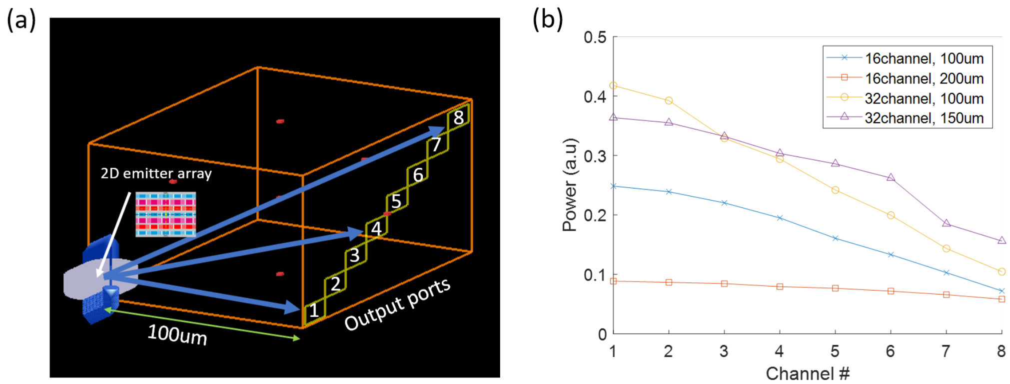

Figure 5.6. (a) Schematic of the proposed 3D OPA switch; (b) Simulation result of the 3D switch with various channel size and device length.

Those 3D FDTD simulations are very computation-intensive due to their large scale. As the switch operates in a grating lobe-free condition, the emission and receiving process can be emulated by the propagation of coupling of Gaussian beam in free space. We simplify the emission from an emitter block to a Gaussian beam with waist w_0 equals half of the emitter size. As the beam then travels in free-space, its intensity follows[74]:

$$I(r,z) = \frac{P}{\pi w(z)^2/2} \exp(-2\frac{r^2}{w(z)^2}) \tag{5.2}$$

where P is the total power of the beam. $w(z)$ is the beam width at distance z, given by:

$$w(z) = w_0\sqrt{1+(\frac{\lambda z}{\pi w_0^2})^2} \tag{5.3}$$

At the receiver side, the amount of power captured by the aperture r_0 is

$$P(r_0) = \int_0^{r_0} \frac{2P}{\pi w^2/2} \exp(\frac{-2r_0^2}{w^2})dr \tag{5.4}$$

So the ratio between captured power and total emitted power is

$$P(r_0)/P(\infty) = 1 - \exp(\frac{-2r_0^2}{w^2}) \tag{5.5}$$

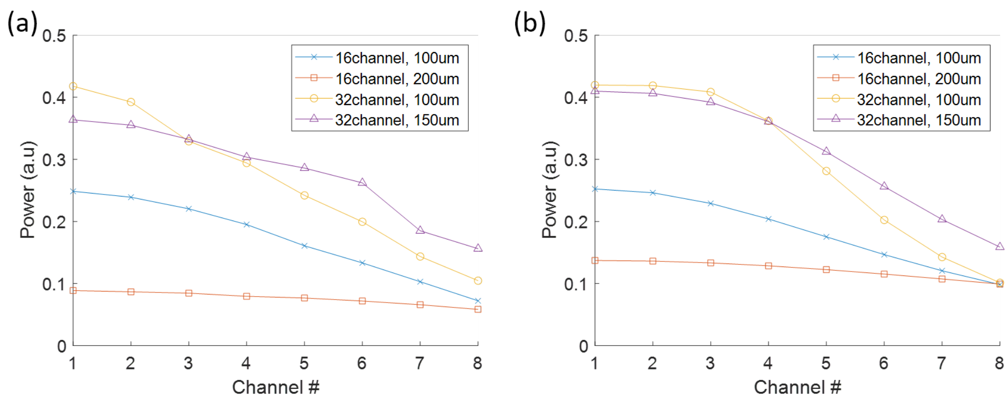

Figure 5.7. (a) FDTD result of the 3D switch, reproduced from Fig. 5.6b; (b) Estimation from Gaussian beam propagation

The comparison between FDTD simulation and numerical estimation from Gaussian beam is presented in Fig. 5.7, showing good agreement in overall trend and relationships. This allows us to estimate the performance for more complicated design schemes. For example, as shown in Fig. 5.8a, the outer ring of emitters are increased to $2NN$ from $N \times N$in size to compensate for the large beam broadening loss from the longest diagonal path $1 \rightarrow 8$. Similarly, the emitter size of the second outer ring is increased to $1.5N \times 1.5N$. The result is shown in Fig. 5.8b. We can see that the increase in individual port size well compensates for the performance from diagonal paths. Moreover, further improvement in port response uniformity is expected with a more accurate apodization of the system.

5.4 Summary

This chapter presents the architecture of an SOI-based 8×8 switch using optical phased array. E-skid waveguides are used in the design to control the evanescent coupling between closely packed ports. As a result, more operating ports could fit into a small FOV of the OPA. And low-loss switching is achieved from the use of a half-wavelength pitch emitter array.

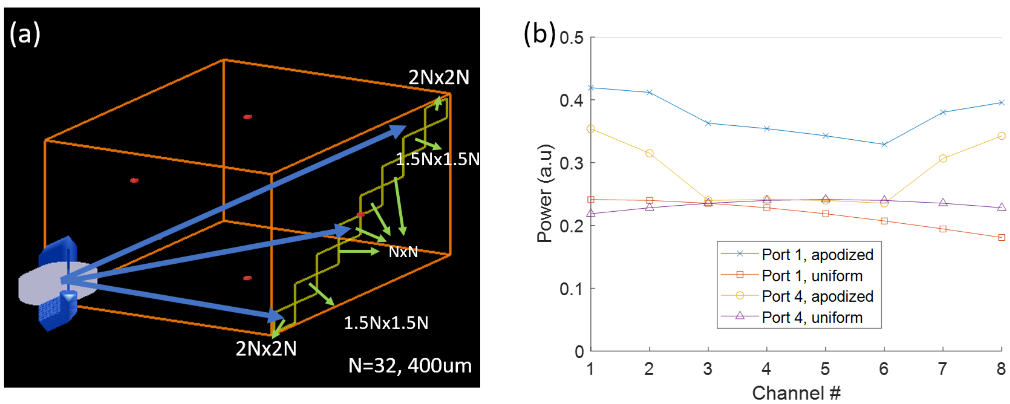

Figure 5.8. (a) Scheme of the emitter size apodization; (b) Calculated switch efficiency.

Broadband (1500 - 1600 nm) switching is numerically demonstrated for silicon and silicon nitride couplers with 3.5/3.8 dB insertion loss and less than 1 dB PDL at 1550 nm. Moreover, we discuss the effect of potential non-uniform power splitting of the cascaded MMI tree from fabrication fluctuation and have shown its minor effect on the device performance. Finally, using a 2D end-fire emitter element is promising for enhancing the number of operational ports. The proposed design demonstrates a scalable and low-loss optical switch in a compact footprint, which can be found necessary in multiple applications.

6. SUMMARY AND FUTURE WORK

In summary, in this thesis, we have shown the design, fabrication, and characterization of a uniform half-wavelength spaced grating emitter array. Moreover, we extended the design scheme to two-dimensional end-fire OPA and optical switches.

In Chapter 2, the design and fabrication process of the OPA components were shown, including the design of multimode interferometer (MMI), SiN/Si power coupler, TO/EO phase shifters, and grating emitter array. The application of e-skid waveguides realizes the half-wavelength pitch between emitters. The fabrication of a dense e-skid waveguide array is done through proximity effect correction by Yun Jo Lee.

In Chapter 3, a 32-channel aliasing-free optical phased array with half-wavelength emitter pitch and high emission power was demonstrated. SiN input couplers were used for high power coupling onto the device. Si e-skid emitter array was used to achieve half-wavelength emitter pitch. De-convolution of the retrieved power profile was performed to recover the original emission pattern and the power within the main beam. The amount of phase noise in the system is evaluated. And a record-high FOV of 135°is measured along with high emission power (44 mW), which makes the design promising for long-range LiDAR systems.

In Chapter 4, we extended the use of the e-skid waveguide array to end-fire emitter arrays. A multi-layer optical phased array with $\lambda/2$ emitter spacing in two dimensions was proposed. The combination of the e-skid waveguide and propagation constant mismatch limits the power crosstalk in both dimensions, and thus 2D-converged beam steering with full $180° \times 180^{\circ}$ aliasing-free field-of-view on a single wavelength is numerically demonstrated. The crosstalk in the same layer is controlled by the asymmetric placement of the e-skid multi-layer cladding, which enhances the coupling length and introduces phase mismatch simultaneously. Crosstalk between vertically aligned waveguides is suppressed by cycling through 3 different silicon thicknesses. Maximum crosstalk < -20 dB is verified by using 3D FDTD simulation over 300 μm propagation at 1550 nm. The design is prone to horizontal misalignment between layers. And the effect of possible phase and power error in fabrication is discussed and could be minimized with a proper phase control mechanism.

In Chapter 5, the half-wavelength edge emitter array was applied to an SOI-based 8×8 switch. The use of e-skid waveguides lowered the power loss from extra grating lobes in the switch. And as a result, more operating ports could be fit into a small FOV of the OPA. Comparable designs for switching are numerically demonstrated for silicon and silicon nitride couplers with 3.5/3.8 dB insertion loss and less than 1 dB PDL at 1550 nm. The effect of power noise from fabrication fluctuation is also evaluated. Finally, using a 2D emitter element further enhances the optical switch to a potential 64×64 setup.

This thesis's future work should mainly focus on scaling the OPA design demonstrated in Chapter 3 and realizing designs from Chapters 4 and 5. The performance of the half-wavelength pitched OPA shown in chapter 3 is mainly limited by the lack of an active phase control mechanism and the limit in the number of channels. Scaling the OPA with more channels can provide more power capacity as well as finer beam confinement. Furthermore, integrating active phase shifters on the chip would considerably lower the phase noise of the emission, which will also allow for high-speed beam steering. The feasibility of the multi-layer 2D end-fire emitter array should also be analyzed.

REFERENCES

[1] J. K. Doylend, M. Heck, J. T. Bovington, J. D. Peters, L. Coldren, and J. Bowers, "Two-dimensional free-space beam steering with an optical phased array on silicon-on-insulator," *Optics express*, vol. 19, no. 22, pp. 21 595–21 604, 2011.

[2] C. T. Phare, M. C. Shin, S. A. Miller, B. Stern, and M. Lipson, "Silicon optical phased array with high-efficiency beam formation over 180 degree field of view," *arXiv preprint arXiv:1802.04624*, 2018.

[3] C. V. Poulton, M. J. Byrd, E. Timurdogan, P. Russo, D. Vermeulen, and M. R. Watts, "Optical phased arrays for integrated beam steering," in *2018 IEEE 15th International Conference on Group IV Photonics (GFP)*, IEEE, 2018, pp. 1–2.

[4] C. V. Poulton, M. J. Byrd, P. Russo, E. Timurdogan, M. Khandaker, D. Vermeulen, and M. R. Watts, "Long-range lidar and free-space data communication with high-performance optical phased arrays," *IEEE Journal of Selected Topics in Quantum Electronics*, vol. 25, no. 5, pp. 1–8, 2019.

[5] C. V. Poulton, P. Russo, B. Moss, M. Khandaker, M. J. Byrd, J. Tran, E. Timurdogan, D. Vermeulen, and M. R. Watts, "Small-form-factor optical phased array module for technology adoption in custom applications," in *CLEO: Applications and Technology*, Optical Society of America, 2019, JTh5B–6.

[6] J. Hulme, J. Doylend, M. Heck, J. Peters, M. Davenport, J. Bovington, L. Coldren, and J. Bowers, "Fully integrated hybrid silicon two dimensional beam scanner," *Optics express*, vol. 23, no. 5, pp. 5861–5874, 2015.

[7] H. J. Visser, *Array and phased array antenna basics*. John Wiley & Sons, 2006.

[8] A. Yaacobi, "Integrated optical phased arrays for lidar applications," Ph.D. dissertation, Massachusetts Institute of Technology, 2015.

[9] S. Chung, H. Abediasl, and H. Hashemi, "A monolithically integrated large-scale optical phased array in silicon-on-insulator cmos," *IEEE Journal of Solid-State Circuits*, vol. 53, no. 1, pp. 275–296, 2017.

[10] T. Komljenovic, R. Helkey, L. Coldren, and J. E. Bowers, "Sparse aperiodic arrays for optical beam forming and lidar," *Optics express*, vol. 25, no. 3, pp. 2511–2528, 2017.

[11] D. N. Hutchison, J. Sun, J. K. Doylend, R. Kumar, J. Heck, W. Kim, C. T. Phare, A. Feshali, and H. Rong, "High-resolution aliasing-free optical beam steering," *Optica*, vol. 3, no. 8, pp. 887–890, 2016.

[12] B. E. Saleh and M. C. Teich, *Fundamentals of photonics*. John Wiley & Sons, 2019.

[13] S. Jahani, S. Kim, J. Atkinson, J. C. Wirth, F. Kalhor, A. Al Noman, W. D. Newman, P. Shekhar, K. Han, V. Van, *et al.*, "Controlling evanescent waves using silicon photonic all-dielectric metamaterials for dense integration," *Nature communications*, vol. 9, no. 1, pp. 1–9, 2018.

[14] C. V. Poulton, A. Yaacobi, D. B. Cole, M. J. Byrd, M. Raval, D. Vermeulen, and M. R. Watts, "Coherent solid-state lidar with silicon photonic optical phased arrays," *Optics letters*, vol. 42, no. 20, pp. 4091–4094, 2017.

[15] M. Gehl, G. Hoffman, P. Davids, A. Starbuck, C. Dallo, Z. Barber, E. Kadlec, R. K. Mohan, S. Crouch, and C. Long, "Phase optimization of a silicon photonic two-dimensional electro-optic phased array," in *CLEO: Science and Innovations*, Optical Society of America, 2019, JTh2A–39.

[16] W. Xu, H. Tang, L. Zhou, L. Lu, and J. Chen, "Aliasing-free beam-steering over the entire field of view utilizing a bent waveguide array with a uniform half-wavelength spacing," in *2018 European Conference on Optical Communication (ECOC)*, IEEE, 2018, pp. 1–3.

[17] C. V. Poulton, M. J. Byrd, M. Raval, Z. Su, N. Li, E. Timurdogan, D. Coolbaugh, D. Vermeulen, and M. R. Watts, "Large-scale silicon nitride nanophotonic phased arrays at infrared and visible wavelengths," *Optics letters*, vol. 42, no. 1, pp. 21–24, 2017.

[18] J. Notaros, M. Notaros, M. Raval, and M. R. Watts, "Liquid-crystal-based visible-light integrated optical phased arrays," in *CLEO: Science and Innovations*, Optical Society of America, 2019, STu3O–3.

[19] C. Weitkamp, *Lidar: range-resolved optical remote sensing of the atmosphere*. Springer Science & Business, 2006, vol. 102.

[20] C. V. Poulton, P. Russo, E. Timurdogan, M. Whitson, M. J. Byrd, E. Hosseini, B. Moss, Z. Su, D. Vermeulen, and M. R. Watts, "High-performance integrated optical phased arrays for chip-scale beam steering and lidar," in *CLEO: Applications and Technology*, Optical Society of America, 2018, ATu3R–2.

[21] C. Wang, M. Zhang, B. Stern, M. Lipson, and M. Lončar, "Nanophotonic lithium niobate electro-optic modulators," *Optics express*, vol. 26, no. 2, pp. 1547–1555, 2018.

[22] W. S. Levine, *The Control Handbook (three volume set)*. CRC press, 2018.

[23] R. Waldhäusl, B. Schnabel, P. Dannberg, E.-B. Kley, A. Bräuer, and W. Karthe, "Efficient coupling into polymer waveguides by gratings," *Applied optics*, vol. 36, no. 36, pp. 9383–9390, 1997.

[24] K. Shang, C. Qin, Y. Zhang, G. Liu, X. Xiao, S. Feng, and S. Yoo, “Uniform emission, constant wavevector silicon grating surface emitter for beam steering with ultra-sharp instantaneous field-of-view,” *Optics express*, vol. 25, no. 17, pp. 19 655–19 661, 2017.

[25] D. Vermeulen, S. Selvaraja, P. Verheyen, G. Lepage, W. Bogaerts, P. Absil, D. Van Thourhout, and G. Roelkens, “High-efficiency fiber-to-chip grating couplers realized using an advanced cmos-compatible silicon-on-insulator platform,” *Optics express*, vol. 18, no. 17, pp. 18 278–18 283, 2010.

[26] W. D. Sacher, Y. Huang, L. Ding, B. J. Taylor, H. Jayatilleka, G.-Q. Lo, and J. K. Poon, “Wide bandwidth and high coupling efficiency si 3 n 4-on-soi dual-level grating coupler,” *Optics express*, vol. 22, no. 9, pp. 10 938–10 947, 2014.

[27] J. Notaros, F. Pavanello, M. T. Wade, C. M. Gentry, A. Atabaki, L. Alloatti, R. J. Ram, and M. A. Popović, “Ultra-efficient cmos fiber-to-chip grating couplers,” in *2016 Optical Fiber Communications Conference and Exhibition (OFC)*, IEEE, 2016, pp. 1–3.

[28] M. Fan, M. A. Popović, and F. X. Kärtner, “High directivity vertical fiber-to-chip coupler with anisotropically radiating grating teeth,” in *Conference on Lasers and Electro-Optics*, Optical Society of America, 2007, CTuDD3.

[29] M. Raval, C. V. Poulton, and M. R. Watts, “Unidirectional waveguide grating antennas for nanophotonic phased arrays,” in *CLEO: Science and Innovations*, Optical Society of America, 2017, STh1M–5.

[30] M. Raval, C. V. Poulton, and M. R. Watts, “Unidirectional waveguide grating antennas with uniform emission for optical phased arrays,” *Optics letters*, vol. 42, no. 13, pp. 2563–2566, 2017.

[31] H. Yun, W. Shi, Y. Wang, L. Chrostowski, and N. A. Jaeger, “2x2 adiabatic 3-db coupler on silicon-on-insulator rib waveguides,” in *Photonics North 2013*, International Society for Optics and Photonics, vol. 8915, 2013, p. 89150V.

[32] W.-P. Huang, “Coupled-mode theory for optical waveguides: An overview,” *JOSA A*, vol. 11, no. 3, pp. 963–983, 1994.

[33] K. J. Seu, A. P. Pandey, F. Haque, E. A. Proctor, A. E. Ribbe, and J. S. Hovis, “Effect of surface treatment on diffusion and domain formation in supported lipid bilayers,” *Biophysical journal*, vol. 92, no. 7, pp. 2445–2450, 2007.

[34] M. Altissimo, “E-beam lithography for micro-/nanofabrication,” *Biomicrofluidics*, vol. 4, no. 2, p. 026 503, 2010.

[35] S. Sabouri and K. Jamshidi, "Design considerations of silicon nitride optical phased array for visible light communications," *IEEE Journal of Selected Topics in Quantum Electronics*, vol. 24, no. 6, pp. 1–7, 2018.

[36] P. Wang, G. Luo, Y. Xu, Y. Li, Y. Su, J. Ma, R. Wang, Z. Yang, X. Zhou, Y. Zhang, *et al.*, "Design and fabrication of a sin-si dual-layer optical phased array chip," *Photonics Research*, vol. 8, no. 6, pp. 912–919, 2020.

[37] Q. Wang, S. Wang, L. Jia, Y. Cai, W. Yue, and M. Yu, "Silicon nitride assisted 1× 64 optical phased array based on a soi platform," *Optics Express*, vol. 29, no. 7, pp. 10 509–10 517, 2021.

[38] L. Zhang, Y. Li, Y. Hou, Y. Wang, M. Tao, B. Chen, Q. Na, Y. Li, Z. Zhi, X. Liu, *et al.*, "Investigation and demonstration of a high-power handling and large-range steering optical phased array chip," *Optics Express*, vol. 29, no. 19, pp. 29 755–29 765, 2021.

[39] K. Van Acoleyen, W. Bogaerts, and R. Baets, "Two-dimensional dispersive off-chip beam scanner fabricated on silicon-on-insulator," *IEEE photonics technology letters*, vol. 23, no. 17, pp. 1270–1272, 2011.

[40] J. Kennedy and R. Eberhart, "Particle swarm optimization," in *Proceedings of ICNN'95-international conference on neural networks*, IEEE, vol. 4, pp. 1942–1948.

[41] D. N. Hutchison, J. Sun, J. K. Doylend, R. Kumar, J. Heck, W. Kim, C. T. Phare, A. Feshali, and H. Rong, "High-resolution aliasing-free optical beam steering," *Optica*, vol. 3, no. 8, pp. 887–890, 2016.

[42] Y. Zhang, Y.-C. Ling, K. Zhang, C. Gentry, D. Sadighi, G. Whaley, J. Colosimo, P. Suni, and S. B. Yoo, "Sub-wavelength-pitch silicon-photonic optical phased array for large field-of-regard coherent optical beam steering," *Optics express*, vol. 27, no. 3, pp. 1929–1940, 2019.

[43] W. Xu, L. Zhou, L. Lu, and J. Chen, "Aliasing-free optical phased array beam-steering with a plateau envelope," *Optics express*, vol. 27, no. 3, pp. 3354–3368, 2019.

[44] Z. Kong, Y. J. Lee, A. Al Noman, Y. Tang, G. Chang, R. Chen, and M. Qi, "Aliasing-free beam steering from an optical array emitter with half-wavelength pitch," in *Integrated Photonics Research, Silicon and Nanophotonics*, Optical Society of America, 2020, ITh2H–6.

[45] H. Zhang, C. Li, X. Tu, J. Song, H. Zhou, X. Luo, Y. Huang, M. Yu, and G. Lo, "Efficient silicon nitride grating coupler with distributed bragg reflectors," *Optics express*, vol. 22, no. 18, pp. 21 800–21 805, 2014.

[46] J. Zou, Y. Yu, M. Ye, L. Liu, S. Deng, and X. Zhang, "Ultra efficient silicon nitride grating coupler with bottom grating reflector," *Optics express*, vol. 23, no. 20, pp. 26 305–26 312, 2015.

[47] M. R. Kossey, C. Rizk, and A. C. Foster, "End-fire silicon optical phased array with half-wavelength spacing," *APL Photonics*, vol. 3, no. 1, p. 011 301, 2018.

[48] A. Hosseini, D. Kwong, Y. Zhang, S. A. Chandorkar, F. Crnogorac, A. Carlson, B. Fallah, S. Bank, E. Tutuc, J. Rogers, *et al.*, "On the fabrication of three-dimensional silicon-on-insulator based optical phased array for agile and large angle laser beam steering systems," *Journal of Vacuum Science & Technology B, Nanotechnology and Microelectronics: Materials, Processing, Measurement, and Phenomena*, vol. 28, no. 6, C6O1–C6O7, 2010.

[49] B. Guan, C. Qin, R. P. Scott, B. Ercan, N. K. Fontaine, T. Su, and S. Yoo, "Hybrid 3d photonic integrated circuit for optical phased array beam steering," in *CLEO: Science and Innovations*, Optical Society of America, 2015, STu2F–1.

[50] W. Song, R. Gatdula, S. Abbaslou, M. Lu, A. Stein, W. Y. Lai, J. Provine, R. F. W. Pease, D. N. Christodoulides, and W. Jiang, "High-density waveguide superlattices with low crosstalk," *Nature communications*, vol. 6, p. 7027, 2015.

[51] Q. Cheng, M. Bahadori, M. Glick, S. Rumley, and K. Bergman, "Recent advances in optical technologies for data centers: A review," *Optica*, vol. 5, no. 11, pp. 1354–1370, 2018.

[52] Q. Cheng, S. Rumley, M. Bahadori, and K. Bergman, "Photonic switching in high performance datacenters," *Optics express*, vol. 26, no. 12, pp. 16 022–16 043, 2018.

[53] B. G. Lee, N. Dupuis, P. Pepeljugoski, L. Schares, R. Budd, J. R. Bickford, and C. L. Schow, "Silicon photonic switch fabrics in computer communications systems," *Journal of Lightwave Technology*, vol. 33, no. 4, pp. 768–777, 2014.

[54] L. Fan, S. Gloeckner, P. Dobblelaere, S. Patra, D. Reiley, C. King, T. Yeh, J. Gritters, S. Gutierrez, Y. Loke, *et al.*, "Digital mems switch for planar photonic crossconnects," in *Optical Fiber Communication Conference*, Optical Society of America, 2002, TuO4.

[55] B. Robertson, H. Yang, M. M. Redmond, N. Collings, J. R. Moore, J. Liu, A. M. Jeziorska-Chapman, M. Pivnenko, S. Lee, A. Wonfor, *et al.*, "Demonstration of multi-casting in a 1× 9 lcos wavelength selective switch," *Journal of lightwave technology*, vol. 32, no. 3, pp. 402–410, 2013.

[56] R. Stabile, A. Rohit, and K. Williams, "Monolithically integrated 8× 8 space and wavelength selective cross-connect," *Journal of Lightwave Technology*, vol. 32, no. 2, pp. 201–207, 2013.

[57] S. Sohma, T. Watanabe, N. Ooba, M. Itoh, T. Shibata, and H. Takahashi, "Silica-based plc type 32 x 32 optical matrix switch," in *2006 European Conference on Optical Communications*, IEEE, 2006, pp. 1–2.

[58] K. Tanizawa, K. Suzuki, M. Toyama, M. Ohtsuka, N. Yokoyama, K. Matsumaro, M. Seki, K. Koshino, T. Sugaya, S. Suda, *et al.*, "Ultra-compact 32× 32 strictly-non-blocking si-wire optical switch with fan-out lga interposer," *Optics express*, vol. 23, no. 13, pp. 17 599–17 606, 2015.

[59] L. Qiao, W. Tang, and T. Chu, "32× 32 silicon electro-optic switch with built-in monitors and balanced-status units," *Scientific Reports*, vol. 7, no. 1, pp. 1–7, 2017.

[60] D. Nikolova, D. M. Calhoun, Y. Liu, S. Rumley, A. Novack, T. Baehr-Jones, M. Hochberg, and K. Bergman, "Modular architecture for fully non-blocking silicon photonic switch fabric," *Microsystems & nanoengineering*, vol. 3, no. 1, pp. 1–9, 2017.

[61] R. Konoike, K. Suzuki, S. Namiki, H. Kawashima, and K. Ikeda, "Ultra-compact silicon photonics switch with high-density thermo-optic heaters," *Optics express*, vol. 27, no. 7, pp. 10 332–10 342, 2019.

[62] T. J. Seok, K. Kwon, J. Henriksson, J. Luo, and M. C. Wu, "Wafer-scale silicon photonic switches beyond die size limit," *Optica*, vol. 6, no. 4, pp. 490–494, 2019.

[63] S. Katayose, Y. Hashizume, and M. Itoh, "1× 8 silicon-silica hybrid thermo-optic switch with multi-chip configuration based on optical phased array," in *2015 20th Microoptics Conference (MOC)*, IEEE, 2015, pp. 1–2.

[64] T. Tanemura, L. Langouche, and Y. Nakano, "Strictly non-blocking 8× 8 silicon photonic switch based on optical phased array," in *2015 European Conference on Optical Communication (ECOC)*, IEEE, 2015, pp. 1–3.

[65] Z. Li, Y. Yu, and X. Zhang, "Scalable 1× n switch using optical phased array," in *Asia Communications and Photonics Conference*, Optical Society of America, 2020, M4A–170.

[66] Z. Kong, Y. J. Lee, A. Al Noman, Y. Tang, G. Chang, R. Chen, and M. Qi, "Aliasing-free beam steering from an optical array emitter with half-wavelength pitch," in *Integrated Photonics Research, Silicon and Nanophotonics*, Optical Society of America, 2020, ITh2H–6.

[67] M. B. Mia, S. Z. Ahmed, I. Ahmed, Y. J. Lee, M. Qi, and S. Kim, "Exceptional coupling in photonic anisotropic metamaterials for extremely low waveguide crosstalk," *Optica*, vol. 7, no. 8, pp. 881–887, 2020.

[68] Y. Pan, C. Qiao, and Y. Yang, “Optical multistage interconnection networks: New challenges and approaches,” *IEEE Communications Magazine*, vol. 37, no. 2, pp. 50–56, 1999.

[69] R. Bashirov and T. Karanfiller, “On path dependent loss and switch crosstalk reduction in optical networks,” *Information Sciences*, vol. 180, no. 6, pp. 1040–1050, 2010.

[70] L. Chrostowski, X. Wang, J. Flueckiger, Y. Wu, Y. Wang, and S. T. Fard, “Impact of fabrication non-uniformity on chip-scale silicon photonic integrated circuits,” in *Optical Fiber Communication Conference*, Optical Society of America, 2014, Th2A–37.

[71] Y. Yang, Y. Ma, H. Guan, Y. Liu, S. Danziger, S. Ocheltree, K. Bergman, T. Baehr-Jones, and M. Hochberg, “Phase coherence length in silicon photonic platform,” *Optics express*, vol. 23, no. 13, pp. 16 890–16 902, 2015.

[72] T. Komljenovic, R. Helkey, L. Coldren, and J. E. Bowers, “Sparse aperiodic arrays for optical beam forming and lidar,” *Optics express*, vol. 25, no. 3, pp. 2511–2528, 2017.

[73] T. Komljenovic and P. Pintus, “On-chip calibration and control of optical phased arrays,” *Optics express*, vol. 26, no. 3, pp. 3199–3210, 2018.

[74] H. Kogelnik and T. Li, “Laser beams and resonators,” *Applied optics*, vol. 5, no. 10, pp. 1550–1567, 1966.